

NATIONAL & INTERNATIONAL SCIENTIFIC EVENTS

10th Asian-Pacific Conference on Biomechanics
(AP Biomech 2019)

Venue: Chang Yung-Fa Foundation International
Convention Center
Location: Taipei City, Taiwan

Begins: November 1, 2019
Ends: November 3, 2019

The 22nd International Avar Cybersecurity Confer-
ence

Venue: Hotel New Otani Osaka
Location: Osaka, Japan

Begins: November 6, 2019
Ends: November 9, 2019

The 20th Asia Pacific Industrial Engineering And
Management Systems (APIEMS 2019)

Venue: Hotel Kanazawa
Location: Kanazawa City, Japan

Begins: December 2, 2019
Ends: December 5, 2019

The 20th International Symposium on Advanced
Intelligent Systems

Venue: ICC JEJU
Location: Jeju Island, Korea

Begins: December 4, 2019
Ends: December 7, 2019

11th International Conference on Environmental
Science and Development

Venue: K+K Hotel
Location: Barcelona, Spain

Begins: February 10, 2020
Ends: February 12, 2020

13th International Joint Conference on Biomedical
Engineering Systems and Technologies

Venue: Grand Hotel Excelsior
Location: Valletta, Malta

Begins: February 24, 2020
Ends: February 26, 2020

17th World Conference on Continuing Engineering
Education (IACEE 2020)

Venue: NTNU Campus
Location: Trondheim, Norway

Begins: May 26, 2020
Ends: May 29, 2020

14th Mediterranean Congress of Chemical Engi-
neering

Venue: Gran Via Venue
Location: Barcelona, Spain

Begins: June 2, 2020
Ends: June 5, 2020

34th European Composite Materials Congress

Venue: Viking Line Terminal
Location: Stockholm, Sweden

Begins: June 9, 2020
Ends: June 11, 2020

The 49th International Congress and Exposition
on Noise Control Engineering

Venue: Convention and Exhibition Center
Location: Seoul, Korea

Begins: August 23, 2020
Ends: August 26, 2020

23rd International Conference on Electrical Ma-
chines and Systems (ICEMS2020)

Venue: ACT CITY Hamamatsu
Location: Hamamatsu, Japan

Begins: November 24, 2020
Ends: November 27, 2020

14th International Conference on Hydrosience
and Engineering

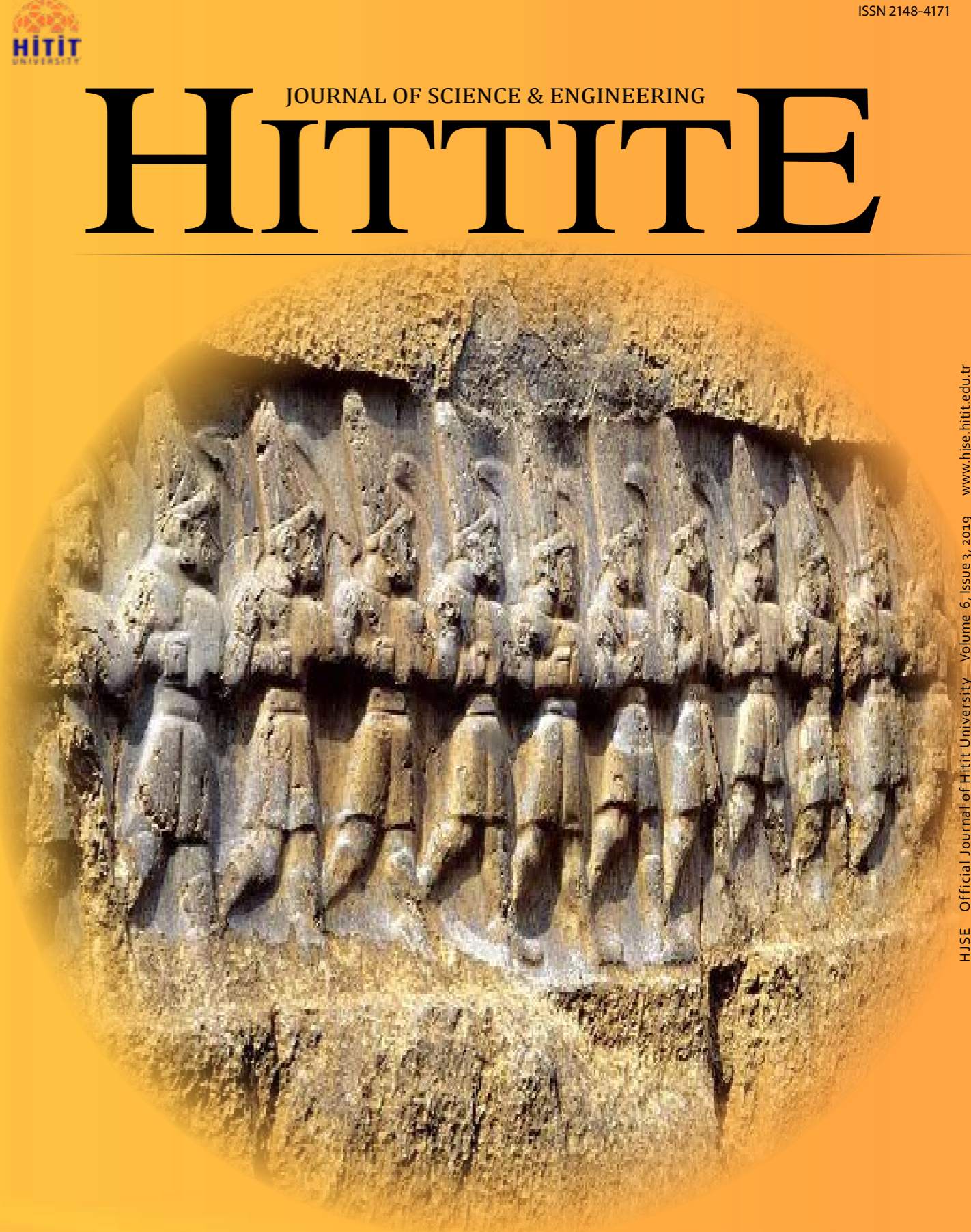
Venue: Radisson Blu Resort & Spa
Location: Cesme, Turkey

Begins: September 22, 2020
Ends: September 25, 2020

HITTITE

JOURNAL OF SCIENCE & ENGINEERING

HJSE Official Journal of Hitit University Volume 6, Issue 3, 2019 www.hjse.hitit.edu.tr



HJSE Official Journal of Hitit University Volume 6, Issue 3, 2019 www.hjse.hitit.edu.tr



Abstracted & Indexed in:

TR Dizin Mühendislik ve Temel Bilimler Veri Tabanı |
CrossRef | Google Scholar | MIP Database | StuartxChange | ResearchBib | Scientific Indexing Services (SIS)

HITTITE

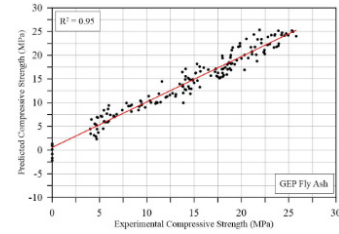
Volume 6, Issue 3, 2019

www.hjse.hitit.edu.tr

Modeling Compressive Strength of Lightweight Geopolymer Mortars by Step-Wise Regression and Gene Expression Programming 157-166

Kasim Mermerdas, Safie Mahdi Olewi and Sallal Rashid Abid

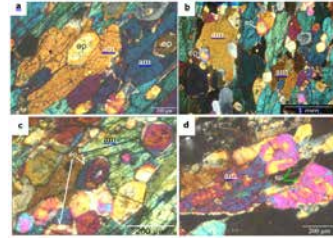
This article presents a comprehensive study aimed at developing suitable mathematical models for the prediction of compressive strength of lightweight geopolymer mortar (LWGM) with different types and amounts binders with different curing regimes.



Chemical and Mineralogical Characteristics of the Microscopic-sized Epidotes in the Metamorphic Basement Rocks within the Late Cretaceous Hatip Ophiolitic Melange in Konya (Central Southern Turkey) 167-172

Kerim Kocak and Merve Kaya

The epidote is suggested to have a possible igneous origin, and to be crystallised from a wet (H₂O>5 wt %) magma under low fO₂ and intermediate pres-sure conditions during initial stage crystallisation on the basis of its petrographical and mineralogical characteristics.



Dietary Exposure Assessment of Aflatoxin From Dried Figs in Turkey

173-177

Hatice Imge Oktay Basegmez

The purpose of the present study is to assess health risk for Turkish adult population posing by dried fig consumption due to the aflatoxin contamination.

Positive sample/ Total Sample (%)	Range of AFTOX (µg/g)	Country	Reference
26/33	0.22-83.4	Algeria	[19]
4/74	LOD*-11.10	Pakistan	[20]
13/22	0.3-7.0	Iran	[21]
16/30	0.1-28.2	Turkey	[22]
219/104 (4.75%) (for export)	ND*-267.48	Turkey	[23]
24/625/80 (23.6%) (from local store)	ND-278.04	Turkey	[23]
11/115	0.1-763.2	Turkey	[24]
343/2643	0.2-162.76	Turkey	[25]
1575/4917	0.2-259.46	Turkey	[25]

*LOD: Limit of Detection, ND: Not Determined

Implementation and Quality Assessment of a User-Centric Adaptation System for DASH 179-184

Nukhet Ozbek and Atilla Aricioglu

This paper presents a novel adaptation system for DASH which is designed to search whether a higher QoE might be achieved if the adaptation method could be user-centric.

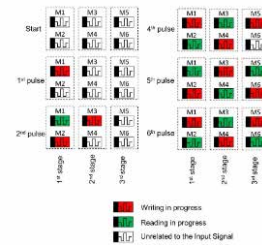


Memristor Based Multi-State Shift Register Architecture

185-191

Dincer Gokcen

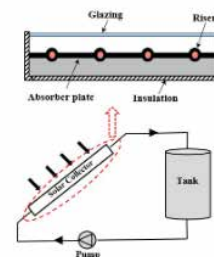
This research presents the use of memristors to build multi-state shift registers.



Performance Assessment of Flat Plate Solar Collector Using Different Nanofluids 193-200

Mustafa Asker and Tukur Sani Gadanya

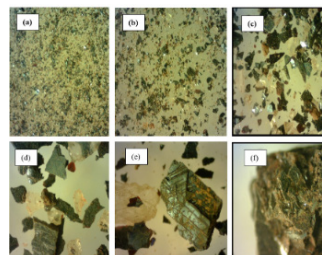
In this work, a numerical study has been performed to investigate the performance of a flat plate solar collector (FPSC) using five different nanofluids including Al₂O₃, CeO₂, Cu, SiO₂, and TiO₂ as the working fluid with a volume fraction (VF) range of 0-2% and mass flow rate of 0.02kg/s.



Effective Processing of Specularite Ore by Wet Magnetic Separation and Reverse Flotation Techniques 201-208

Ammar Mahdi Al-Dhubaibi, Huseyin Vapur and Soner Top

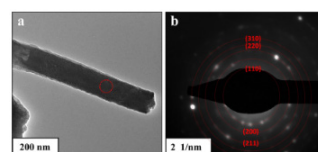
The aim of this study was to obtain a high grade and yield percentage of iron concentrate from a specularite ore by using wet magnetic separation and reverse flotation techniques.



Characterization of Iron Nanowires Fabricated by Electrodeposition into Polycarbonate Template 209-213

Halil Yilmaz and Mustafa Kocabas

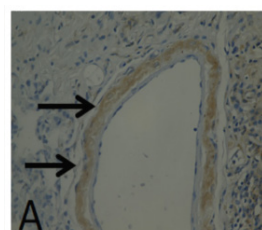
In the present study, commercially available polycarbonate (PC) membranes with different pore diameters were used as a template for electrodeposition of iron nanowires.



The Preventive Effect of Thymoquinone and Ceratonia Siliqua L. in Experimental Asthmatic Pregnant Rats: Histologically and Immunohistochemically Evaluation 215-222

Orhan Zeybek

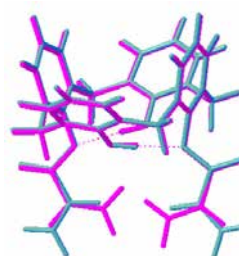
In this study, the use of TQ and CS has been shown to alleviate the histological changes and immunohistochemically caused by asthma.



Computational Insight into Conformational Rearrangement and Intramolecular-H Bond Analysis of Some Calix[4]Arenes Including Acryloyl Moiety 223-228

Selehattin Yilmaz, Burcu Tepeli and Sultan Yagmur

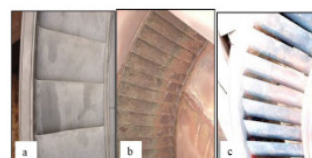
The conformational analyses of Calix[4]arenes reveals four different stable structures (conformations); Cone, Partial Cone, 1,2-Alternate and 1,3-Alternate after employing a density functional theory (DFT) computational analysis.



The Performance of Gas Turbine Power Plant Using 5% Biodiesel & 95% High Speed Diesel 229-233

Mujammil Asdhiyoga Rahmanta, Tiva Winahayu Dwi Hapsari and Bernaded Oka Anggraini

In this study, the effects of biodiesel mixed with HSD were studied using a gas turbine power plant with a capacity of 18 MW.



Owner

Prof. Dr. Ali Osman ÖZTÜRK
on behalf of Hitit University

Editor-in-chief

Prof. Dr. Ali KILIÇARSLAN

Associate Editors

Prof. Dr. D. Ali KÖSE
Assist. Prof. Dr. Öncü AKYILDIZ

Production

Assoc. Prof. Dr. Kazım KÖSE
Mustafa Reşit HABOĞLU
Erhan ÇETİN
Harun Emre KIRAN
Ömer Faruk TOZLU

Editor's Office

Tel: +90 364 227 45 33 / 12 36

Fax: +90 364 227 45 35

Email: alikilicarslan@hitit.edu.tr

Subscription Service:

Tel: +90 364 227 45 33 / 12 82

Fax: +90 364 227 45 35

Email: hjse@hitit.edu.tr

EDITORIAL BOARD

Prof. Dr. İftikhar AHMAD

Prof. Dr. Mike BECKETT

Prof. Dr. İbrahim DİNÇER

Prof. Dr. Ali ELKAMEL

Prof. Dr. Mohamad S QATU

Prof. Dr. Saffa RIFFAT

Prof. Dr. Thanos SALIFOĞLU

Assoc. Prof. Dr. Yuehong SU

Dr. Wojciech NOGALA

Prof. Dr. Yusuf AYZAZ

Prof. Dr. Adil DENİZLİ

Prof. Dr. Ali GENCER

Prof. Dr. Metin GÜRÜ

Prof. Dr. Murat HOŞÖZ

Prof. Dr. Sadık KAKAÇ

Prof. Dr. Tarık Ömer OĞURTANI

Prof. Dr. Ender SUVACI

Assoc. Prof. Dr. Ali TOPÇU

Prof. Dr. Kazım Savaş BAHÇECİ

Assoc. Prof. Dr. Cengiz BAYKASOĞLU

Prof. Dr. Vedat DENİZ

Prof. Dr. Hakan GÜNGÜNEŞ

Prof. Dr. Bülent KABAK

Prof. Dr. Ali KILIÇARSLAN

Prof. Dr. Dursun Ali KÖSE

Prof. Dr. İrfan KURTBAŞ

Assoc. Prof. Dr. Seyfi ŞEVİK

Prof. Dr. Dilber Esra YILDIZ

University of Malakand, Chakdara, Pakistan

Bangor University, Bangor, United Kingdom

Uoit Ontario University, Ontario, Canada

University of Waterloo, Ontario, Canada

Central Michigan University, Michigan, United States

The University of Nottingham, United Kingdom

Aristotle University of Thessaloniki, Thessaloniki, Greece

The University of Nottingham, United Kingdom

Polish Academy of Sciences, Poland

Suleyman Demirel University, Turkey

Hacettepe University, Turkey

Ankara University, Turkey

Gazi University, Turkey

Kocaeli University, Turkey

TOBB University, Turkey

Middle East Technical University, Turkey

Anadolu University, Turkey

Hacettepe University, Turkey

Hitit University, Turkey

Hitit University, Turkey

Hitit University, Turkey

Hitit University, Turkey

Hitit University, Turkey

Hitit University, Turkey

Hitit University, Turkey

Hitit University, Turkey

Hitit University, Turkey

Hitit University, Turkey

Journal Name	: HITTITE JOURNAL OF SCIENCE AND ENGINEERING
Year	: 2019
Managing Editor	: Prof. Dr. Ali KILIÇARSLAN
Managing Office	: Hitit University Faculty of Engineering
Managing Office Tel	: +90 364 227 45 33 / 12 36
Publication Language	: English
Publication Type	: Peer Reviewed, Open Access, International Journal
Delivery Format	: 4 times a year (quarterly)
Print ISSN	: 2149-2123
Online ISSN	: 2148-4171
Publisher Address	: Hitit Üniversitesi Kuzey Kampüsü Çevre Yolu Bulvarı 19030 Çorum / TÜRKİYE
Publisher Tel	: +90 364 227 45 33/1236



This new issue of Hittite Journal of Science and Engineering contains eleven manuscripts from the disciplines of physics, biology, geological engineering, electrical and electronics engineering, mechanical engineering, mining engineering, materials science and engineering. These manuscripts were first screened by Section Editors using plagiarism prevention software and then reviewed and corrected according to the reviewer's comments. I would like to express my gratitude to all our authors and contributing reviewers of this issue.

I would like to thank to the new President of Hitit University, Prof. Dr. Ali Osman Öztürk, for his support and interest in HJSE and also to the Associate Editors of HJSE, namely Prof. Dr. Dursun Ali Kose and Asst. Prof. Dr. Oncu Akyıldız, as well as our Production Editors Dr. Kazım Kose, Mustafa Reşit Haboğlu, Erhan Çetin, Harun Emre Kiran and Ömer Faruk Tozlu for their invaluable efforts in making of the journal.

It's my pleasure to invite the researchers and scientists from all branches of science and engineering to join us by sending their best papers for publication in Hittite Journal of Science and Engineering.

Dr. Ali Kiliçarslan

Editor-in-Chief

Modeling Compressive Strength of Lightweight Geopolymer Mortars by Step-Wise Regression and Gene Expression Programming

Kasım Mermerdaş¹  Safie Mahdi Olewi^{2,3}, Sallal Rashid Abid⁴ 

¹Harran University, Department of Civil Engineering, Sanliurfa, Turkey

²Hasan Kalyoncu University, Department of Civil Engineering, Gaziantep, Turkey

³Diyala University, Department of Civil Engineering, Baqubah, Iraq

⁴University of Wasit, Department of Civil Engineering, Wasit, Iraq

ABSTRACT

This article presents a comprehensive study aimed at developing suitable mathematical models for the prediction of compressive strength of lightweight geopolymer mortar (LWGM) with different types and amounts binders with different curing regimes. Lightweight pumice aggregate, alkali activated powder materials are the main components of geopolymer binder. From the experimental study 306 data samples were obtained and these were used to derive explicit formulas for estimation of the compressive strength of LWGMs. Two methods are used to produce the models. The first is the simplified linear step-wise regression, while the second method is the genetic expression programming. Step-wise regression is a statistical tool that uses the impact of each factor to evaluate its effect on the equation. This impact is calculated based on the probability effect based on the F-distribution and the null-hypothesis. The default value of probability that refers to the significance of each factor is 0.05. Thus, the software calculates the probability of each of the independent variables and includes only those with probability values less than 0.05. Based on the included independent variables, simplified linear regression equation is introduced. The genetic programming on the other hand, is much more sophisticated method that uses the principles of gene evolution. The modeling is separated for each type of binder. Thus, two sets of formulas are obtained from each modeling, one for the granulated blast furnace slag -based LWGM, while the second is for the fly ash-based LWGM. These models revealed that genetic algorithm based modeling has a reliable potential for estimating the strength of LWGMs.

Keywords:

Geopolymer; Ground granulated blast furnace Slag; Fly ash; Lightweight Mortar; Step-Wise Regression; Genetic Modeling

INTRODUCTION

The great need for concrete results in depletion of huge quantities of cement. This causes a manufacture of equal amount of cement with an excessive amount of carbon dioxide emissions. CO₂ emissions from cement production are an important factor causing air pollution. The risk of ecological imbalance should also be taken into account because of the continuous consumption of natural resources. Greenhouse gas emissions from cement production are estimated to be 6-7% of the total [1,2].

Geopolymer, an innovative eco-friendly inorganic binder material obtained using industrial waste powders, can be taken into account as an alternative binder to the cement based system. There are lots of aluminosilicate based materials available in nature. Moreover,

plenty of them are obtained from industrial by products. Hence, the utilization of these substances as binding agents has gained more significance for the construction sector. Therefore, intensive works have been performed to examine the features of composite materials incorporating geopolymer binder [3-6]. Besides, the development of hybrid geopolymer-based materials has been of a critical importance, as well, recently [7-9]. The most commonly used aluminosilicate substance in casting of geopolymer based concrete is FA, GGBFS and calcined kaolin [10-13]. Amongst those, FA and GGBFS are waste materials which can be used as substitutional cementitious materials for the concrete. Due to high CaO content more than 30%, GGBFS provides the formation of calcium silicate hydrate (C-S-H) gel-like structure in geopolymer composites as a result of chemical effect

Article History:

Received: 2019/01/05

Accepted: 2019/09/24

Online: 2019/09/30

Correspondence to: Kasım Mermerdaş
Harran University, Department of Civil
Engineering
E-Mail: kasim.mermerdas@harran.edu.tr

of alkali activators [14-19]. However, with the activation of fly ash by alkalis in order to form the amorphous inorganic polymers, F type FA is commonly desired for the geopolymer production due to provision of a reasonable setting behavior and strength development. The dosage and type of alkali activator is one of governing factors on properties of the gel and its formation [20]. Sodium silicate and NaOH are the most used activating solutions in geopolymer [21 - 24].

Some recent studies have demonstrated that various alkali activators based on sodium silicate and NaOH are useful in improving the mechanical properties of geopolymers containing industrial by-products [25-28]. The glassy nature of the GGBFS phase allows the alkaline to be activated more easily than FA. The presence of a larger crystal phase in FA requires higher temperatures for the accelerated reaction [29]. GGBFS addition to the system has been shown to result in a significant increase in the strength of FA-based geopolymer binders [30, 31].

Going back to the end of 1980's and the beginning of 1990's, the Genetic Algorithms (GAs) and later the Genetic Programming were developed as new evolutionary techniques. The genetic programming is simply the evolution and optimum solving of computer programs (research problems) of domain-independent-subjects from the Darwinian principles, namely, gene survival, reproduction, and evolution. Both genetic algorithms and genetic programming techniques use only single type of individuals or entity to formulate both the genome and phenome types of the problem. In biology, the genome refers to the chromosome that carries all features of the entity, while the phenome is the visualized shape of that entity (the body). In genetic programming, the chromosomes are the individuals, which are fixed-length strings of linear form, while the individuals of GP are parse-trees of nonlinear different shapes and different lengths. The gene expression programming (GEP) on the other hand, uses the two forms, where fixed-length linear-strings are used to encode the individuals during the processing phase. These codes are then translated to nonlinear entities of different shapes and sizes in the post processing phase, which are simplified expression trees. Thus, GEP translates the language of chromosomes into a simple language of expression trees [32].

In GEP, different numbers of different-length and shape and multi-gene chromosomes are used to code the variables of the problem need to be solved. In addition to the main variables of the problems, the program defines constants and mathematical expressions as parts of these chromosomes. The mathematical expressions include all types of possible mathematical operations such as addition, subtraction, multiplication, division, square or higher order roots, squaring or higher powers, logarithms, exponentials, trigonometric

functions, and others. In the start of the evolution process, a fitness function is chosen to evaluate the accuracy of the solution and the errors. This fitness is evaluated at the first step for a random generation. In the subsequent steps, the individuals with best fitness are selected (survived individuals) for reproduction and development of the next generation. The development of each next generation carried out by carrying some or all of several randomly selected operations on the survived (selected based on best fitness) chromosomes and genes from the previous generation. These reproduction operations include replication of survived genes, mutation, partial or gene transportation, and partial or gene recombination. This process continues one generation by another for several hundreds, thousands, or millions of generations until the best fitness of the solution is obtained. The flowchart of the GEP process is illustrated in Fig.1.

Estimation of a dependent variable can be made with the help of mathematical equation obtained by multiple

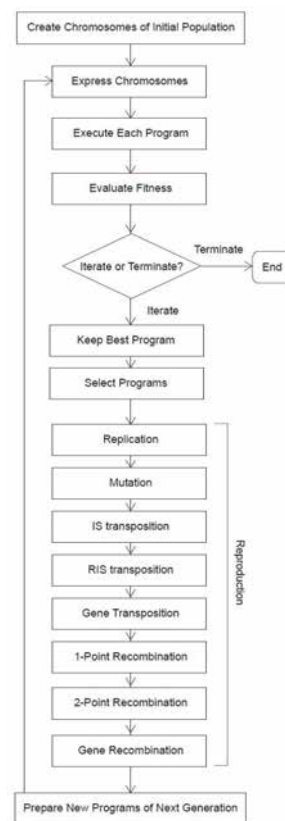


Figure 1. Flowchart of GEP

linear regression analysis. Stepwise regression is a statistical technique of adjusting regression models in which the choice of predictive variables is carried out by an automatic procedure. In each step, a variable is considered for addition to or subtraction from the set of explanatory variables based on some prespecified criterion. In this study, stepwise regression model was preferred among other regression models to compare with the performance of the GEP model derived.

EXPERIMENTAL PROGRAM

The primary focus of the experimental research on compressive strength of LWGM produced by LWFA and by product materials was to investigate the effectiveness of different quantities of binder, curing temperature and time. However, derivation of prediction models to skip time and effort consuming experimental stage. This provides a basis for the motivation of the current study.

In the preliminary study it was determined that utilization of lightweight fine aggregate (LWFA) by itself, had no problem of workability and consistency of the mix. Furthermore, the other challenges, for instance, separation of the large particles, demolding of the samples and comparatively lower compressive strength values obtained directed the authors to make a decision on beneficiation of crushed lime stone sand together with LWFA in the LWGM mixtures.

Materials

Since LWFA is decided to be used for production of LWGM, the fraction of the total aggregate volume for LWFA was taken as 70%, while 30% was considered for limestone aggregate. The grading of LWFA is coarser than crushed limestone aggregate. The details on physical and grading properties of the aggregates can be found in [32].

The LWFA were immersed in water to obtain 100% saturation before mixing with the other ingredients. The excessive moisture on the surface of the aggregates was dried to get saturated surface dry condition. The result of the experimental study on the water absorption capacity of LWFA was shown in Table 1. It was observed that maximum saturation level is 26.6%.

For the production of geopolymer binders, two pozzolanic materials, namely FA and GGBFS, were activated by alkalis. ASTM C618 F class FA was obtained from Ceyhan

Table 1. Water absorption for lightweight aggregate

Soaked in water (hour)	0.5	1	2	6	24	48	72
Water absorption %	20.689	21.275	22.463	24.113	26.628	26.719	26.81

Sugozu thermal power plant. In addition, GGBFS meeting the eligibility criteria specified in ASTM C 989 was used. As the alkaline activator mixture of Na_2SiO_3 and a 12 M NaOH solution in proportions of 1: 2.5 was used. The ratio of the alkali solution to the binder is equal to 0.50. The composition of the sodium silicate solution was selected to provide the optimal activation. The optimal activation is stated to be the highest geopolymerization level [32]. Accordingly, sodium silicate solution contains 29.4% SiO_2 , 14.7% Na_2O and 55.99% water. The polycarboxylic ether based plasticizer

was used to provide a consistent workability to the LWGM mortar and was taken as 5% of the binder.

Mix design

In the experimental program, mix proportion with the different amounts of ingredients, the effect of six levels curing time and four ranges curing temperature on the compressive strength of LWGM mortar were considered. The amounts of alkaline activator solution and the ratio of sodium silicate to sodium hydroxide solution was constant. The mixture proportions of mortars are presented in the previous study conducted by the authors [32]. All the mixtures of LWGMs were designed with alkaline solution only as the liquid component in the mixture. No additional water, Therefore to improve the workability and to make LWGM mix as a homogeneous mix an super plasticizer with specific gravity of 1.07 is added to the mix.

Mixing, Casting, and Curing regime

After preparing the alkaline liquids, a predetermined mixing procedure was applied as described in the previous study [32]. The fresh LWGM was poured in two layers in the moulds (50 x 50 x 50 mm). To provide the fresh with a proper compaction, a laboratory type vibrating table was used. The specimens were wrapped with heat resistant thin plastic film as shown in Fig. 2 to avoid evaporation of water.

Next, all the mixtures of FA and GGBFS based LWGM were placed in an oven under curing temperatures of 60, 80, 100 and 120 °C for accelerated curing periods of 2, 6, 8, 24, 48 and 72 h. Fig. 2 shows the specimens curing in the oven. Then specimens were demolded after the curing process and the specimens were tested.



Figure 2. Mortar curing.

EXPERIMENTAL TEST RESULTS

In this section, the data from the experimental work conducted in the previous work [32] are used to introduce modeling formulas for the compressive strength of geopolymer mortar (Table 2). Two methods are used to generate these formulas. The first is the simplified linear step-wise regression, while the second method is the genetic expression programming.

The compressive strength value was used as dependent variable, while curing time, temperature, and binder content are used as predictors.

Table 2. Compressive strength values of LWGMs with different binder amounts, curing time and curing temperature.

Mix ID.	Accelerated curing temperature(C°)	Time(h)	Compressive strength for different binder content (MPa)						
			650	750	850	950	1050	1150	1250
GGBFS based LWGM	60	2	6.89	8.56	9.12	10.68	8.45	10.8	12.55
		6	18.45	21.33	24.5	22.75	24.3	27.53	28.45
		8	19.8	23.39	26.14	28.05	29.6	28.92	29.44
		24	26.02	28.13	29.12	31.08	31.83	32.91	34.1
		48	27.5	30.76	32.07	33.98	32.6	35.98	38.01
		72	29.4	31.4	31.67	32.71	33.82	35.4	36.49
	80	2	11.16	12	12.63	11.08	16.73	11.35	16.37
		6	20.28	23.7	21.27	24.34	27.93	26.93	30.16
		8	23.28	24.74	27	27.33	29.4	28.25	31.12
		24	27.81	28.41	30.16	29.52	31.83	32.91	32.71
		48	29.8	29.3	31	30.88	32.27	34.1	35.54
		72	31.47	30.88	30.32	30.2	33.42	35.26	36.06
	100	2	14.74	20.92	22	22.51	25.62	26.39	23.89
		6	21.51	26.29	27	29.96	27.97	29.4	27.86
		8	23.39	27.21	29	30.04	29.32	29.72	29.96
		24	24	29.36	30	30.72	30.35	31.27	30.6
		48	26.1	29.79	30.6	31	30.9	31.95	32.51
		72	26.69	30.08	30.1	31.04	31.4	32.83	29.64
	120	2	18.37	21.39	23.19	22.47	27.16	27.37	28.25
		6	20.22	23.71	25.42	25.34	27.73	27.77	27.85
		8	21	24	26.73	24.82	26.93	27.49	28.61
		24	22.5	24.47	27	25	27.33	28	28.8
		48	22.71	24.62	27.49	26.57	28	28.5	31.2
		72	21.2	23.98	26.97	24.94	30.32	29.46	28.65
FA based LWGM	60	2	0	0	0	0	0	0	0
		6	4.7	4.42	4.74	5.62	5.26	5.78	6.81
		8	4.86	5.38	5.86	6.14	5.9	8.25	9.2
		24	9.44	10.32	12.71	13.78	14.38	18.45	18.13
		48	13.47	14.5	15.66	18.69	18.88	21.12	22.35
		72	14.1	15.3	17.97	19.68	21.71	23.51	25.78
	80	2	4.62	4.06	4.02	4.5	4.14	4.74	4.82
		6	5.97	6.61	9.12	10.44	13.03	13.85	14.6
		8	6.5	8.37	9.48	12.15	14.14	14.4	15.6
		24	11.28	14.7	15.34	17.21	19.28	19.5	21.64
		48	17.68	18	18.5	20.32	21	22.1	23
		72	18.08	19	21.56	22.76	22.8	24.3	24.72
100	2	4.58	5.5	5.14	5.46	5.98	7.85	10.92	
	6	8.05	9.4	13.07	13.75	14.86	17.37	17.5	
	8	9.32	10.2	14.5	14.65	15.18	18.53	18.9	
	24	11.6	14.1	16.02	18	18.97	19.84	21.43	
	48	13.75	15.58	18.84	23.43	22.11	24.22	24.54	
	72	17.29	18.65	22.47	23.94	23.15	25.34	25.46	
120	2	4.69	5.46	6.49	7.41	8.41	11	13.86	
	6	9.82	11.12	12.43	13.82	14.06	16.77	18.05	
	8	11.45	12	14.02	14.86	17.53	17.93	20.32	
	24	15	17.8	18.76	20	22.43	23.9	23.71	
	48	15.15	18.29	20.72	19.08	20.52	23.55	24.94	
	72	16.5	18.9	21.12	19.84	21.31	21.91	23.9	

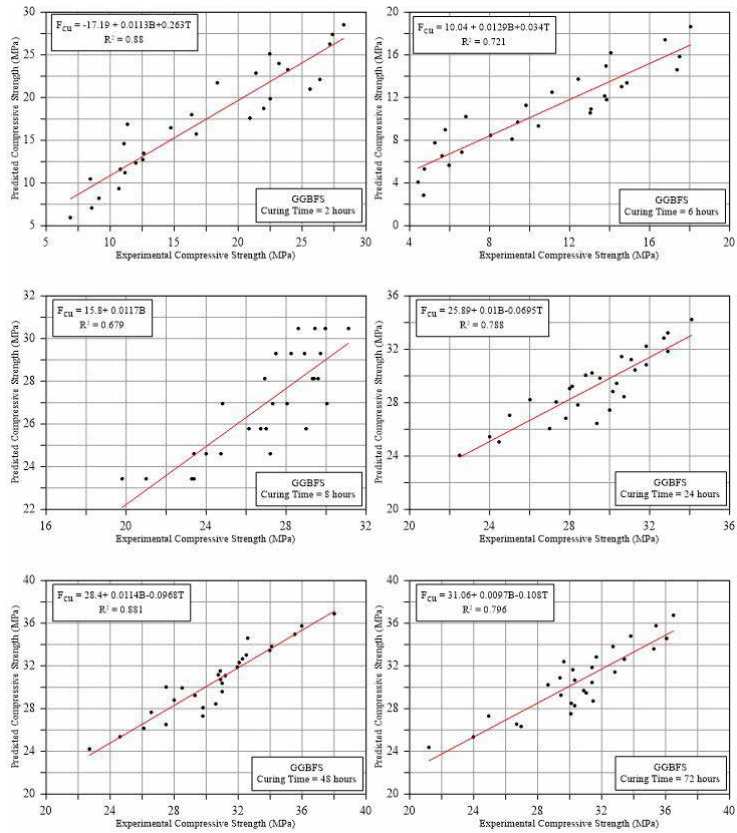


Figure 3. Step-wise formula of compressive strength versus GGBFS binder content and curing temperature for different curing times

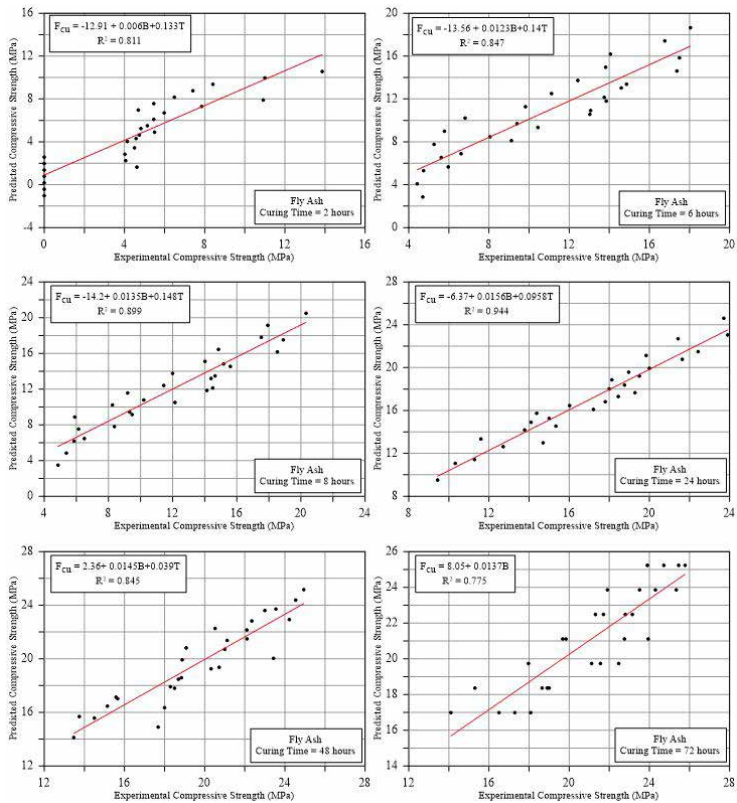


Figure 4. Step-wise formula of compressive strength versus fly ash binder content and curing temperature for curing time of 72 hours

STEP-WISE REGRESSION BASED COMPRESSIVE STRENGTH MODELING OF LWGM

Step-Wise Regression Relationships of Compressive Strength vs. Binder and Temperature for Various Curing Periods

In this section, the strength is correlated with both of the amount of binder and the curing temperature for different curing periods. Fig. 3 shows the conducted linear step-wise regressions for curing periods of 2, 6, 8, 24, 48, and 72 hours for both GGBFS and fly ash binders.

Fig. 3 shows the correlations of the strength values obtained from GGBFS based LWGM with the curing temperature and the binder content for different curing periods. In the formulas shown in Fig. 3, the binder contents vary from 650 kg/m^3 to 1250 kg/m^3 , with steps of 100 kg/m^3 . On the other hand, the included curing temperatures were 60, 80, 100, and 120°C . As shown in the figure, although the regression is linear, the determination coefficients (R^2) were good for all curing periods. The determination coefficients (R^2) for curing periods of 2, 6, 8, 24, 48, and 72 hours were approximately 0.88, 0.72, 0.68, 0.79, 0.88, and 0.8, respectively.

The correlations between compressive strength of fly ash-based geopolymer and both of binder (fly ash) content and the curing temperature are shown in Fig. 4 for curing periods of 2, 6, 8, 24, 48, and 72 hours. It is clear that these relations have better determination coefficients than those of GGBFS-based geopolymer. The determination coefficients for curing periods of 2, 6, 8, 24, 48, and 72 hours range from approximately 0.78 to approximately 0.94, while those of GGBFS were in the range of 0.68 to 0.88.

Step-Wise Regression Relationships of Compressive Strength Vs. Binder and Curing Time for Various Curing Temperatures

In this section, for each temperature, the strength of LWGM is correlated to binder content and curing period for different curing temperatures. The curing temperatures are 60, 80, 100, and 120°C . Similar to the previous section, all formulas were found based on the binder content. The regression equations for GGBFS-based geopolymer are shown in Fig. 5, while Fig. 6 shows the regression equations of fly ash-based geopolymer.

It is clearly obvious that the degree of confidence of this set of equations is much lower than of that for different curing periods. In the equations predicted for different curing temperatures the coefficients of determination are mostly lower than 0.6, while for those of different curing periods, the lowest R^2 is 0.66. The values of R^2 for compressive strength of GGBFS-based geopolymer for curing temperatures of 60, 80, 100, and 120°C are approximately 0.56, 0.54, 0.53 and 0.79, respectively, as shown in Fig. 5.

As it is clear in Fig. 6, the determination coefficients of the compressive strength of fly ash-based geopolymer for different curing temperatures are better than their corresponding values with GGBFS binder. The coefficients of determination of compressive strength versus binder content and curing time for curing temperatures of 60, 80, 100, and 120°C are approximately 0.83, 0.81, 0.8, and 0.69, respectively.

Step-Wise Regression Relationships of Compressive Strength vs. Binder, Curing Temperature, and Curing Time

In the previous sections, regression equations for compressive strength of geopolymer concrete based on only

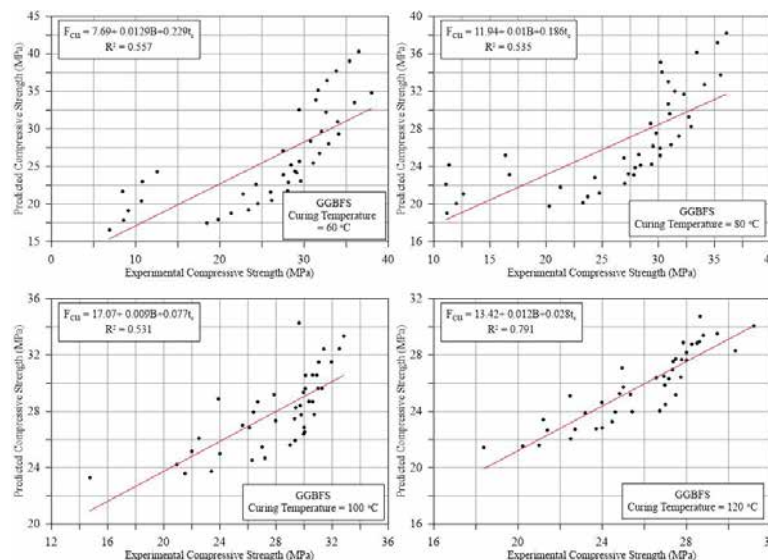


Figure 5. Step-wise formula of compressive strength versus GGBFS binder content and curing time for curing temperature of 120°C

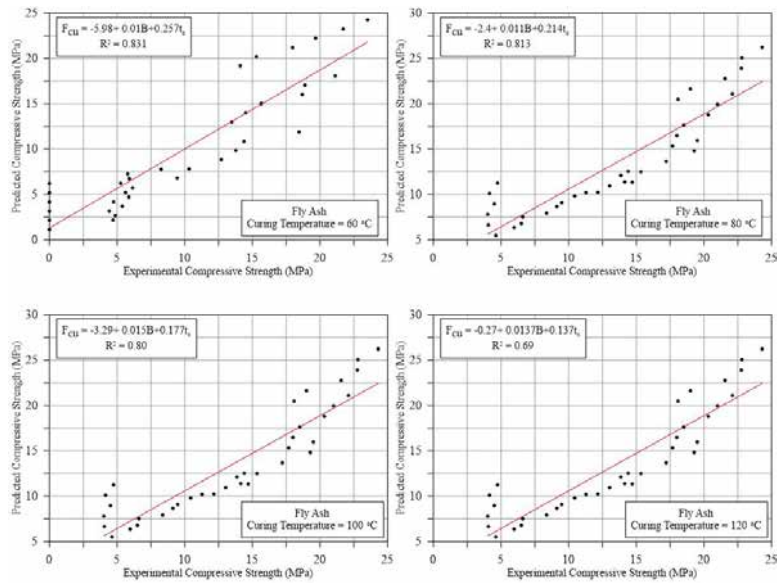


Figure 6. Step-wise regression formula for compressive strength versus fly ash binder content and curing time for curing temperature of 100 °C

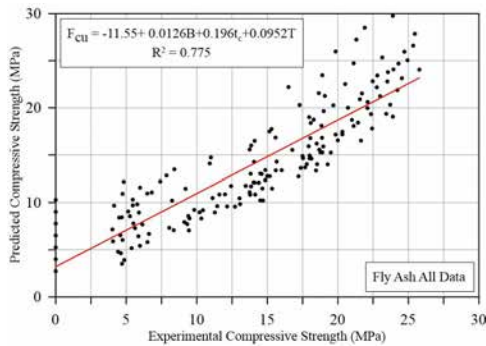


Figure 7. Step-wise regression formula for compressive strength versus fly ash binder content, curing temperature, and curing time

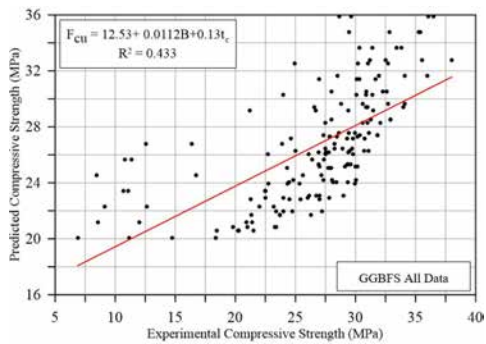


Figure 8. Step-wise regression formula for compressive strength versus GGBFS binder content, curing temperature, and curing time

two independent variables were obtained using linear step-wise regression. In this section, the compressive strength is correlated with the three independent variables at once. Thus, compressive strength is correlated to binder content, curing temperature, and curing time. Fig. 7 shows the experimental versus predicted compressive strength values for all experimental data of the FA based LWGMs. The coefficient of determination of this equation is approximately 0.78, which is quite good. Contrarily,

for the GGBFS-based geopolymer concrete, the step-wise regression showed that curing temperature was insignificant with probability value greater than 0.05. Therefore, the equation was in terms of binder content and curing time only. However, the R^2 was as low as 0.43 (Fig. 8). In order to make a broad comparison of the prediction performance all of the derived step-wise regression formulas are presented in Table 3.

Table 3. Comparison of step-wise regression formulations.

Mix ID	Definition	Step-wise regression formulas	R^2
GGBFS based LWGMs	Curing time = 2 hrs.	$F_{cu} = 17.19 + 0.0113B + 0.263T$	0.88
	Curing time = 6 hrs.	$F_{cu} = 10.04 + 0.0129B + 0.034T$	0.721
	Curing time = 8 hrs.	$F_{cu} = 15.8 + 0.0117B$	0.679
	Curing time = 24 hrs.	$F_{cu} = 25.89 + 0.01B + 0.0695T$	0.788
	Curing time = 48 hrs.	$F_{cu} = 28.4 + 0.0114B + 0.0968T$	0.881
	Curing time = 72 hrs.	$F_{cu} = 31.06 + 0.0097B + 0.108T$	0.796
	Curing temperature = 60 °C	$F_{cu} = 7.69 + 0.0129B + 0.229 t_c$	0.557
	Curing temperature = 80 °C	$F_{cu} = 11.94 + 0.01B + 0.186 t_c$	0.535
	Curing temperature = 100 °C	$F_{cu} = 17.07 + 0.009B + 0.077 t_c$	0.531
	Curing temperature = 120 °C	$F_{cu} = 13.42 + 0.012B + 0.28 t_c$	0.791
	All data	$F_{cu} = 12.53 + 0.0112B + 0.13 t_c$	0.433
	FA based LWGMs	Curing time = 2 hrs.	$F_{cu} = -12.91 + 0.006B + 0.133T$
Curing time = 6 hrs.		$F_{cu} = -13.56 + 0.0123B + 0.14T$	0.847
Curing time = 8 hrs.		$F_{cu} = -14.2 + 0.0135B + 0.148T$	0.899
Curing time = 24 hrs.		$F_{cu} = -6.37 + 0.0156B + 0.0958T$	0.944
Curing time = 48 hrs.		$F_{cu} = 2.36 + 0.0145B + 0.039T$	0.845
Curing time = 72 hrs.		$F_{cu} = 8.05 + 0.0137B$	0.775
Curing temperature = 60 °C		$F_{cu} = -5.98 + 0.01B + 0.25 t_c$	0.831
Curing temperature = 80 °C		$F_{cu} = -2.4 + 0.0118B + 0.214 t_c$	0.813
Curing temperature = 100 °C		$F_{cu} = -3.29 + 0.015B + 0.177 t_c$	0.80
Curing temperature = 120 °C		$F_{cu} = -0.27 + 0.0137B + 0.137 t_c$	0.69
All data		$F_{cu} = -11.55 + 0.0126B + 0.196 t_c + 0.0952T$	0.775

GENE EXPRESSION PROGRAMMING BASED COMPRESSIVE STRENGTH MODELING OF LWGM

In this section, the Gene Expression Programming (GEP) is used to evaluate the effects of the studied three parameters (binder content, curing temperature, and curing time) on compressive strength of LWGM. As in the previous section, the evaluation is in the form of a regression formula based on the type of binder. Thus, two formulas are to be conducted in this section, one for the FA based geopolymer, while the other is for GGBFS-based LWGM.

Although two third of the data were used as training and the rest were taken as testing data sets, for analysis of the results, all of them were considered to be a single cluster.

Gene expression programming (GEP), invented by Candida Ferreira [33], uses softwares by statements of the acquired models or presented knowledge [34]. Genetic programming, introduced by Koza [35], is a application of GAs [36]. Solving defined problem by employing a computer program is a commonly used solution. The definition of the problem is the first step in the logic of GP and GAs, and then the program runs to work out the problem in a problem-independent mode [36]. GEP is derived as an enhanced form of aforementioned genetic operators. These three algorithms use almost same genetic operators in the solutions with unimportant differences. Ferreira [33] states that the differences between the three algorithms denoted as “in GAs the individuals are linear strings of fixed length (chromosomes); in GP the individuals are nonlinear entities of different sizes and shapes (parse trees); and in GEP the individuals are encoded as linear strings of fixed length (the genome or chromosomes) which are afterwards expressed as nonlinear entities of different sizes and shapes (i.e., expression trees (ETs) or simple diagram representations)”.

In this section, the GEP is used for formulation-based modeling of the compressive strength of the LWGM based on the experimental results of this study. This formulation is carried out based on the binder type, while binder content, curing temperature, and curing period are kept variables. Thus, two formulas are obtained using GEP. The first is for the compressive strength of fly ash-based LWGM, while the second is for the GGBFS-based LWGM. In both of which, the compressive strength is nonlinearly evaluated based on the binder content, the curing temperature, and the curing period as expressed in Equation 1. The total number of compressive strength results used in GEP for each binder was 168. The fitness function used in the GEP in this study is the coefficient of determination (R^2), which was also used in the step-wise regression in this study. The software named GeneXproTools.5.0 was benefited for derivation of the model, while Minitab 17 was used as statistical software for

stepwise regression modelling.

$$F_{cu} = f(B, T, t_c) \quad (1)$$

In the GEP carried out in this study, thirty chromosomes each of 3 genes and head length of 7 were used, while the addition was used as the linking function to link the resulted expression trees. Thus, each resulted equation will be composed of three expression trees linked by addition. To simplify the resulted functions, only a limited set of mathematical operations were selected. These are square root, cubic root, squaring, cubing, natural logarithm, exponential, sin, and cosine as well as basic mathematical operations.

Fig. 9 shows the resulted expression trees of the strength of FA based samples, while Fig. 10 shows the expression trees of that of GGBFS samples. In these figures and the following equations, the parameters d_0 , d_1 , d_2 refer to the variables of the equation, which are the binder content (B), the curing temperature (T), and the curing time (t_c), respectively, while C_0 and C_1 are constants of each sub-equation.

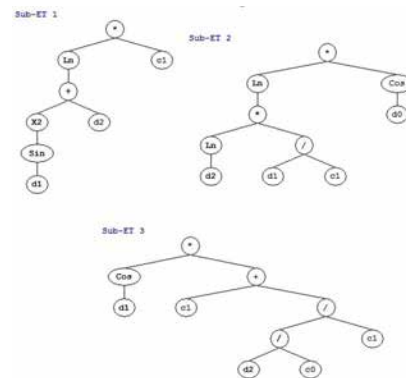


Figure 9. Resulted expression trees of compressive strength of fly ash-based geopolymer samples.

Equation 2 is the GEP prediction formula for the fly ash-based mortar, while Equation 3 is the prediction formula of compressive strength of the GGBFS based mortar.

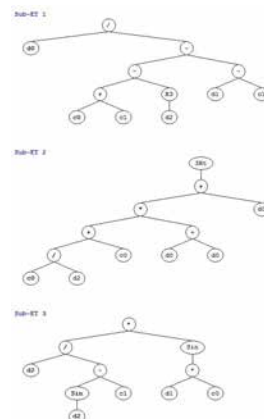


Figure 10. Resulted expression trees of compressive strength of GGBFS-based geopolymer samples.

Equations 2 and 3 are obtained from the expression trees illustrated in Figs. 9 and 10.

The obtained prediction values versus experimental ones are graphically demonstrated in Fig. 11 and Fig. 12 for FA based and GGBFS based LWGMs, respectively.

$$F_{cu} = F_1 + F_2 + F_3 \quad (2)$$

$$F_1 = c_1 \ln[(\sin d_1)^2 + d_2] \quad (2a)$$

Where $C_o = 4.00769$ and $C_1 = 4.87732$

$$F_2 = \cos d_o \ln \left[\frac{d_1}{C_1} \ln d_2 \right] \quad (2b)$$

Where $c_o = -5.881989$ and $c_1 = 6.77649$

$$F_3 = \cos d_1 \left[c_1 + \frac{d_2 / C_o}{C_1} \right] \quad (2c)$$

Where $c_o = -4.005798$ and $c_1 = 4.376678$

Where F_1 , F_2 , and F_3 are the sub-function resulted from each sub-expression trees shown in Fig. 9, respectively, and connected by the addition linking function.

Equation 2 yielded a coefficient of determination of (R^2)0.95. as shown in Fig. 11, which is much better than that of stepwise regression, which was 0.775. This reveals the power of GEP compared to regression formulas. However, Equation 3 had a coefficient of determination of 0.866. Although it is slightly less than the former, it is even so better than that of the prediction model expressed by linear step-wise regression (0.433). This assures that GEP is much powerful than traditional statistical regression tools.

$$F_{cu} = F_1 + F_2 + F_3 \quad (3)$$

Where F_1 , F_2 and F_3 are given by Equations (7), (8), and (9), respectively.

$$F_1 = d_o / \left[(c_o + c_1 - d_2^3) - (d_1 - c_1) \right] \quad (3a)$$

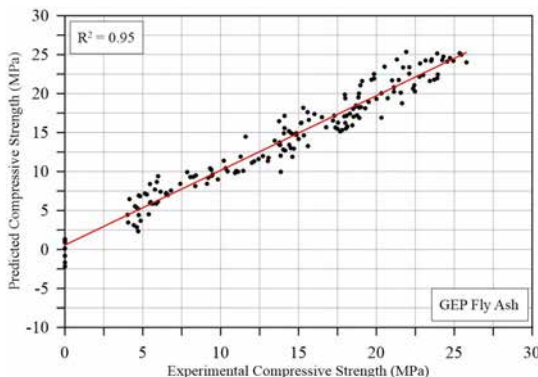


Figure 11. GEP prediction vs experimental compressive strength of FA-based-LWGM (168 specimens)

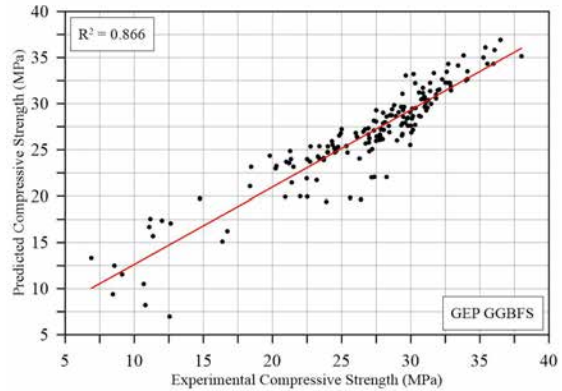


Figure 12. GEP predicted vs experimental compressive strength of GGBFS-based-LWGM compressive strength of 168 specimens.

Where $c_o = 7.316192$ and $c_1 = 7.221954$

$$F_2 = \sqrt[3]{2d_o \left(c_o + \frac{C_o}{d_2} \right) + d_o} \quad (3b)$$

Where $c_o = 9.992737$ and $c_1 = -5.524353$

$$F_3 = \left[d_2 / (\sin d_2 - C_1) \right] \sin C_o d_1 \quad (3c)$$

Where $c_o = 7.880677$ and $c_1 = -9.897583$

CONCLUSION

The GEP prediction formulas for the fly ash and GGBFS-based lightweight LWGM were compared to those obtained from stepwise regression. The GEP equation for FA based LWGM has a coefficient of determination of $R^2 = 0.95$ which is much better than that of stepwise regression, which was 0.775. This reveals the power of GEP to predict regression formulas. The analyses have also indicated that GEP prediction compressive strength values for GGBFS-based LWGM were quite closer to the experimental ones than traditional statistical regression tools.

For future studies other powerful soft computing techniques may be utilized for derivation of estimation models for such construction materials. These tools are artificial neural networks, artificial neuro fuzzy inference systems, fuzzy logic etc. However, the GEP model exploits the input data as they are i.e. without needing preprocessing before they are introduced to the software. Therefore, this method may be considered as a more user friendly technique than the other modeling methods. However, when the accuracy of the prediction values are taken into account, then the utilization of the sophisticated techniques become more prominent. In such cases, the possible solution offered may be the computerization of the complicated models through special softwares. In such a way, the disadvantage due to the complexity of the estimation models can be eliminated.

REFERENCES

1. Davidovits J. Global Warming Impact on the Cement and Aggregate Industry. *World Resource review* 6(2) (1995) 263-278.
2. Turner LK, Collins FG. Carbon dioxide equivalent (CO₂-e) emissions: A comparison between geopolymer and OPC cement concrete. *Construction and Building Materials* 43 (2013) 125-130.
3. Cristelo N, Tavares P, Lucas E, Miranda T, Oliveira D. Quantitative and qualitative assessment of the amorphous phase of a Class F fly ash dissolved during alkali activation reactions – Effect of mechanical activation, solution concentration and temperature. *Compos Part B Eng.* 103 (2016) 1-14.
4. Zivica V, Palou MT. Physico-chemical characterization of thermally treated bentonite. *Compos Part B Eng.* 68 (2015) 436-445.
5. Masi G, Rickard WDA, Bignozzi MC, van Riessen A. The effect of organic and inorganic fibres on the mechanical and thermal properties of aluminate activated geopolymers. *Compos Part B Eng.* 76 (2015) 218-228.
6. Kheradmand M, Mastali M, Abdollahnejad Z, Pacheco-Torgal F. Experimental and numerical investigations on the flexural performance of geopolymers reinforced with short hybrid polymeric fibres. *Compos Part B Eng* 126 (2017) 108-118.
7. Roviello G, Menna C, Tarallo O, Ricciotti L, Messina F, Ferone C, Asprone D, Cioffi R. Lightweight geopolymer-based hybrid materials. *Compos Part B Eng.* 128 (2017) 225- 237.
8. Nematollahi B, Sanjayan J, Shaikh FUA. Matrix design of strain hardening fiberr reinforced engineered geopolymer composite. *Compos Part B Eng.* 89 (2016) 253-265.
9. Yan S, He P, Jia D, Wang J, Duan X, Yang Z, Wang S, Zhou Y. Effects of high temperature heat treatment on the microstructure and mechanical performance of hybrid Cf- SiCf-(Al₂O₃p) reinforced geopolymer composites. *Compos Part B Eng.* 114 (2017) 289-298.
10. Pacheco-Torgal F, Labrincha JA, Leonelli C, Palomo A, Chindaprasirt P. *Handbook of alkali-activated cements, mortars and concretes*, Woodhead Publishing, Cambridge, 2015.
11. Aydın S, Baradan B. Effect of activator type and content on properties of alkali activated slag mortars. *Compos Part B Eng.* 57 (2014) 166-172.
12. Kürklü G. The effect of high temperature on the design of blast furnace slag and coarse fly ash-based geopolymer mortar. *Compos Part B Eng.* 92 (2016) 9-18.
13. Aydın S, Baradan B. The effect of fiber properties on high performance alkali-activated slag/silica fume mortars. *Compos Part B Eng.* 45(1) (2013) 63-69.
14. Glukhovskiy VD, Rostovskaja GS, Rumyna GV. High strength slag-alkaline cements, 7th International Congress on the Chemistry of Cements, Paris, pp. 164-168, 1980.
15. Kutti T, Malinowski R, Srebrenik M. Investigation of mechanical properties and structure of alkali activated blast furnace slag mortars. *Silicates Industriels* 6 (1982) 149-158.
16. Fernandez-Jimenez A, Puertas F, Arteaga A. Determination of kinetic equations of alkaline activation of blast furnace slag by means of calorimetric data. *J. Therm. Anal. Calorim.* 52 (1998) 945-955.
17. Balçıklı M, Özbay E. Optimum design of alkali activated slag concretes for the low oxygen/chloride ion permeability and thermal conductivity. *Compos Part B Eng.* 91 (2016) 243-256.
18. Yip CK, Lukey GC, van Deventer JSJ. The coexistence of geopolymeric gel and calcium silicate hydrate at the early stage of alkaline activation. *Cem. Concr. Res.* 35(9) (2005) 1688-97.
19. Yip C, van Deventer J. Microanalysis of calcium silicate hydrate gel formed within a geopolymeric binder. *J. Mater. Sci.* 38(18) (2003) 3851-60.
20. Juenger MCG, Winnefeld F, Provis JL, Ideker JH. Advances in alternative cementitious binders, *Cem. Concr. Res.* 41(12) (2011)1232-43.
21. Lloyd N, Rangan B. Geopolymer concrete with fly ash. In: *Second international conference on sustainable. Const, Mater. and Tech.* (2010) 1493-504.
22. Komnitsas K, Zaharaki D. Geopolymerization: a review and prospects for the minerals industry, *Miner. Eng.* 20(14) (2007) 1261-77.
23. Tempest B, Sanusi O, Gergely J, Ogunro V, Weggel D. Compressive strength and embodied energy optimization of fly ash based geopolymer concrete, In: *Proceedings of the 2009 world of coal ash (WOCA) conference Lexington, KY, USA, 2009.*
24. Singh PS, Trigg M, Burgar I, Bastow T. Geopolymer formation processes at room temperature studied by ²⁹Si and ²⁷Al MAS-NMR, *Mater. Sci. Eng.* 396(1- 2) (2005) 392-402.
25. Kumar S, Kumar R, Mehrotra SP. Influence of granulated blast furnace slag on the reaction, structure and properties of fly ash based geopolymer *J. Mater. Sci.* 45 (3) (2010) 607-615.
26. Rashad AM. Properties of alkali-activated fly ash concrete blended with slag, Iran. *J. Mater. Sci. Eng.* 10 (1) (2013) 57-64.
27. Ismail I, Bernal SA, Provis JL, San Nicolas R, Hamdan S, van Deventer JS. Modification of phase evolution in alkali-activated blast furnace slag by the incorporation of fly ash. *Cem. Concr. Compos.* 45 (2014) 125-135.
28. Garcia-Lodeiro I, Fernández-Jiménez A, Palomo A. Hydration kinetics in hybrid binders: early reaction stages, *Cement Concr. Compos.* 39 (2013) 82- 92.
29. van Jaarsveld J, van Deventer J. The effect of metal contaminants on the formation and properties of waste-based geopolymers. *Cem. and Concr. Res.* 29(8) (1999) 1189-1200.
30. Ismail I, Bernal SA, Provis J, San Nicolas R, Brice DG, Kilcullen AR, van Deventer JS. Influence of fly ash on the water and chloride permeability of alkali activated slag mortars and concretes. *Constr. Build. Mater.* 48 (2013) 1187- 1201.
31. Parthiban K, Saravanaramohan K, Shobana S, Bhaskar AA. Effect of replacement of slag on the mechanical properties of fly ash based geopolymer concrete, *Int. J. Eng. Technol.* 5 (3) 2555-2559, 2013
32. Mermerdaş K, Algin Z, Oleiwi SM, Nassani DE. Optimization of lightweight GGBFS and FA geopolymer mortars by response surface method, *Construction and Building Materials* 139 (2017), 159-171.
33. Ferreira C. Gene expression programming; a new adaptive algorithm for solving problems. *Complex Syst* 12(2) (2001) 87-129.
34. Li X, Zhou C, Xiao W, Nelson PC. Prefix gene expression programming. in *Late Breaking Paper at the Genetic and Evolutionary Computation Conference (GECCO)*, Washington, D.C., 2005.
35. Koza JR. *Genetic programming; on the programming of computers by means of natural selection*, MIT Press, USA, 1992.
36. Gen M, Cheng R. *Genetic algorithms and engineering design*, Wiley, USA, 1997.

Chemical and Mineralogical Characteristics of the Microscopic-sized Epidotes in the Metamorphic Basement Rocks within the Late Cretaceous Hatip Ophiolitic Melange in Konya (Central Southern Turkey)

Kerim Kocak¹ Raziye Merve Kaya

Konya Technical University, Department of Geology, Konya, Turkey

ABSTRACT

At the base of the Neotethyan ophiolitic melange, widespread epidote crystals formed in metamorphic rocks of the metamorphic basement, which were experienced a regional metamorphism in green-schist facies conditions. The epidote crystals is subhedral to euhedral, with high Al_2O_3 (26-30 %) and low Fe_2O_3 (5-8%) contents. It is predominantly zoisite ($X_{cz} = 0.46$ to 0.72) and subordinate epidote ($X_{ep} = 0.27-0.53$) in composition, with typical compositional zoning due to variable substitution of Fe^{3+} and Al^{3+} on octahedral sites and sector-zoning. The epidote is suggested to have a possible igneous origin, and to be crystallised from a wet ($H_2O > 5$ wt %) magma under low fO_2 and intermediate pressure conditions during initial stage crystallisation on the basis of its petrographical and mineralogical characteristics.

Keywords:

Epidote; Mineralogy; Chemical zoning; Ophiolite; Konya.

INTRODUCTION

The term epidote $\{Ca_2 Fe_x Al_{3-x} Si_3 O_{12} (OH)\}$ first used in 1801 by Haüy [1], typically forms as a result of medium-temperature alterations of intermediate-basic rocks [2]. However, It is also recognised in various magmatic rocks, e.g. alkaline granite [3], granodiorite, monzogranite [4], tonalite [5], orbicular diorite [6] [7], gabbro [8] and dacite [9]. Epidote can also be developed in eclogites [10], and high-pressure migmatites and pegmatites derived from eclogites [11] [12].

In the SW part of Konya city, widespread epidote minerals occur in the metamorphic basement at the base of Neotethyan ophiolitic melange, which tectonically overlies the Middle Triassic–Upper Cretaceous carbonates (Midostepe and Lorasdağı formations) of the Tauride platform [13] (Fig. 1). The Melange contains Carboniferous-Late Cretaceous carbonates, radiolarian cherts, ultramafic rocks, volcanics and gabbro bodies within sedimentary and sheared serpentinite matrix. Çayırbağı ophiolites obducted onto the melange, and contain various ultramafic rocks, namely, harzburgite, dunite, pyroxenite and gabbro. Substantial magnesite deposits are hosted by serpentinitized harzburgite. The

basement includes various amphibole-bearing metamorphic rocks, namely, amphibolite, epidote-amphibolite, zoisite-amphibolite, garnet-amphibole schist, amphibole schist, plagioclase amphibole schist, plagioclase-epidote-amphibole schist and q-amphibole schist [14]. The contact between the metamorphic basement and the overlying peridotite is represented by 2–3-m-thick, strongly sheared serpentinite and amphibolite schist, with concordant foliation patterns [15]. The metamorphic rocks were subjected to a regional metamorphism in greenschist facies conditions, with development of chlorite and albite crystals. It is aimed to characterize epidote minerals in Ep- amphibolite and zoisite amphibolite using its mineral chemistry.

ANALYTICAL METHODS

From the selected samples, fifty thin sections of were made at thin section laboratory of Department of Geological Engineering (Selcuk University, Konya), and then, their composition and texture were studied under the microscope. Modal mineralogy was determined by point counting (2000-3000 points per thin section, depending on grain size). Chemical

Article History:

Received: 2019/01/10

Accepted: 2019/09/23

Online: 2019/09/30

Correspondence to: Kerim Kocak,
Konya Technical University, Geology,
Konya, TURKEY
E-Mail: kkocak@yahoo.com
Phone: +90 332 2232193
Fax: +90 332 2410635

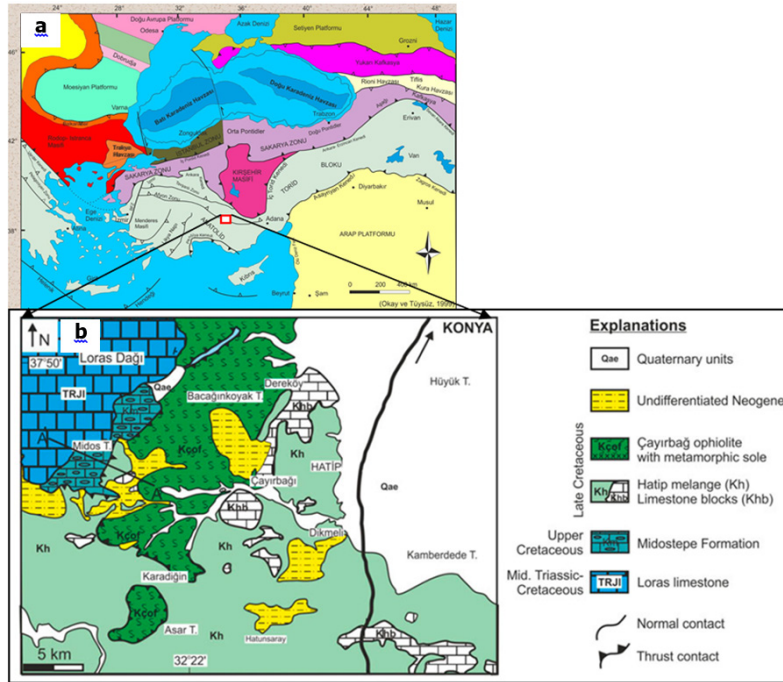


Figure 1. a) Tectonic units of Turkey [16] b) Geological map of the study area [13].

composition of the epidote was determined by electron microprobe at METU, Ankara (Turkey). Operating conditions were kept at an accelerating voltage of 15 kV and a beam current of 20 nA. A beam size of 5 μm was used on amphibole and biotite grains, whereas a defocused beam of 10 μm was used on plagioclase grains to limit Na loss.

PETROGRAPHY

The epidote amphibolite consists of amphibole (0.6 mm, 65.3%), epidote (0.1-0.4 mm 23.47 %), zoisite (0.1-0.3 mm,

5%), plagioclase (5.5 %), quartz (0.7%) and titanite (0.03%) in a granular texture. The amphiboles exhibits typical light and yellowish green colour and pleochroism, and are magnesiohornblende, pargasite and edenite in composition [14]. The epidotes mostly forms as single grain or rarely in aggregate, which is subhedral to euhedral (Fig. 2a), with high (II and III order) birefringence colour. It develops mostly colour-zoned isometric or stubby prismatic (Fig. 2 a, b); the cores are pale yellowish-green and pleochroic, but the rims are nearly colourless. Though it is not common, sector-zoning is also observed in the

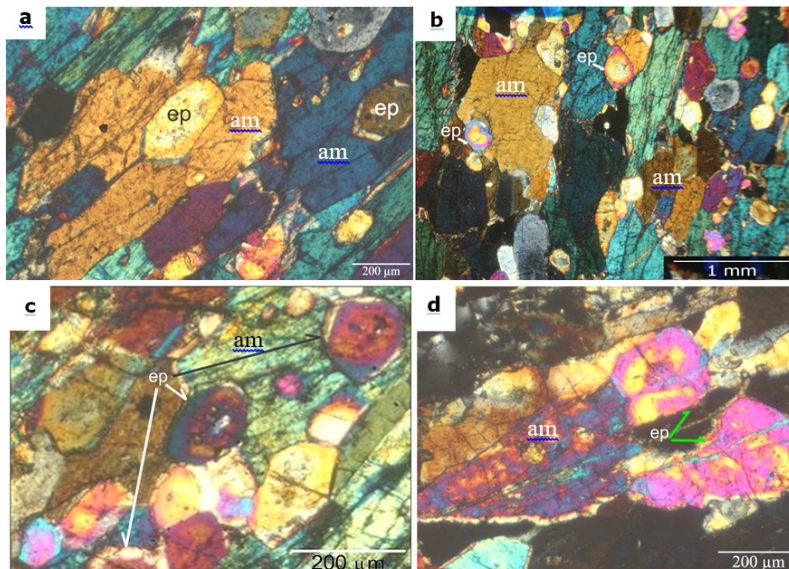


Figure 2. Microphotograph of the epidote amphibolite, ep: epidote, am: amphibole; a) Euhedral epidote (ep) growth within the amphibole, b) epidote replacing the subhedral amphibole. c-d) sector-zoning in the epidote. Cross-Nicholls(XN)

samples (Fig. 2 c, d). The plagioclase is altered to calcite and sericite.

The zoisite amphibolite is composed of amphibole (52.2 %), zoisite (38.4 %), plagioclase (0.5 mm, 7.1 %) and titanite (2.3 %) in a granular texture. The amphibole (0.3-0.7 mm) is predominantly subhedral, and exhibits greenish colour and pleochroism, and resorbed by epidote crystals (Fig. 2a, b). Zoisite (0.3 mm) occurs as aligned anhedral crystals, with low birefringence colour. The titanite (0.4 mm) forms as rhomboeder crystals, and exhibit brownish colour due to its FeO content.

MINERAL CHEMISTRY

Chemical compositions of the epidotes are presented in Table 1, which has limited compositional range of pistacite [$XPs = Fe^{3+}/(Fe^{3+} + Al) \times 100$] of 7% and 16% Fig. 3), and of $CaO = 23.4-25.5$ wt%. The epidote minerals contain minor amounts of TiO_2 (0.05 to 0.31, with an average of 0.18 wt %), MnO (0.01 to 0.17 wt %) and MgO (0.0 to 0.4, with an average of 0.12 wt%). But they are distinguished from typical epidotes [2] with higher contents of Al_2O_3 (26-30 against 20.32%) and lower contents of Fe_2O_3 (5-8

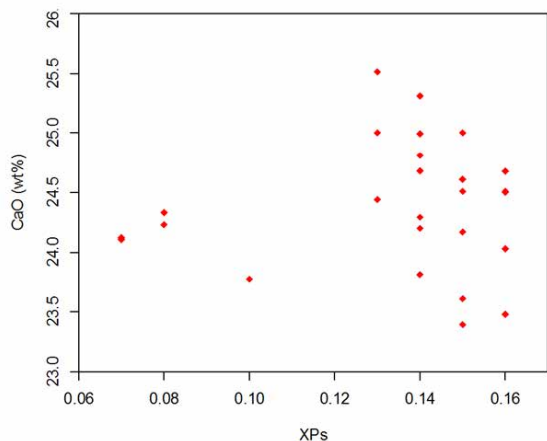


Figure 3. X Ps-CaO (wt%) relationship of epidote minerals in metabasic rocks.

Table 1. Chemical analyses of the epidote minerals, the formula is normalized on Si = 3 apfu due to high Si value ($Si > 3.05$ apfu, [18]).

Wt%	G ₃ -1-3	G ₃ -1-7	G ₃ -1-8	G ₃ -2-Z1-1	G ₃ -3-8	G ₃ -3-9	M-1-2	M-1-3	M-1-6	M-1-9	M-1-2-1	M-1-2-2	M-1-2-5
SiO ₂	39.12	39.24	39.22	39.24	39.35	39.37	38.35	38.86	38.43	39.36	38.42	38.73	37.58
TiO ₂	0.16	0.14	0.14	0.15	0.18	0.12	0.18	0.16	0.23	0.17	0.28	0.18	0.09
Al ₂ O ₃	27.25	27.49	27.54	27.24	27.10	26.97	27.84	26.57	27.93	27.46	28.04	27.69	27.68
Cr ₂ O ₃	0.04	0.11	0.11	0.05	0.00	0.02	0.08	0.22	0.08	0.05	0.17	0.20	0.02
Fe ₂ O ₃	7.23	6.68	6.68	7.43	7.64	7.75	6.66	7.89	6.32	6.84	7.06	6.77	7.61
MnO	0.07	0.09	0.09	0.14	0.12	0.14	0.07	0.01	0.03	0.08	0.09	0.11	0.14
MgO	0.00	0.00	0.00	0.00	0.00	0.00	0.11	0.10	0.17	0.12	0.11	0.01	0.12

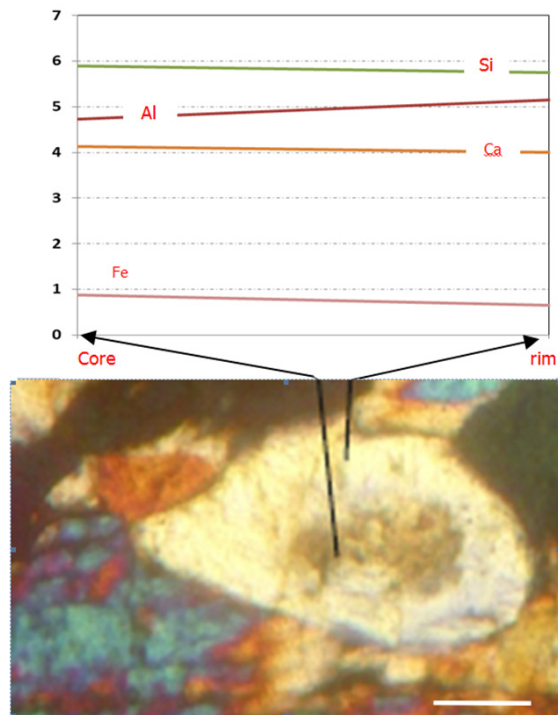


Figure 4. Chemical zoning of the epidote. Scale bars represent 0.03 mm

against 17.75%).

In thin section, the zoning is occasionally clear from the colour variation/intensity, nonetheless characteristically shows up in the interference colours, in that birefringence is a strong function of the chemical composition, especially the Fe-Al content. Single epidote grains commonly exhibits a growth zoning; the core shows relative enrichment in Fe, Si and Ca, and depletion in Al in comparing with its rim (Fig. 4). Based on the molar fractions of the end-members, it has been classified in the epidote solid solutions series as epidote and zoisite; they were calculated respectively as: $XFe^{3+} = Fe^{3+} / (Fe^{3+} + Al^{3+} - 2 + Cr^{3+})$, $XAl^{3+} = (Al^{3+} - 2) / (Fe^{3+} + Al^{3+} - 2 + Cr^{3+})$ [17]. The epidote crystals are mostly zoisite (Xcz) in composition, ranging from $Xcz = 0.46-0.72$ (Table 1), while epidote composition (Xep) also exists, with $Xep = 0.27-0.53$.

Table 1. Chemical analyses of the epidote minerals, the formula is normalized on Si = 3 apfu due to high Si value (Si > 3.05 apfu, [18]) (cont.).

Wt%	G ₃₋₁₋₃	G ₃₋₁₋₇	G ₃₋₁₋₈	G _{3-2- z1-1}	G ₃₋₃₋₈	G ₃₋₃₋₉	M-1-2	M-1-3	M-1-6	M-1-9	M-1- 2-1	M-1- 2-2	M-1- 2-5
CaO	24.23	24.11	24.12	24.33	23.39	24.03	25.00	24.50	25.51	24.20	24.29	24.68	25.00
Na ₂ O	0.01	0.00	0.00	0.02	0.00	0.04	0.07	0.02	0.01	0.11	0.02	0.00	0.04
TOTAL	98.11	97.86	97.89	98.59	97.78	98.44	98.35	98.33	98.71	98.38	98.47	98.36	98.28
<i>Based on 8 cations and 12.5 oxygens</i>													
Si	3.03	3.04	3.04	3.04	3.05	3.05	2.97	3.01	2.98	3.05	2.98	3.00	2.91
Ti	0.01	0.01	0.01	0.01	0.01	0.01	0.01	0.01	0.01	0.01	0.02	0.01	0.01
Al	2.49	2.51	2.51	2.49	2.47	2.46	2.54	2.43	2.55	2.51	2.56	2.53	2.53
Cr	0.00	0.01	0.01	0.00	0.00	0.00	0.00	0.01	0.00	0.00	0.01	0.01	0.00
Fe ₂	0.00	0.00	0.00	0.00	0.00	0.00	0.00	0.00	0.00	0.00	0.00	0.00	0.00
Fe ₃	0.21	0.19	0.19	0.22	0.45	0.45	0.39	0.46	0.37	0.40	0.41	0.39	0.44
Mn ₃₊	0.00	0.01	0.01	0.01	0.01	0.01	0.00	0.00	0.00	0.01	0.01	0.01	0.01
Mg	0.00	0.00	0.00	0.00	0.00	0.00	0.01	0.01	0.02	0.01	0.01	0.00	0.01
Ca	2.01	2.00	2.00	2.02	1.94	1.99	2.07	2.03	2.12	2.01	2.02	2.05	2.07
Sr	0.00	0.00	0.00	0.00	0.00	0.00	0.00	0.00	0.00	0.00	0.00	0.00	0.00
Na	0.00	0.00	0.00	0.00	0.00	0.01	0.01	0.00	0.00	0.02	0.00	0.00	0.01
XFe ₃₊	0.30	0.27	0.27	0.31	0.48	0.49	0.42	0.51	0.40	0.44	0.42	0.42	0.46
XAl ₃₊	0.70	0.72	0.72	0.69	0.52	0.50	0.58	0.47	0.60	0.56	0.57	0.56	0.54
XPs	0.08	0.07	0.07	0.08	0.15	0.16	0.13	0.16	0.13	0.14	0.14	0.14	0.15
Wt%	M-1- 3-1	M1- 4-a2	M1- 4-e2	M1-4- pl1-1	M1-4- pl1-2	M1-4- pl1-3	M1-4- pl1-5	M1-4- pl1-7	M1- 4-z1	M4- tüm-5	M4- tüm-6	M4- tüm2- 1	M4- tüm2- 7
SiO ₂	38.85	39.31	39.01	38.13	37.69	39.23	38.17	39.15	39.30	38.47	39.19	39.28	37.91
TiO ₂	0.19	0.22	0.05	0.20	0.20	0.20	0.16	0.16	0.15	0.31	0.17	0.25	0.15
Al ₂ O ₃	27.03	26.14	27.23	27.36	27.36	27.36	27.52	26.58	26.51	27.20	29.83	26.85	27.76
Cr ₂ O ₃	0.08	0.04	0.10	0.10	0.10	0.10	0.09	0.09	0.14	0.07	0.06	0.14	0.04
Fe ₂ O ₃	6.76	7.61	7.26	7.15	7.15	7.15	7.60	7.67	7.20	7.57	5.09	7.90	6.75
MnO	0.07	0.07	0.11	0.17	0.17	0.17	0.08	0.08	0.07	0.09	0.09	0.05	0.12
MgO	0.16	0.19	0.14	0.14	0.14	0.14	0.08	0.08	0.14	0.30	0.18	0.22	0.40
CaO	24.99	24.68	23.61	24.81	25.31	23.81	24.51	24.51	24.61	24.17	23.77	23.48	24.44
Na ₂ O	0.05	0.00	0.00	0.00	0.00	0.00	0.04	0.04	0.02	0.09	0.08	0.02	0.15
TOTAL	98.19	98.24	97.50	98.07	98.13	98.17	98.24	98.35	98.16	98.27	98.46	98.20	97.72
<i>Based on 8 cations and 12.5 oxygens</i>													
Si	3.01	3.05	3.02	2.95	2.92	3.04	2.96	3.03	3.04	2.98	3.04	3.04	2.94
Ti	0.01	0.01	0.00	0.01	0.01	0.01	0.01	0.01	0.01	0.02	0.01	0.01	0.01
Al	2.47	2.39	2.49	2.50	2.50	2.50	2.51	2.43	2.42	2.48	2.72	2.45	2.53
Cr	0.00	0.00	0.01	0.01	0.01	0.01	0.01	0.01	0.01	0.00	0.00	0.01	0.00
Fe ₂	0.00	0.00	0.00	0.00	0.00	0.00	0.00	0.00	0.00	0.00	0.00	0.00	0.00

Table 1. Chemical analyses of the epidote minerals, the formula is normalized on Si = 3 apfu due to high Si value (Si > 3.05 apfu, [18]) (cont.).

Wt%	M-1-3-1	M1-4-a2	M1-4-e2	M1-4-pl1-1	M1-4-pl1-2	M1-4-pl1-3	M1-4-pl1-5	M1-4-pl1-7	M1-4-z1	M4-tüm-5	M4-tüm-6	M4-tüm2-1	M4-tüm2-7
Fe ₃	0.39	0.44	0.42	0.42	0.42	0.42	0.44	0.45	0.42	0.44	0.30	0.46	0.39
Mn	0.00	0.00	0.01	0.01	0.01	0.01	0.00	0.00	0.00	0.01	0.01	0.00	0.01
Mg	0.02	0.02	0.02	0.02	0.02	0.02	0.01	0.01	0.02	0.03	0.02	0.03	0.05
Ca	2.07	2.05	1.96	2.06	2.10	1.98	2.03	2.03	2.04	2.01	1.97	1.95	2.03
Sr	0.00	0.00	0.00	0.00	0.00	0.00	0.00	0.00	0.00	0.00	0.00	0.00	0.00
Na	0.01	0.00	0.00	0.00	0.00	0.00	0.01	0.01	0.00	0.01	0.01	0.00	0.02
XFe ₃₊	0.45	0.53	0.46	0.45	0.45	0.45	0.46	0.51	0.49	0.48	0.29	0.50	0.42
XAl ₃₊	0.54	0.46	0.53	0.54	0.54	0.54	0.53	0.49	0.50	0.52	0.71	0.49	0.57
XPs	0.14	0.16	0.15	0.14	0.14	0.14	0.15	0.16	0.15	0.15	0.10	0.16	0.13

$$XAl_{3+} = (Al^{3+} - 2) / (Fe^{3+} + Al^{3+} - 2 + Cr^{3+})$$

$$XFe^{3+} = Fe^{3+} / (Fe^{3+} + Al^{3+} - 2 + Cr^{3+})$$

$$XPs = Fe^{3+} / (Fe^{3+} + Al^{3+})$$

DISCUSSIONS AND CONCLUSION

Pistacite [Ps: Fe³⁺/(Fe³⁺ Al)], and TiO₂ wt % contents of epidote were substantial to determine its origin. In the literature review, Ps ranges in igneous epidotes are as follows; (1) 25-29% [19], (2) 23-27% [20], (3) 19-24% [21], (4) 26-33% [22], (5) 30-70 % [23], (6) 21-26 % [8], (7) 16-29% [24]. [19] suggested that epidotes formed from alteration of plagioclase varied from Ps0 to Ps24 those formed by alteration of biotite varied from Ps36 to Ps48. In sum, Ps content range 16-70, and 0-48 % in igneous and secondary epidotes. [23] also suggest that metamorphic epidotes show pistacite molar percentage of 0 to 100 %. The samples have Ps content varies from Ps7 to Ps16, suggesting both metamorphic and secondary (plagioclase alteration) origin. Secondary epidote is usually smaller in comparing with igneous epidote, and forms as a product of alteration of plagioclase [25]. Generally, the unsaturated nature of plagioclase, with small-intermediate size is unfavour of secondary origin.

[9] suggest that igneous epidote has TiO₂ <0.2 wt%. Similarly [22] reported that igneous and secondary epidotes have TiO₂ contents <0.2 wt% and >0.6 wt (%), respectively. In metamorphic epidote, TiO₂ ranges are as follows; 0.01-0.14% in greenschist metabasite [26], 0.02-0.12 % in epidote blueschist [10], 0.08-0.64 % in garnet amphibolite [27], 0.07 to 0.22 wt% in eclogite and associated metabasite [10], and 2.06 wt% TiO₂ in epidote-glaucophane-blueschist [28]. TiO₂ contents of the samples range from 0.05 to 0.31 wt%, but mostly less than 0.2 wt%, suggesting an igneous origin of the epidotes in the samples.

[20] suggested that igneous epidote may have some textural and phase relationship as follows; (a) epidote overprinting

ehedral allanite, (b) ehedral slightly pleochroic epidote in biotite, (c) embayed hornblende by epidote, (d) wormy intergrowths with plagioclase and/or quartz, (e) epidote associated with magmatic flow banding, and (f) crystallisation of epidote in unaltered rocks. (g) Igneous epidote can also form as inclusion in primary muscovite [29], (h) inclusion in biotite and K-feldspar [30], and (i) exhibit fine scale oscillatory zoning [9]. The epidote is subhedral to ehedral (Fig. 2), and embays and truncates an optically continuous amphibole, confirming an igneous origin for epidote. [31] suggest that the amphibole in the samples may have igneous origin and crystallized under a medium pressure (≤ 7 kb) based on characteristics of their mineral chemistry. The samples is also characterised by the lack of pyroxene crystals possibly due to high content of water in the magma [32] [33]. It was experimentally shown that high H₂O contents, 5wt % at 400MPa, or 7-9 wt % at 960 MPa, may cause amphibole to be the liquidus silicate phase, and impede pyroxene crystallisation [32] [33]. Taking account the extensive crystallisation of amphibole in the samples and its intermediate crystallisation pressure, it is likely that the magma could have water contents higher than 5 wt % during initial stage of crystallization. [34] shows experimentally that Fe³⁺ content of epidote increases with fO₂, and decreasing fO₂ induce epidote more aluminous. Low pistacite content (Ps7-16) of the samples indicates low fO₂ conditions during crystallisation of the magma.

Consequently, petrographical characteristics and mineral chemistry of the epidote in metamafic rocks from metamorphic basement suggests that the epidote crystals are of igneous in origin, and likely to be crystallized from a magma with high water content (higher than 5 wt %) and low fO₂ conditions during initial stage of crystallization.

ACKNOWLEDGEMENT

The authors wish to thank Konya Technic University and Selcuk University for financial support of the project.

References

1. Haiy RJ. *Traité de Mineralogie*, (Vol. 2), 1822.
2. Chukhrov VV. *Minerals*, (VV Chukhrov Ed. Vol. 3). Moscow, Nauka, 1972.
3. Pattnaik SK. Petrology of the Bhela-Rajna alkaline complex, Nuapara District, Orissa. *Journal of the Geological Society of India* 48(1) (1996) 27-40.
4. Leterrier J. (1972). Etude petrographique et geochemique du massif granitique de Querigut (Ariege). (PhD), Universite de Nancy, France.
5. Cornelius HP. *Geologische Beobachtungen im Gebiet des Fornogletschers (Engadin)*, (Vol. = Jg. 1913, Nr. 8, S. 246-252), 1913.
6. Owen J. Significance of epidote in orbicular diorite from the Grenville Front zone, eastern Labrador. *Mineralogical Magazine* 55(379) (1991) 173-181.
7. Owen JV. Geochemistry of Orbicular Diorite from the Grenville Front Zone, Eastern Labrador. *Mineralogical Magazine* 56(385) (1992) 451-458.
8. Korinevskii VG. Magmatic epidote from gabbro. *Russian Geology and Geophysics* 49(3) (2008) 159-164.
9. Evans BW, Vance JA. Epidote Phenocrysts in Dacitic Dikes, Boulder County, Colorado. *Contributions to Mineralogy and Petrology* 96(2) (1987) 178-185.
10. Enami M, Liou JG, Mattinson CG. Epidote minerals in high P/T metamorphic terranes: Subduction zone and high- to ultrahigh-pressure metamorphism. *Epidotes* 56 (2004) 347-398.
11. Nicollet C, Leyreloup A, Dupuy C. Chapter 14 - Petrogenesis of High Pressure Trondhjemitic Layers in Eclogites and Amphibolites from Southern Massif Central, France. In F Barker (Ed.), *Developments in Petrology* (Vol. 6, pp. 435-463): Elsevier, 1979.
12. Franz G, Smelik EA. Zoisite-clinozoisite bearing pegmatites and their importance for decompressional melting in eclogites. *European Journal of Mineralogy* 7(6) (1995) 1421-1436.
13. Özcan A, Göncüoğlu MC, Turhan N, Şentürk K, Uysal Ş, Işık A. Konya-Kadınhanı-İlgin dolayının temel jeolojisi (in Turkish) (1990). MTA Genel Müdürlüğü Jeoloji Etütleri Dairesi.
14. Kaya RM. (2017). Karadığın (Meram, Konya) Yöresi'ndeki Hatip Ofiyolitli Karışığında Yer Alan Metamagmatiklerin Mineralojik Özellikleri. (MSc), Selcuk Uni., Konya.
15. Dasci HT, Parlak O, Nurlu N, Billor Z. Geochemical characteristics and age of metamorphic sole rocks within a Neotethyan ophiolitic melange from Konya region (central southern Turkey). *Geodinamica Acta* 27(4) (2015) 223-243.
16. Okay A, Tüysüz O. Tethyan sutures of northern Turkey. In: Durand B, Jolivet L, Horvárt, Séranne M (eds) *The mediterranean basins: tertiary extension within the alpine Orogen*. Geological Society London Special Publications 156 (1999) 475-515.
17. Franz G, Liebscher A. Physical and chemical properties of the epidote minerals - An introduction. *Epidotes* 56 (2004) 1-+.
18. Armbruster T, Bonazzi P, Akasaka M, et al. Recommended nomenclature of epidote-group minerals, (Vol. 18), 2006.
19. Tulloch AJ. Secondary Ca-Al silicates as low-grade alteration products of granitoid biotite. *Contributions to Mineralogy and Petrology* 69(2) (1979) 105-117.
20. Zen EA, Hammarstrom JM. Magmatic epidote and its petrologic significance. *Geology* 12(9) (1984) 515-518.
21. Dawes RL, Evans BW. Mineralogy and Geothermobarometry of Magmatic Epidote-Bearing Dikes, Front Range, Colorado. *Geological Society of America Bulletin* 103(8) (1991) 1017-1031.
22. de Oliveira MA, Dall'Agnol R, Scaillet B. Petrological Constraints on Crystallization Conditions of Mesoproterozoic Sanukitoid Rocks, Southeastern Amazonian Craton, Brazil. *Journal of Petrology* 51(10) (2010) 2121-2148.
23. Schmidt MW, Poli S. Magmatic epidote. *Epidotes* 56 (2004) 399-430.
24. Tchameni R, Sun F, Dawai D, et al. Zircon dating and mineralogy of the Mokong Pan-African magmatic epidote-bearing granite (North Cameroon). *International Journal of Earth Sciences* 105(6) (2016) 1811-1830.
25. Ismail A, Ghani AA. Magmatic epidote: probable absence and implication to the geobarometry of the granitic rocks from Peninsular Malaysia. *Bulletin of the Geological Society of Malaysia* 45 (2002) 231-234.
26. Lugovic B, Segvic B, Altherr R. Petrology and tectonic significance of greenschists from the Medvednica Mts. (Sava Unit, NW Croatia). *Ofioliti* 31(1) (2006) 39-50.
27. Qian JH, Wei CJ. P-T-t evolution of garnet amphibolites in the Wutai-Hengshan area, North China Craton: insights from phase equilibria and geochronology. *Journal of Metamorphic Geology* 34(5) (2016) 423-446.
28. Howie RA, Walsh JN. The geochemistry and mineralogy of an epidote-glaucophanite from Hacava, Spišskogemerské rudohorie Mountains, West Carpathians, Czechoslovakia. *Geol. Práce* 78 (1982) 59-64.
29. Sial AN, Toselli A, Saavedra J, Ferreira VP, Rossi de Toselli JN. (1995). Magmatic epidote bearing granitoids from NW Argentina and NE Brazil. Paper presented at the Third Hutton Symposium. The Origin of granites and related rocks, Univ. of Maryland.
30. Sial AN, Toselli AJ, Saavedra J, Parada MA, Ferreira VP. Emplacement, petrological and magnetic susceptibility characteristics of diverse magmatic epidote-bearing granitoid rocks in Brazil, Argentina and Chile. *Lithos* 46(3) (1999) 367-392.
31. Koçak K, Kaya RM, Döyem A, Söğüt AR, Zedef V. Mineralogical and chemical characteristics of the amphibole minerals from the metamorphic sole rocks of the Late Cretaceous-aged Hatip ophiolitic melange in the Konya area (Central Southern Turkey). *Selcuk Univ. J. Eng. Sci. Tech.* 6(3) (2018) 519-528.
32. Naney MT. Phase-Equilibria of Rock-Forming Ferromagnesian Silicates in Granitic Systems. *American Journal of Science* 283(10) (1983) 993-1033.
33. Prouteau G, Scaillet B. Experimental constraints on the origin of the 1991 Pinatubo dacite. *Journal of Petrology* 44(12) (2003) 2203-2241.
34. Liou JG. Synthesis and Stability Relations of Epidote, Ca₂Al₂FeSi₃O₁₂ (OH). *Journal of Petrology* 14(3) (1973) 381-413.

Dietary Exposure Assessment of Aflatoxin From Dried Figs in Turkey

Hatice Imge Oktay Basegmez 

Adana Alparslan Türkeş Science and Technology University, Department of Bioengineering, Adana, Turkey

ABSTRACT

Aflatoxins are fungi's secondary toxigenic metabolites and known as potent hepatocarcinogen for humans. The purpose of the present study is to assess health risk for Turkish adult population posing by dried fig consumption due to the aflatoxin contamination. In order to make this evaluation total of 23.547 aflatoxin monitoring data of dried figs from the Turkish Ministry of Food, Agriculture and Livestock between the crop years of 2011/2012-2015/2016 in Turkey were used. Intakes were estimated using consumption data and aflatoxin concentrations and expressed using the average Turkish adults' body weight (72.8 kg). Estimated daily exposure was found 0.005 ng/kg bw/day for aflatoxin B₁, 0.009 for total aflatoxins in a worst case scenario. The calculated margin of exposure (MOE) was higher than the 10.000. Cancer risk in Turkish adult population observed in the range between 0.00017 to 0.00030 cancers per 100,000 people per year. Calculated MOE and population risk according to estimated daily intake revealed that Turkish adult population are not under the toxicological risk through dried fig consumption.

Keywords:

Aflatoxin, Dietary Intake, Risk Assessment, Exposure Analysis, Dried Figs, Turkey

Article History:

Received: 2019/02/06

Accepted: 2019/09/19

Online: 2019/09/30

Correspondence to: Hatice Imge Oktay Basegmez,

E-mail: ibasegmez@atu.edu.tr;

Phone: +90 322 455 0000;

Fax: +90 322 455 0039.

INTRODUCTION

Based on 2017/2018 crop production estimates, dried figs produced mainly by Turkey (58% market share), Iran (13%), USA (7%), Afghanistan (7%) and Greece (6%) for domestic consumption and export trade. Turkey, as the leading country of fig production, exports approximately 90% of their dried fig production and about 75% of the export were carried out with European Union member states [1].

Dried figs are susceptible to aflatoxin (AF) contamination and natural occurrence of AF can be at high levels. Fruit structure, harvesting, drying and storage can affect the occurrence of AF in dried figs as well as its high sugar content. Moreover, due to its fleshy skin -which does not provide any protection- AF contamination can occur easily in it. It is important to note that the natural occurrence of AF in a single fig fruit can reach very high levels, such as 4000 µg/kg, the presence of AF in dried figs is considered a major threat to human health [2].

Fungi belongs to *Aspergillus* genus are the main

producers of AFs. *Aspergillus flavus* is the most common toxigenic species, but different strains produce different amounts of AFs and some produce none. Fungi produce nearly 20 secondary metabolites, among them, food samples contains only four major aflatoxins B₁, B₂, G₁ and G₂ naturally [3]. Aflatoxin B₁ (AFB₁) was found to be a potent hepatocarcinogen according to human, animal and cell and tissue culture studies and International Agency of Research on Cancer was classified both AFB₁ and total AFs (AFTOT) carcinogenic to humans (Group I) [4].

The FAO/WHO Joint Expert Committee on Food Additives (JECFA) in 1987, 1997, 2007 performed an evaluation of this toxin. Due to the genotoxic and carcinogenic properties of aflatoxins, no observed adverse effect level (NOAEL) and a tolerable daily intake (TDI) value have not been specified [5, 6]. Instead, according to epidemiological and toxicological studies, calculated potency estimates for human liver cancer originated AFs exposure [7]. Carcinogenicity of AFs varies in humans having chronic hepatitis B virus infection.

Major toxicological impact of AFs is being responsible for 4.6%-28.2% liver cancer cases throughout the world when hepatitis virus infection positive and negative individuals considered [8]. Similar with JECFA, The European Union Scientific Committee for Food (SCF) also concluded that even very low levels of exposure to AFs (<1 ng kg⁻¹ bw day⁻¹), could promote the liver cancer risk [9]. Therefore ALARA principle is recommended, which means AF contamination levels should be reduced to being as low as reasonably achievable [5].

Regulatory limits for AFs and other mycotoxins expressed for food and feed products in more than 100 countries and AF limits vary widely among countries. The United States Food and Drug Administration (FDA) has accepted a maximum guidance limit for AF in foods at 20 µg/kg AFTOT [10]. Because of high toxicity and carcinogenic properties, legal tolerance levels in the EU and in Turkish legislations are low for AF in dried fruits that are intended for human consumption (AFB₁:8 µg/kg; AFTOT :10 µg/kg). The Codex Alimentarius Commission has adopted on July 2nd 2012 new maximum limits for AFs in ready to eat dried figs (AFB₁: 6 µg/kg; AFTOT :10 µg/kg) [11].

As hazard to public health from AFs are well known, mold growth and mycotoxin production are common concerns for all countries that produce and consume figs. The fig industry in Turkey working together with government agencies have been pro-active in developing programs to improve prevention, detection and analytical methods to minimize AF contamination in dried figs. Estimation of dietary intake of toxins is important for risk analysis. It is also essential to make the necessary regulations for the protection of public health. Risk assessment can be used to quantify the magnitude of exposure, or probability of harmful effect on individuals/populations from chemicals such as mycotoxins. Risk assessments includes four step, which; hazard identification, dose-response analysis, exposure assessment and risk characterization. Risk assessments of AFs have been performed in Africa, China, Taiwan [12], Vietnam [13], Lebanon [14], and public health risk were evaluated calculating the margin of exposure (MOE) values and/or population risk related with consumption of various types of foods. Because Turkey is the leading country for dried fig production, having a risk assessment evaluation of AFs is important.

This study aimed to assess health risks through dietary exposures to AFs with consumption of dried figs among Turkish adult population. Dietary exposure risk assessment was conducted through MOE value and cancer potency factor calculation using the estimated daily intake (EDI).

MATERIAL AND METHODS

Aflatoxin Contamination Data

Concentration data were collected and combined from the Turkish Ministry of Food, Agriculture and Livestock between crop years of 2011/2012 and 2015/2016. Results on the concentration of AFB₁ and AFTOT in dried figs was available for a total of 23.547 samples from the mycotoxin monitoring program. Samples were analysed for the presence of AFs with a validated method using an immunoaffinity column clean-up and High Pressure Liquid Chromatography system equipped with fluorescence detection [15] in accredited national control laboratories. Results are expressed in nanograms (ng) per gram weight.

Estimation of Dried Fig Consumption

Although it is very important to have a detailed consumption survey in order to make accurate AF dietary exposure, Turkey does not have comprehensive national consumption survey, yet. For the present study in order to make the evaluation of AF exposure through dried fig consumption, Turkey's estimated dried figs consumption per capita is taken as 0.5 grams per day [16].

Calculation of Estimated Dietary Exposure to Afs

Handling of censored data (results below limit of detection) was conducted according to EFSA (2010) for calculation purposes. Prevalence of censored data was between 86.5 and 90.9% during the five year of harvest seasons. The average toxin concentrations were used for the daily intake calculations. During the of average toxin level calculation, not detected samples were considered as 0 for lower bound (LB) estimates and were considered as the limit of detection (LOD) for upper bound (UB) estimates because of censored data percentage was higher than 60% [17]. For the exposure estimates, the average body weight for Turkish adults (72.8 kg) were used according to the National Institute of Statistics [16]. Intake values are expressed in ng per kg body weight per day. The estimated daily intake (EDI) of AFs was calculated as follows:

$$EDI \text{ (ng/kg b.w/day)} = \left[\frac{\text{toxin (ng/g)} \times \text{consumption (g/day)}}{\text{average b.w. (kg)}} \right] \quad (1)$$

Risk Assessment

There is no threshold value specified for AFs exposures because for the chemicals that cause cancer completely safe level cannot be established. Especially chemicals directly or indirectly act on DNA such as AFB₁ which could start changes leading to cancer. Therefore, the calculated EDI cannot be directly compared with threshold level for AFs.

The JECFA set forth a risk dose of 0.013105 (ng/kg bw/day) for adults in European Countries according to human epidemiological data. Meaning of risk dose is 0.013 increase in the incidence of cancer per year in the general population of 100,000 people exposure of per ng AFs/kg bw/day [6].

Hepatitis also increase the risk of liver cancer in parallel with AFs exposure. Aflatoxin exposure in patients with chronic hepatitis is known to significantly increase the risk of liver cancer. The JECFA also calculated the risk of liver cancer 0.3 and 0.01 cancer/year for 100,000 people/ng AF/kg bw/day for people with hepatitis B surface antigen negative (HBsAg-) and positive (HBsAg+) people, respectively [6].

If the calculated MOE is below 10.000 which is equivalent to 170 ng/kg bw/day AFs, there is public health risk due to the AFs contaminated food consumption [5].

Evaluation of MOE and population health risk which were calculated based on estimated daily intake level was conducted. The risk of liver cancer for the Turkish population was evaluated according to the EDI results and average potency factor calculated using the chronic hepatitis prevalence. WHO classified Turkey as intermediate in terms of endemicity for hepatitis B (2-8%). Prevalence of chronic hepatitis B infection was reported between 4.0% and 5.0%. Similar with these data, Mehmet et al., [18] reported that the prevalence of HBsAg(+) as 8.2% and 6.2% in the rural and urban areas of Southeastern of Turkey, respectively. In order to point out worst case scenario, prevalence rate of 8% is used for calculation of average potency. Average potency and population risk were calculated using the formulas below.

$$\begin{aligned} \text{Population risk} &= \text{Exposure} \times \text{average potency} \\ \text{Average potency} &= 0.3 \times 0.08 + 0.01 \times 0.92 = 0.033 \end{aligned} \quad (2)$$

RESULTS AND DISCUSSION

Limit of detection (LOD) and limit of quantification (LOQ) for AFB₁ and AFTOT was 0.067, 0.2 and 0.17, 0.5 ng/g, respectively. Table 1 shows concentration data of AF contaminated dried figs in Turkey from 2011-2012 to 2015-2016 harvest seasons. The concentrations of AFB₁ and AFTOT varied from 0.20 to 431.43 ng/g and from 0.51 to 477.90 ng/g, respectively.

There are several studies available in literature with regard the natural occurrence of AFs in dried figs. It can be seen from the Table 2, AF contamination is a problem mainly in Turkey because it is the major producer. Aflatoxin contamination data from the Turkey in accordance with our contamination results express that AF contamination in dried figs can be menace Turkish population and risk assessment is a vital necessity.

Table 1. Summary of annual AF contamination (ng/g) of dried figs.

Year	2011-2012	2012-2013	2013-2014	2014-2015	2015-2016
No. of Samples	4116	4644	5041	4677	5069
No. of Positive Samples (%)	403 (9.79%)	627 (13.50%)	550 (10.91%)	426 (9.11%)	504 (9.94%)
Mean AFB ₁ of positive samples (ng/g)	5.94	5.39	6.56	4.84	5.08
Mean AFTOT of positive samples (ng/g)	10.93	8.08	9.79	8.32	6.79
Mean AFB ₁ - LB* (ng/g)	0.58	0.73	0.72	0.44	0.51
Mean AFB ₁ - UB* (ng/g)	0.64	0.79	0.78	0.50	0.57
Mean AFTOT - LB (ng/g)	1.07	1.09	1.07	0.76	0.68
Mean AFTOT - UB (ng/g)	1.22	1.24	1.22	0.91	0.83
AFB ₁ Range (ng/g)	0.2-183.00	0.2-254.40	0.2-431.43	0.2-88.04	0.2-381.30
AFTOT Range (ng/g)	0.51-374.10	0.51-415.19	0.50-477.90	0.51-264.00	0.51-403.90

* LB (lower bound): results under LOD reported as 0, UB (upper bound): results under LOD reported as LOD.

Table 2. Summary of natural occurrence of AFTOTs in dried figs in literature.

Positive sample/ Total Sample (%)	Range of AFTOTs (ng/g)	Country	Reference
26/33	0.22-83.4	Algeria	[19]
4/14	LOD*-11.10	Pakistan	[20]
13/22	0.3-7.0	Iran	[21]
16/130	0.1-28.2	Turkey	[22]
219/104 (47.5%) (for export)	ND*-267.48	Turkey	[23]
2461/580 (23.6%) (from local store)	ND-278.04	Turkey	[23]
11/115	0.1-763.2	Turkey	[24]
313/2643	0.2-162.76	Turkey	[25]
1575/4917	0.2-259.46	Turkey	[25]

*LOD: Limit of Detection, ND: Not Determined

In order to reveal the worst scenario, the estimated daily intake was calculated by using the data from harvest year with the highest contamination of AF. The highest daily exposure may occurred during 2012/2013 harvest season due to the highest AF contamination (Table 1). Based on highest AF levels in the analyzed dried fig samples and using an average body weight of 72.8 kg, estimated daily intake was determined 0.005 (LB), 0.005 (UB) ng/g bw/day for AFB₁ and 0.008 (LB), 0.009 (UB) ng/g bw/day for AFTOT.

Table 3. AF dietary exposure assessment* and risk characterization.

	Mean Exposure (ng/kg bw/day)	MOE ^b	Risk ^c
AFB ₁	(LB) ^a 0.005	34.000	0.00017
	(UB) ^a 0.005	34.000	0.00017
AFTOT	(LB) 0.008	21.250	0.00027
	(UB) 0.009	18.889	0.00030

* Calculated using 2012/2013 harvest season data

^b MOE=BMDL₁₀/Dietary exposure, BMDL₁₀= 170 ng/kg bw/day

^c Risk, liver cancer cases/100.000 population/year

Dietary intake of AFs through dried fig consumption in Turkey does not pose a potential public health risk with regard to MOE, because calculated MOE was higher than 10.000. Based on the average exposure of AFB₁ and AFTOT associated with an average risk of excessive liver cancer of 0.0002-0.0003 cases / 100,000 individual for a year. It can be seen from the risk factor AF exposure through dried figs is not a problem alone. But it should be remember that people are exposed to AF contamination from various types of food in which the most important one is cereals for Turkish consumers. Table 4 summarises estimates of dietary aflatoxin exposure from other countries.

Table 4. Summary of AF exposure assessment studies in literature.

Food Product	Mean intake		Potential Risk	Country	Reference
	of AFB ₁ (ng/kg bw/ day)	of AFTOT (ng/kg bw/day)			
Hazelnut	0.014 (LB) 0.016 (UB)	0.018 (LB) 0.023 (UB)	-	Turkey	[22]
Dried fig	0.003 (LB) 0.003 (UB)	0.004 (LB) 0.005 (UB)	-	Turkey	[22]
Dried fig (from local store)	-	1.27	-	Turkey	[23]
Dried fig (for export)	-	0.2	-	Turkey	[23]
Various types of foods (cereals, pizza, pulses, nuts etc.)	0.63 (LB) 0.66 (UB)	-	0.0527- 0.0545 cases / 100,000 persons / year	Lebanon	[14]
Mullberry, Date, Fig, Apricot	0.04 0.12 0.04 0.06	-	4250 1417 4250 2833 (MOE) 1.2 0.3	Iran	[21]
Rice and maize	17.7 4.0	-	Cancers / 100,000 pop. / year 0.0007- 0.2713 cancers / 100,000 pop. / year	Vietnam	[13]
Peanut and peanut products	-	0.03 (UB)	0.2713 cancers / 100,000 pop. / year	Taiwan	[12]
Muthokoi, maize kernel, maize meal	-	27 292 59	-	Kenya	[26]

The average exposure estimates to AFB₁ and AFTOT as revealed in this study were similar with those reported in Kabak [22] and much lower than estimates from other countries. These differences are appropriate because the methods and models used to evaluate dietary exposure, the LOD/LOQ of the analytical technique, handling of the censored data may differ. Also it must be noted that risk assessment from single type of food can be a limitation because AF effect should be evaluated cumulative.

All calculations in this publication are based on the assumption that the entire population consumes dried figs. On the other hand, in the Turkey nutrition and health research 2010 conducted by Ministry of Health, it is expres-

sed that 60.5 % of individuals of Turkish population stated that they do not consume dried fruits daily [27]. While the toxicological risk assessment is carried out, it is not taken into consideration how much the population consumes in the calculations. In this publication, the worst case scenario was tried to be presented.

CONCLUSION

Although AFs are present in dried figs consumed by Turkish populations, there is no toxicological risk for consumers in Turkey. Estimates of dietary AF exposure are consistent with estimates in other developed countries. However it must be noted that AF exposure may come from consumption of various types of foods. That is why exposure estimation should be conducted through total diet study which will provide cumulative exposure assessments. In order to provide a precise risk assessment, especially consumption data and exposure data are required. Unfortunately national food consumption data which includes dried figs are not available in Turkey, yet. There is an urgent need for comprehensive national food consumption survey for further studies in order to make a more precise health risk estimation for Turkish population arising from the exposure of AFs.

ACKNOWLEDGEMENTS

The authors wish to thank The Turkish Ministry of Food, Agriculture and Livestock for providing the AFs contamination data.

References

1. INC, International Nut and Dried Fruit Council. Nuts and Dried Fruits Statistical yearbook 2017/2018 (2017). https://www.nutfruit.org/files/tech/1524481168_INC_Statistical_Yearbook_2017-2018.pdf Access date 24.07.2018
2. Scott, PM, Trucksess, MW. Prevention of mycotoxins in dried fruit, other fruit products, and botanicals, in: Appell, M, Kendra, D F, Trucksess, MW (Eds.). Mycotoxin prevention and control in agriculture. ACS Symposium Series, Washington DC. 1031 pp. 17-35, 2009.
3. Richard, JL. Some major mycotoxins and their mycotoxicoses—An overview. International J Food Microbiol 119 (1-2) (2007) 3-10.
4. IARC, International Agency for Research on Cancer. Some naturally occurring substances: Food items and constituents, heterocyclic aromatic amines and mycotoxins. IARC monographs on the evaluation of carcinogenic risks of chemicals to humans vol 56 Lyon, France, 1993 <https://monographs.iarc.fr/wp-content/uploads/2018/06/mono56.pdf> Access date 24.07.2018
5. EFSA (European Food Safety Authority). Opinion of the Scientific Panel on Contaminants in the Food chain on a request from the European Commission related to the potential increase of consumer health risk by a possible

- of the existing maximum levels for aflatoxins in almonds, hazelnuts and pistachios and derived products. The EFSA Journal 446 (2007) 1–127.
6. JECFA. Evaluations of Certain Food Additives and Contaminants. WHO Food additives Series, vol. 40. (1998) IPCS, WHO, Geneva, Switzerland
 7. JECFA. Evaluation of certain food additives and contaminants. Forty-ninth Report. Technical Report Series No. 884. Geneva: WHO. (1999) pp 69–77.
 8. Liu Y, Wu F. Global burden of aflatoxin-induced hepatocellular carcinoma: A risk assessment. *Environmental Health Perspective* 118 (6) (2010) 818–824.
 9. Scientific Committee for Food (SCF). European Commission DG XXIV Unit B3. Thirty-fifth Report. Opinion on aflatoxins B1, B2, G1, G2, M1 and patulin. Expressed on 23 September 1994.
 10. U.S. Food and Drug Administration (FDA). Guidance for Industry: action levels for poisonous or deleterious substances in human food and animal feed. (2000) Available at: <https://www.fda.gov/Food/GuidanceRegulation/GuidanceDocumentsRegulatoryInformation/ChemicalContaminantsMetalsNaturalToxinsPesticides/ucm077969.htm#afla> Access: 14/11/18
 11. Codex Alimentarius Commission (CAC). Report of the sixth session of the Codex Committee on Contaminants in Foods, 35th session. July 2–7, 2012. (2012) FAO, Rome, Italy. Available at: http://www.fao.org/tempref/codex/Reports/Reports_2012/REP12_CFe.pdf Access Date 14/11/2018
 12. Wang X, Lien K, Ling M. Probabilistic health risk assessment for dietary exposure to aflatoxin in peanut and peanut products in Taiwan. *Food Control* 91 (2018) 372–380
 13. Huong BTM, Tuyen LD, Do TT, Madsen H, Brimer L, Dalsgaard A. Aflatoxins and fumonisins in rice and maize staple cereals in Northern Vietnam and dietary exposure in different ethnic groups. *Food Control* 70 (2016) 191–200.
 14. Raad F, Nasreddine L, Hilan C, Bartosik M, Parent–Massin D. Dietary exposure to aflatoxins, ochratoxin A and deoxynivalenol from a total diet study in an adult urban Lebanese population. *Food and Chemical Toxicology* 73 (2014) 35–43.
 15. AOAC Official Method 999.07. Aflatoxins and total aflatoxins in peanut butter, pistachio paste, fig paste and paprika powder. Immunoaffinity column–liquid chromatography with post–column derivatization. *Journal of AOAC International* 83 (2000) 320.
 16. TÜİK, National Institute of Statistics of Turkey (2016) www.tuik.gov.tr Access Date 14/11/2018
 17. EFSA. Management of left–censored data in dietary exposure assessment of chemical substances. *European Food Safety Authority Journal* 8 (2010) 1557.
 18. Mehmet D, Meliksah E, Serif Y, Gunay S, Tuncer O, Zeynep S. Prevalence of Hepatitis B Infection in the Southeastern Region of Turkey: Comparison of Risk factors for HBV Infection in Rural and Urban Areas. *Japanese Journal of Infectious Diseases*, 58 (2005) 15–19
 19. Mimoune NA, Arroyo–Manzares N, Gamiz–Gracia L, Garcia–Campana AM, Bouti K, Sabaou N, Riba A. Aspergillus section Flavi and aflatoxins in dried figs and nuts in Algeria. *Food Additives and Contaminants B* 11 (2) (2018) 119–125
 20. Iqbal SZ, Mehmood Z, Asi MR, Shahid M, Sehar M, Malik N. Cooccurrence of aflatoxins and ochratoxin A in nuts, dry fruits, and nuty products. *Journal of Food Safety* 38 (4) (2018) 1–7
 21. Heshmati A, Zohrevand T, Khaneghah AM, Nejad ASM, Sant’Ana AS. Co–occurrence of aflatoxins and ochratoxin A in dried fruits in Iran: Dietary exposure risk assessment. *Food and Chemical Toxicology* 106 (2017) 202–208
 22. Kabak B. Aflatoxins in hazelnuts and dried figs: Occurrence and exposure assessment. *Food Chemistry* 211 (2016) 8–16.
 23. Bircan C, Koç M. Aflatoxins in Dried Figs in Turkey: A Comparative Survey on the Exported and Locally Consumed Dried Figs for Assessment of Exposure. *Journal of Agricultural Science and Technology* 14 (2012) 1265–1274.
 24. Heperkan D, Karbancioglu Güler F, Oktay HI. Mycoflora and natural occurrence of aflatoxin, cyclopiazonic acid, fumonisin and ochratoxin A in dried figs. *Food Additives and Contaminants A* 29 (2)(2012) 277–286.
 25. Bircan C, Barringer SA, Ulken U, Pehlivan R. Aflatoxin levels in dried figs, nuts and paprika for export from Turkey. *International Journal of Food Science and Technology* 43 (2008) 1492–1498
 26. Kilonzo RM, Imungi JK, Muiro WM, Lamuka PO, Kamau Njage PM. Household dietary exposure to aflatoxins from maize and maize products in Kenya. *Food Additives and Contaminants A* 31 (2014) 2055–2062.
 27. Türkiye Cumhuriyeti Sağlık Bakanlığı Sağlık Araştırmaları Genel Müdürlüğü, Türkiye beslenme ve sağlık araştırmaları 2010, Beslenme durumu ve alışkanlıklarının değerlendirilmesi sonuç raporu (2014). Hacettepe Üniversitesi Beslenme ve Diyetetik Bölümü. Available at: https://www.tuseb.gov.tr/enstitu/tacese/yuklemeler/ekitap/Beslenme/tbsa_beslenme_arastirmasi_sonuc_raporu.pdf Access Date 30/07/2019

Implementation and Quality Assessment of a User-Centric Adaptation System for DASH

Nukhet Ozbek, Atilla Aricioglu

Ege University, Department of Electrical and Electronics Engineering, Izmir, Turkey

ABSTRACT

In recent years, dynamic adaptive streaming over HTTP (DASH) has been widely used in order to let the viewer have an uninterrupted streaming and therefore higher quality-of-experience (QoE). The technique basically relies on dynamic rate adaptation by downloading the video at lower qualities according to various network conditions. However, many issues are open related to client-side rate adaptation. For example, current DASH systems do not yet let the viewer decide which aspect of quality of the video should be reduced first and which aspect of quality of the video should be stable. This paper presents a novel adaptation system for DASH which is designed to search whether a higher QoE might be achieved if the adaptation method could be user-centric. During subjective quality assessment, it has been observed that all the participants have had a higher QoE compared to regular DASH system when they were given a chance to decide the way of adaptation.

Keywords:

Adaptive streaming; MPEG-DASH; User-centric; SSCQE; QoE.

Article History:

Received: 2019/02/24

Accepted: 2019/09/24

Online: 2019/09/30

Correspondence to: Nukhet Ozbek,
Ege University, Electrical and Electronics
Engineering, Izmir, TURKEY
E-Mail: nukhet.ozbek@ege.edu.tr
Phone: +90 232 311 16 65
Fax: +90 232 311 18 17

INTRODUCTION

Significant and fast developments in network services and smart mobile devices over the last decade have led to large growth and progress in media streaming. Eventually, old applications running on UDP and using the RTP/RTSP protocols have been replaced by new applications that use the HTTP protocol running on TCP. VoD and IPTV companies such as Apple, Adobe, Youtube have developed and used HLS (HTTP Live Streaming) [1], MSS (Silverlight Smooth Streaming) [2], HDS (HTTP Dynamic Streaming) [3] and DASH (Dynamic Adaptive Streaming over HTTP) [4], which are all HTTP based adaptation protocols. The DASH standard was introduced by MPEG to make efficient video streaming over the Internet [5]. This standard is based on the same video or audio content being encoded at different bit rates and kept on the server as small HTTP file segments and the adaptation is made on the client side by considering network conditions and buffer status. To play the content, the DASH client first obtains the manifesto file. By parsing the file, the DASH client learns about the segment duration, media-content availability, media types, resolutions, minimum and maximum bandwidths, and other content characteristics. Using this information, the DASH client selects the appropriate encoded alternative, and starts streaming

the content by fetching the segments via HTTP GET requests. After appropriate buffering to allow for network throughput variations, the client continues fetching the subsequent segments, and monitors the network bandwidth fluctuations. Depending on its measurements, the client decides how to adapt to the available bandwidth by fetching segments of different alternatives (with lower or higher bitrates) to maintain an adequate buffer.

On the other hand, the main goal of modern video streaming services is to find out how to transfer content over the network for the best Quality-of-Experience (QoE). The constant bit rate coding in the DASH system affects QoE in different ways: First, encoding different video content at the same bit rate results in different QoE. Second, the effect of different bitrate allocation options on QoE. Currently available systems use DASH, but do not leave the user with the choice of which features of the video will change when the available bandwidth changes. In this study, a user-centric adaptation system is proposed which allows the user to decrease quality depending on the QoE preferences. Before the streaming begins, the user is asked to select the QoE preferences by voting which feature is to be waived in the first place as a bitrate drop during the flow. In other

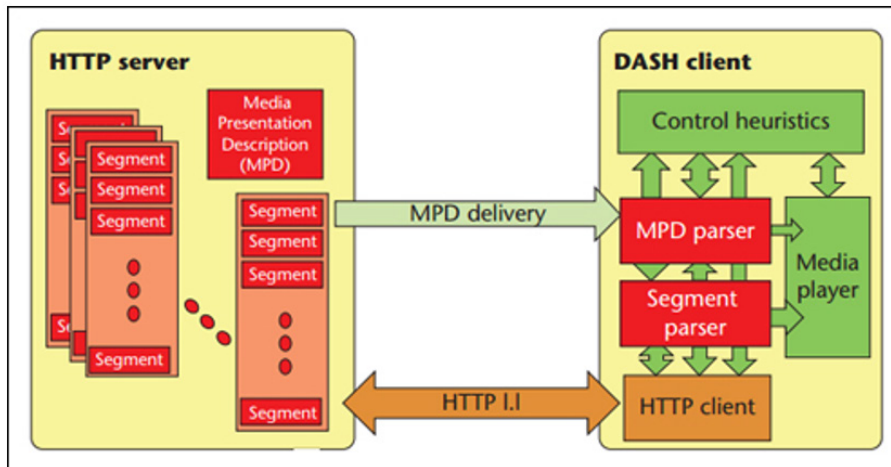


Figure 1. MPEG-DASH system [5].

words, the questions about which features will be more variable, and which features will remain unchanged as much as possible are asked to improve the QoE.

In the literature, a few studies have been suggested to develop adaptation based on user-perceived quality rather than the best media bitrate and bandwidth compliance. In [6], a segment selection algorithm was developed in which users could opt for a smaller amount of data to the player's buffer for a smoother streaming experience compromising the image quality or an image quality with better stability. In [7], a method for streaming over mobile networks is proposed to provide users with a more efficient flow by grouping and multicasting them according to the relevant video version and the base station to which the user is connected. In another study, user-centric functions have been developed to determine the effects of initial delay, freezing and image quality changes on the users QoE in the sight of subjective test results [8]. In a DASH system using scalable video encoding, it has been demonstrated that by using different image quality options, the initial waiting time is reduced, but these quality changes and low quality images reduced the user QoE [9]. In a DASH system developed for mobile devices [10], it has been suggested to collect data such as user presence, proximity to the screen and motion, screen brightness, and ambient lighting with sensors on the mobile device and to use them for better QoE. Although it is agreed that the adaptation algorithms must be designed considering not only available network resources but also the user's needs, the user has not probed yet for preferences about adaptation and quality switches.

MATERIAL AND METHODS

The working technique of MPEG-DASH is shown in Fig. 1. In the MPEG-DASH technique, the media content exists on an HTTP server in two parts. The video or

audio content is encoded at different bit rates and divided into one or multiple consecutive media segments. A manifesto containing information on the properties and locations of the segments as URL addresses, the XML file named MPD (Media Presentation Description), is kept on the server with these segments. Each segment has an addressable location on a server that can be downloaded using HTTP GET or HTTP GET with byte ranges. When the first connection is established, the client can access all the information to be tracked by fetching and parsing the MPD file. Then, on the client side, the video segment of the bit rate appropriate to the TCP throughput is requested from the server, monitoring the status of the connection, repeatedly. When the connection speed changes, switching between different bit rates allows the video to be watched without interruption. In case of bandwidth changes, it is decided by the control heuristics module that the segment file which is suitable for the calculated bit rate for the next segment/s will be requested; the requested segments are transmitted simultaneously from the HTTP server to the segment parser module in the DASH client.

The DASH technique aims to adapt to the changes of the network by changing the bitrate of the video and audio, namely switching the quality factors such as SNR (Signal-to-Noise Ratio), FPS (Frame-per-Second), and so on. Which feature of the media, (such as resolution, fps, audio bitrate etc.), will be encoded in which bitrate must be predetermined. The video and audio content is encoded to fulfill the fixed bit rate as the planned/manifested values and divided into segments of equal length in time.

We propose a novel system that allows the user to determine the DASH adaptation method. The web pages shown in Figs 2 and 3 are presented to the user as the option of selecting and determining the priority order. At the



Figure 2. Web page for the first stage of priority determination.

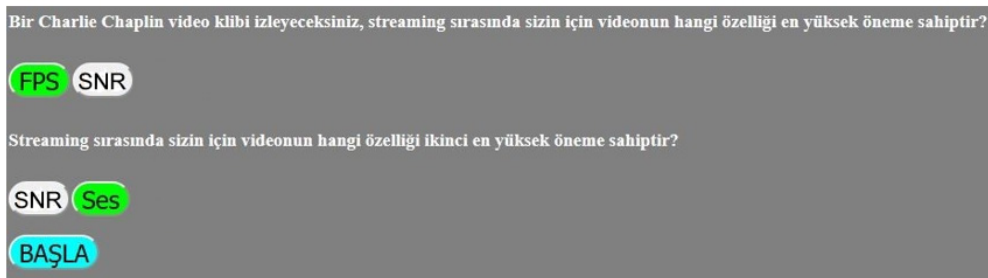


Figure 3. Web page for the second stage of priority determination after selecting FPS at the first stage.

first page the user is asked to prefer between SNR and FPS quality of the video. At the second page the user is asked for to prefer between audio quality and unselected video quality. Thus, the user determines which aspect of quality of the video should be reduced first and which aspect of quality of the video should be stable. Table 1 shows four different adaptation methods and the corresponding quality priority orders.

To implement user-centric adaptation system for DASH, The Bitmovin Adaptive Streaming HTML5 Player is used, which supports MPEG-DASH and is free for open-source and commercial purposes [11]. Four different pages are created with embedding DASH.js to use related source videos and MPD files. The segmentation process is performed using MP4BOX [12] and the relevant segment and mpd files are stored in related folders. The corresponding paths

of the segments prepared are indicated on the page where the DASH player is embedded.

To examine how the user can perceive a higher QoE with the user-centric system, the new system is compared

Table 1. Adaptation methods.

Adaptation Method	Priority #1	Priority #2	Priority #3
1	FPS	SNR	Audio
2	FPS	Audio	SNR
3	SNR	FPS	Audio
4	SNR	Audio	FPS



Figure 4. The proposed QoE evaluation interface compliant with the SSCQE method of ITU-Rec. 500-11.

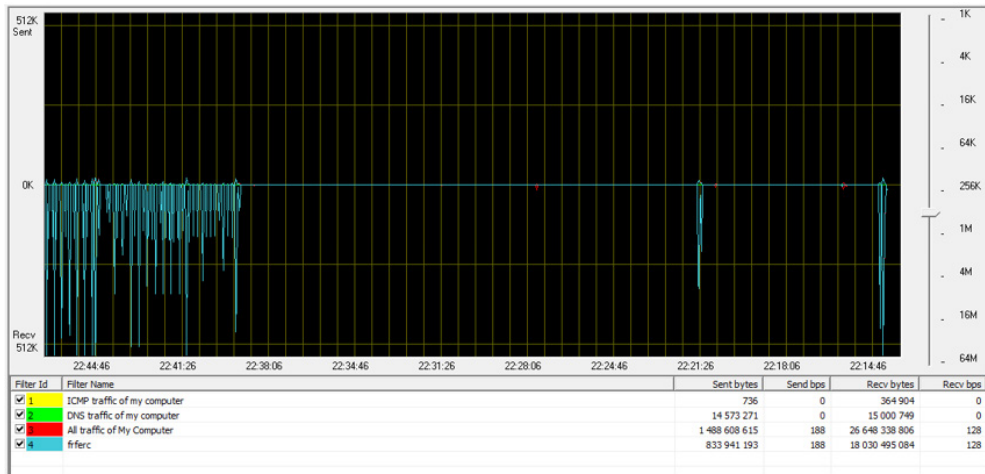


Figure 5. Bandwidth tracking with Tmeter.

to the default adaptation system which is unaware of user's preferences by using subjective quality evaluation. We propose to measure QoE by using SSCQE (Single Stimulus Continuous Quality Scale) method which is recommended for subjective quality assessment of video streaming applications in ITU-Rec. 500-11 [13]. An evaluation interface has been added to the top left of the page to enable on-the-fly evaluation on pages where the player is embedded. Every 5 seconds the viewer is requested to give a rating between 1-5 points as a voted QoE value. For example for a 30-second flow with a total of 6 evaluations, QoE rating is made over 30 points. The proposed QoE evaluation interface is shown in Fig. 4.

Each viewer firstly evaluates the default adaptation method and then the viewer selects the adaptation method according to his/her preferences. After making the selection, the viewer is directed to the relevant adaptation page and evaluates as the first part of the test. The scores obtained in the subjective evaluations are stored in the corresponding txt files, including the name and surname of the participant

and the date and time of the test. After each adaptation, the submission process of the evaluation result is directed to the page containing the relevant php code. The evaluation is recorded in the corresponding txt file of the adaptation evaluated by the php code.

RESULT AND DISCUSSION

The system was installed on a free subdomain with all the necessary files [14]. In order to observe the adaptation during the test, Tmeter [15] was used to limit the available bandwidth. As a result of practical observations, the free subdomain offered up to 4500 kbps and 1700 kbps in average of bandwidth for downloading. Considering the maximum bandwidth of 1600 kbps, it was decided to make a coding at fixed bit rates such as 1600 kbps, 1250 kbps and 850 kbps, with a difference of 350 kbps which could make a difference in perceptual quality. Bandwidth tracking and restriction examples with Tmeter are given in Figs 5 and 6, respectively.

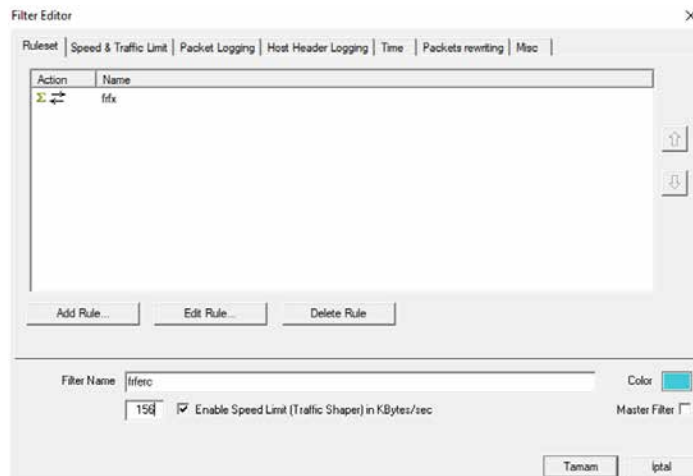


Figure 6. Bandwidth limiting with Tmeter (156 KBps approximately 1250 kbps).

As a source of test content, a Charlie Chaplin video clip at 1280x720 resolution is selected and encoded with an H.264 codec. Table 2 shows how SNR, FPS, and audio bitrate allocations are made according to 4 different adaptation methods to suit 3 different total bitrates. Eq. (1) shows the total bitrate is calculated as sum of video and audio bitrates.

$$\begin{aligned} \text{Total Bitrate } (\sum \mathbf{BR}) \\ = \text{Video Bitrate } (\mathbf{VB}) + \text{Audio Bitrate } (\mathbf{AB}) \end{aligned} \quad (1)$$

A1: When the available bandwidth decreases from 1600 kbps to 1250 kbps, the audio bitrate is reduced to 185 kbps. When the available bandwidth decreases from 1250 kbps to 850 kbps, the video bitrate is reduced to 665 kbps. The 400 kbps drop results in reducing the SNR of the video since the FPS value is kept constant.

A2: When the available bandwidth decreases from 1600 kbps to 1250 kbps, the video bitrate from is reduced to 665 kbps, reducing the SNR of the video. When the available bandwidth drops from 1250 kbps to 850 kbps, the audio bitrate is reduced to 185 kbps.

A3: When the available bandwidth drops from 1600 kbps to 1250 kbps, the audio bitrate is reduced to 185 kbps. When the available bandwidth is reduced from 1250 kbps to 850 kbps, the FPS of video is reduced from 30 to 20, reducing the video bitrate 400 kbps down.

A4: When the available bandwidth drops from 1600 kbps to 1250 kbps, the FPS of video is reduced from 30 to 20, and reducing the video bitrate 400 kbps down. When the available bandwidth drops from 1250 kbps to 850 kbps, the audio bitrate is reduced to 185 kbps.

On the established system, subjective tests were conducted with 15 participants. In the first stage of the test, each participant was presented with the flow using the adaptation method #4 as default, and in the second stage,

Table 2. Allocation methods

	$\sum \mathbf{BR} = 1600\mathbf{k}$		$\sum \mathbf{BR} = 1250\mathbf{k}$		$\sum \mathbf{BR} = 850\mathbf{k}$	
	VB	AB	VB	AB	VB	AB
A1	1065k @30f	535k	1065k @30f	185k	665k @30f	185k
A2	1065k @30f	535k	665k @30f	535k	665k @30f	185k
A3	1065k @30f	535k	1065k @30f	185k	665k @20f	185k
A4	1065k @30f	535k	665k @20f	535k	665k @20f	185k

Table 3. Results of subjective tests as cumulative scores (A1: Adaptation preferred, A4: Adaptation default)

Assessor No.	A1	A4	Assessor No.	A1	A4	Assessor No.	A1	A4
1	25	18	6	25	19	11	21	17
2	23	16	7	23	16	12	23	13
3	18	17	8	27	15	13	26	14
4	23	19	9	22	15	14	27	17
5	26	16	10	23	17	15	27	15

the viewer was asked which adaptation method he would like to watch the same video. All participants preferred the adaptation method #1. The silent Chaplin video selected for streaming, although accelerated during construction like most old movies, has a standard FPS value (25). Instead of the audio quality and the video SNR value, the participants chose not to reduce the FPS value, but to watch the video in a fixed and original FPS. In other words, the most important video feature for the participants was the FPS value and the second was the SNR value. The audio bitrate was not important at all since the test video was from a silent film, having only background music. Note that, different type of contents might lead to different preferences. However, this research was kept as future work.

The cumulative scores of the adaptations are given in Table 3. The QoE value of the adaptation method #1 is computed as average 23.93 over 30; the QoE value of the adaptation method #4 is computed as average 16.27 over 30. The results show that QoE of the user-centric system is superior to QoE of the default system.

CONCLUSION

We proposed a user-centric system for DASH that allows the user to determine the quality adaptation method using preferences and priorities of the viewer. We observed that, when the viewer was given a chance to select the adaptation method, the flow quality assessments provided a higher quality of experience compared to the current DASH system in which the user was generally subjected to certain and single type of adaptation. The user-centric system could be extended by following the streaming experiences of the users, learning their preferences and/or network capacities and offering the user new adaptation methods in this direction. As another future study, it can be searched to merge adaptation decisions with objective QoE measurement methods.

ACKNOWLEDGEMENT

This work was partially supported by the Scientific Research Project of Ege University through a research Grant No. 16MUH017.

References

1. Apple Inc. [http Live Streaming Technical Overview](#), 2013.
2. Zambelli A. [Smooth streaming technical overview](#), 2009.
3. Adobe Systems Inc. [HTTP Dynamic Streaming](#), 2013.
4. DASH Industry Forum. [For Promotion of MPEG-DASH](#), 2013.
5. Sodagar I, Vetro A. The MPEG-DASH Standard for Multimedia Streaming over the Internet. *IEEE Computer Society Industry and Standards* 18 (2011) 62-67.
6. Seyedebrahimi M, Bailey C, Peng X. Client QoE-Oriented Segment Selection for DASH, in: *IEEE International Conference on Computer and Information Technology; Ubiquitous Computing and Communications; Dependable, Autonomic and Secure Computing; Pervasive Intelligence and Computing*. 26-28 October 2015.
7. Gao S, Tao M. Joint multicast scheduling and user association for DASH-based video streaming over heterogeneous cellular networks, in: *IEEE International Conference on Communications in China (ICCC)*. 24 October 2016.
8. Liu Y, Dey S, Gillies D, Ulupinar F, Luby M. User Experience Modeling for DASH Video, in: *Packet Video Workshop (PV)*. 12-13 December 2013.
9. Sieber C, Hofsfeld T, Zinner T, Tran-Gia P, Timmerer C. Implementation and user-centric comparison of a novel adaptation logic for DASH with SVC, in: *IFIP/IEEE International Symposium on Integrated Network Management*. 27-31 May 2013.
10. Reznik Y. User-adaptive mobile video streaming using MPEG-DASH, in: *Proc. SPIE 8856. Applications of Digital Image Processing XXXVI*. 26 September 2013.
11. <https://bitmovin.com/html5-player/>.
12. <https://gpac.wp.imt.fr/mp4box/>.
13. International Telecommunication Union. *ITU-R Recommendation BT.500-11: Methodology for the Subjective Assessment of the Quality of Television Pictures*, 2002.
14. <https://www.000webhost.com/>.
15. <http://tmeter.ru/en/>.

Memristor Based Multi-State Shift Register Architecture

Dincer Gokcen 

Hacettepe University, Department of Electrical and Electronics Engineering, Ankara, Turkey

ABSTRACT

Bio-inspired circuit design attracts a great deal of attention among researchers in the field of electronics. Memristor has emerged not only because of their potential use in neuro-morphic circuits but also because of their feasible fabrication using low-cost techniques. This research presents the use of memristors to build multi-state shift registers. Memristors are capable of storing and processing multi-state logic and design of an architecture for their use in shift register have potential applications in bio-inspired integrated circuits, telecommunication systems, cryptography, display technologies, data storage, chaotic circuits, etc. The designed shift register consists of stages with capability to store and transfer multiple bits. The number of stages can be adjusted depending on the requirements of the specific applications. Each stage of the shift register consists of two memristors for a continuous signal generation at the output of each stage. Reading and writing are executed in sequential order so that when reading operation is performed by a memristor, new data is transferred to another for writing. The amplitude of the voltage corresponds to the logic state and voltage levels are classified into logic states using comparators. For n -state logic, $2n-1$ comparators are required at each stage. Yakopcic's memristor model is used in the simulations conducted in LTSPICE. The multi-state shift register architecture provided in this research successfully stores and shifts the data in the desired logic state.

Keywords:

Memristor, Resistive Switching, Shift Register, Multi-state Logic, Integrated Circuits

INTRODUCTION

Developments in nanofabrication and material technologies have a significant impact on the speed, power consumption, cost and stability of electronic systems. In recent years, memristors have been one of the most important junction points where nanomaterials and electronics met. In the 1970s, Chua put forward the idea that there must be a circuit element defining the relationship between flux and charge [1]. Memristor research remained in theory level until the first practical work done by Williams et al. in 2008 [2]. Since then, in the search for new generation electronic systems, memristors have drawn the attention of the industry.

An active memristive layer, mostly metal oxide, sandwiched by two metal electrodes forms a memristor [2,3]. At this point, the active material is deterministic to obtain the bow-tie I-V hysteresis from the electrical measurements. Since the fabrication of the first memristor by Williams et al., TiO_2 represents one of the most worked out active materials in the literature [4]. The oxygen

vacancies drift in TiO_2 thin films in the same direction with the current flow. Due to the drift of oxygen vacancies in the active layer, the resistance of the memristor (also known as memristance) varies as a function of the voltage applied across its terminals. The memristor stores the last resistance value on it even after the power source is disconnected. All these properties indicate the non-volatility and voltage-dependent resistance characteristics of memristors. Memristors have been subject to various studies including non-volatile resistive memory devices (ReRAM, NVRAM, etc.), bio-inspired and chaotic circuits [5-7]. Additionally, electrical properties of memristors resemble the synapses in the human body since the conduction through the memristor also depends on the strength of the signal passing through it. Artificial neural network applications and multistate data storage represent some of the futuristic properties of memristors. Conventional computation relies on the binary logic where all logical operations, as well as data storage, are done using 1s and 0s. In the case of multi-state (non-binary or multi-valued) logic as in analog and

Article History:

Received: 2019/03/09

Accepted: 2019/07/31

Online: 2019/09/30

Correspondence to: Dincer Gokcen
Hacettepe University, Department of
Electrical and Electronics Engineering
E-Mail: dgokcen@hacettepe.edu.tr

quantum computer architectures, data is processed and stored in states not limited by 1 and 0. For instance, in a 3-state logic, 000, 001, 010, 011, 100, 101, 110, and 111 are used for logical operations and data storage. Multi-state data storage property of the memristors using crossbar array architectures has been subject to some studies in the literature [8-11].

Shift registers, commonly used in counter and memory devices, are composed of a number of flip-flops, which has been one of the essential components used for data storage in conventional binary logic systems. Shift registers scroll the binary data in a specific direction and the number of the bits stored in the shift registers is the same as the number of the flip flops used in the system. Prior to the development of modern memory architectures, shift registers were used as the primary memory structures in computation. Currently, the applications of the shift registers can be found in displays, communication systems, parallel and serial interface conversion and filters [12]. Unlike conventional shift registers using the Boolean systems, memristor-based shift registers can handle multi-state register operations. With the increasing demand on the research of memristor-based computation, the design of a multi-state shift register architecture becomes a necessity for modern data registers, noble communication protocols, and analog computation systems [8-11].

Several research groups elaborated Memristor-based logic gates. Memristor-based material implication (IMPLY) [13], memristor threshold logic [14], memristor-aided logic (MAGIC) [15] and memristors-as-drivers (MAD) [16] represent some of the proposed configurations in the literature executing logic operations using memristors. Likewise research on memristor-based logic gates, there are some memristor-based shift register studies in the literature counting on the single-bit logic [17, 18]. In addition to studies covering single bit operations, memristors have also been investigated in the literature to demonstrate their multi-state data storage capability in ReRAM architecture for multithreaded processors [8]. Due to the non-volatility of memristors, ReRAM can store multistate data even when the power is off. Low power consumption is another advantage of memristor-based memory systems since the power is not supposed to be on all the time. Furthermore, memristors potentially occupy less space in the circuit layout since multiple bits can be stored in a single memristor, rather than sparing a different cell for each bit as in conventional RAM architectures. This study provides an architecture for multi-state shift registers enabling the sequential scrolling of multistate data. Rather than using flip-flops or latches as in binary shift registers, the design, demonstrated herein, shifts the multi-state logic signals from one memristor to another. For validation of the designed architecture, simulations are performed for 4-state shift register operations. Jakopcic's

memristor model is utilized in the simulations while designing a universal shift register relying on the multistate data storage ability of memristors as the primary objective of this research, various memristor models are evaluated throughout the design to extract writing and reading parameters resembling the real device.

BACKGROUND

R_M , the resistance of the memristor (also known as memristance), defines the relation between charge (q) and magnetic flux (ϕ) as given in Eq. 1 [1,2].

$$R_M = \frac{d\phi}{dq} \quad (1)$$

where $\frac{d\phi}{dt} = v(t)$ and $\frac{dq}{dt} = i(t)$. Therefore the voltage ($v(t)$) across the terminals of a memristor is given by Eq. 2

$$v(t) = i(t) \cdot R_M(x) \quad (2)$$

R_M is the resistance of the memristor and $i(t)$ represents the current value. Williams et al. proposed a linear model to express the change in the resistance depending on the ionic drift in the active layer of the memristor [2]. Accordingly, the resistance of the memristor (R_M) is expressed by Eq. 3.

$$R_M(x) = R_{ON}x + R_{OFF}(1-x) \quad (3)$$

Here x is the state variable and given as $x = \frac{w}{D}$, where w is the width of the region with oxygen vacancies (doped region) and D is the total length of the memristor. The state variable value ranges between 0 and 1. R_{ON} and R_{OFF} refer to the maximum and minimum resistances obtained depending on the voltage applied. In a binary logic system, R_{ON} and R_{OFF} correspond to logic 1 and 0 respectively. The shift register architecture given in this research is designed for a memristor with R_{ON} and R_{OFF} values of $120\ \Omega$ and $1.1k\ \Omega$, respectively. In the later studies, several non-linear ionic drift models were worked out to completely define the memristive characteristics of materials. Most of these models were successful at physical boundary conditions of the device, but Pickett's model relying on Simmons tunneling barrier model provides a more realistic approach to the time domain operations [19]. Mathematical expressions are complex and there are a variety of parameters that needs to be determined experimentally. There are some alternative methods proposed due to the complexity of this model. Among these, the device models proposed by Yakopcic et al. [20] and Kvatsinsky et al. [21] (threshold adaptive memristor model (TEAM)) may be the most preferred ones due to the less complexity for simulations.

As mentioned before, this study utilizes Yakopcic's model to simulate working conditions of memristors. According to the model, the motion of state variable is given by Eq. 4 [20].

$$\frac{d(x)}{d(t)} = \eta g(V(t)) f(x(t)) \quad (4)$$

η represents the direction of the motion, $g(V(t))$ defines the threshold to change the state variable, and $f(x(t))$ describes the points (x_n and x_p) at which the state variable do not change. Eq. 5 expresses $g(V(t))$ for possible conditions of $V(t)$

$$g(V(t)) = \begin{cases} A_p (e^{V(t)} - e^{V_p}), & \text{if } V(t) > V_p \\ -A_n (e^{-V(t)} - e^{V_n}), & \text{if } V(t) < -V_n \\ 0, & \text{if } -V_n \leq V(t) \leq V_p \end{cases} \quad (5)$$

Here, V_p and V_n stands for the positive and negative threshold voltages, respectively, whereas A_p and A_n are the multipliers used to adjust how fast state variable changes. $f(x(t))$ is given by Eq. 6.

$$f(x(t)) = \begin{cases} e^{-\alpha_p (x-x_p)w_p(x,x_p)} & , \text{if } x \geq x_p \\ 1, & \text{if } x < x_p \\ e^{\alpha_n (x+x_n-1)w_n(x,x_n)} & , \text{if } x \leq 1-x_n \\ 1, & \text{if } x > 1-x_n \end{cases} \quad (6)$$

Window functions for positive and negative regimes are respectively given as w_p and w_n . α_p and α_n are the parameters defining the constraining factors in the motion of the state variable. Eventually, current change as a function of state variable ($x(t)$) and applied voltage ($V(t)$) can be expressed by hyperbolic functions (Eq. 7).

$$f(x) = \begin{cases} a_1 x(t) \sinh(bV(t)), & V(t) \geq 0 \\ a_2 x(t) \sinh(bV(t)), & V(t) < 0 \end{cases} \quad (7)$$

a_1 , a_2 , and b are the fitting parameters depending on the design and structure of the memristor. For the simulations conducted in this work, the fitting parameters are taken as $a_1=a_2=0.17$, $b=0.05$, $\eta=1$, $A_n=A_p=4000$, $V_n=0.56$, $V_p=0.65$, $\alpha_n=5$, $\alpha_p=1$, $x_0=0.11$ (initial value of the state variable), $x_n=0.5$ and $x_p=0.3$. Shift registers are classified under sequential circuits where circuits work with the clock pulses. The device model and parameters must coincide with the practical working conditions of the modern memory devices and electronics systems to ensure the implementation of the proposed architecture for contemporary technologies.

METHODOLOGY

Writing Operation

In a binary logic system, if R_M approaches to the minimum resistance value of the memristor (R_{ON}), the memristor is set to logic 1. $R_M = R_{ON}$ condition is satisfied when the state variable (x) is 1. On the contrary, if R_M is close to the maximum resistance value of the memristor (R_{OFF}), the memristor is set to logic 0. Fig. 1 demonstrates the voltage, current and resistance waveforms obtained throughout the writing operation at which the resistance changes with the applied voltage. The graphs are plotted by using Yakopcic's model for the memristor. As mentioned before, using Yakopcic's model simplifies the mathematical load of the simulation. It is important to note that the writing process must not consume massive time to ensure that the design is compatible with clocking trend of modern memory devices and electronic systems. The speed of the writing process is determined by several parameters including the applied voltage, mobility of the ions in the active layer, maximum and minimum resistances of the memristor [20,22]. The proposed circuit model works at $\pm 1.8V$. As $+1.8V$ is applied for $200 \mu s$, the state variable increases from 0 to 1, meaning that logic state also switches from 0 to 1. On the contrary, when the voltage source is reverse biased with $-1.8V$, the state variable decreases in the reverse direction within about $200 \mu s$. Consequently, reverse polarities of the applied voltage drive opposite logic conditions. To make the memristor working as a multi-state logic and memory device, knowing the precise values of the state variable are critical. For example, in a 4-state logic device, the ranges of x between 0-0.25, 0.26-0.5, 0.51-0.75, and 0.76-1 refer to 00, 01, 10, and 11 in a 2-bit complimentary system. As given in Figure 2, the x value changes in a logarithmic fashion and 00, 01, 10, and 11 logic states are respectively obtained within $12 \mu s$ (for 125mV), $30 \mu s$ (for 375mV), $72 \mu s$ (for 625mV) and $180 \mu s$ (for 880mV) when $+1.8V$ applied. If the initial state is known, switching one state to another is possible by applying voltage for specific times. However, the initial state (or resistance) of the memristor may not be known before the writing operation, therefore it is crucial to design an automated writing circuit which accurately works no matter what the initial state (resistance) is. In the proposed design, for a reliable writing operation, the memristor state variable is first set to 0 or 1 by applying a constant voltage of $-1.8V$ or $+1.8V$ for $200 \mu s$. Via this technique, without knowing its initial state, the memristor can be set to any value of the state variable by applying negative voltage (e.g. $-1.8V$ for a certain time interval) after preconditioning at $+1.8V$. There are two convenient ways to set the desired value of the state variable: (1) applying varying voltage values for a certain time,

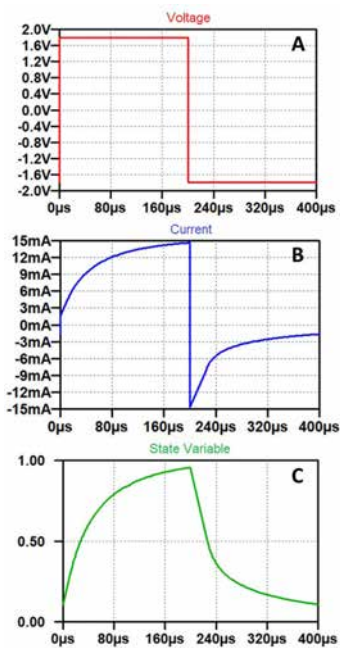


Figure 1. A) Voltage applied across the terminals of the memristor for $400 \mu s$ ($+1.8V$ for $200 \mu s$, $-1.8V$ for $200 \mu s$), B) Current change recorded over the memristor, C) Variations at the state variable (x) during the writing process.

(2) applying a constant voltage of $-1.8V$ for varying time periods. As an example of the first case, applying $-1.8V$ and $-1.2V$ for a constant time of $30 \mu s$ yields different state variables. In the second case, the state variables are at different values when a constant voltage of $-1.8V$ is applied for $20 \mu s$ and $30 \mu s$. The universal shift register design given in this study is capable of running both scenarios.

Reading Operation

The reading of the memristor state is done by applying the zero-net flux condition at which the applied voltage is in square waveform and maximum and minimum voltage values are at the same amplitude but in opposite directions [22]. The stored data on the memristor is not supposed to be affected adversely throughout the readout process. Fig. 2 shows the change at the resistance value of the memristor during the readout process based on the app-

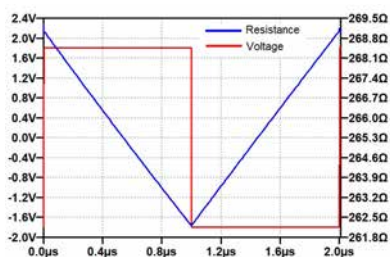


Figure 2. Resistance change during the reading operation (Applied voltage: $+1.8V$ for $1 \mu s$, $-1.8V$ for $1 \mu s$).

lied voltage. Before the readout process, the initial resistance value is 269Ω and after applying $+1.8V$ for $1 \mu s$ and sequentially $-1.8V$ for $1 \mu s$, the same resistance is observed. This indicates the readout condition does not change the resistance and so the state variable of the memristor, if the zero-net flux condition is satisfied. Reading the state of the memristor can be done via operational amplifier based current or voltage reading process [22, 23]. The readout circuit used in this design is given in Section 4. Simply, the amplified voltage amplitude at the output of the opamp corresponds to a state variable. The maximum absolute voltage value must be normalized to the state variable 1, whereas the minimum absolute voltage must be also normalized to the state variable 0. As mentioned earlier, the voltage applied to the input of the opamp is in the form of a square wave, therefore the output voltage appears to be in the triangular waveform and root mean square (RMS) converter or an averaging circuit can be embedded to the system for the simplification in the quantization. An averaging circuit with the bypassing capacitor at the input is a feasible way for implementation. As compared to the writing operation, reading consumes less time, however, for the synchronization purpose, the period is taken the same as the writing process.

RESULTS AND DISCUSSION

The foremost principle that has to be considered at the design of the memristor-based multi-state shift register architecture is that reading and writing operations need to be performed in a sequence. Writing and reading cannot be done at the same time on a single memristor. The sequence can be achieved using two memristors in a stage. While the writing operation is in progress on a memristor, the reading operation is conducted in another one. Unlike the binary systems, one stage stores more than 1 bit. The sequential processes observed at the memristors

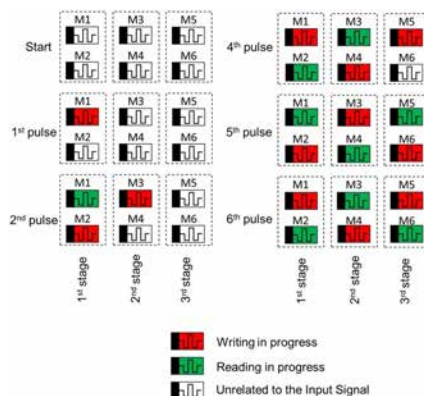


Figure 3. Representation of the initial reading and writing sequences for a three-stage multi-state shift register. Red-colored memristors represent the writing process in the particular memristor, whereas green colored ones indicate the reading process. Non-colored ones symbolize the memristors unrelated to the input signal (this condition is only observable in the initial pulses).

are illustrated in Fig. 3 for a three-stage shift register configuration. The first data package is written to the M1 at the first clock pulse. Here, the term “data package” is used to define random multi-state data. With the second clock pulse, the stored data at M1 is sent to the M3 at the second stage via read-out circuitry. While this read-out process is in progress on M1, the writing operation is performed on M2 for the second data package. The first data transferred to the M3 during the read-out process of M1. Sequentially, the writing at M4 of the second stage continues while the data stored at M3 can be observed at the output of the second stage. Proper clocking and switch connections are vital to achieving a sequential order for the writing and reading processes. At each clock pulse, the read line (RL) switch connected to one of the memristors must be on, whereas write line (WL) switch must be on for the other one. The shift register configuration given in this study is universal and the number of the stages can be extended to any desired level.

Fig. 4 shows the circuit diagram of a 2-stage memristor-based multi-state shift register. This circuit is specifically designed for a 2-bit operation in a single memristor. As discussed before, clock connections of the transmission gates that are used to establish the sequence in the reading and writing are connected with reverse polarities for the same memristor. To maintain a sequential order in the shift register, clock pulses of M1-M3 and M2-M4 must be paired. The input of the first stage is the writing signal for M1 and M2. The input signals are separated in equal time periods to separate the writing times for M1 and M2. When M1 is being written, the M2 is read out and vice versa. The readout connections shown in Figure 4A are connected to the circuitry shown in Fig. 4B. As illustrated in Fig. 4B, each stage has a single readout circuit at which the signal amplified using an opamp. Both inverting and non-inverting configurations can be used in the opamp. Signal transferred per clock pulse classified into voltage levels by using comparators after the amplification. Comparators connected to the decoders determine the logic carried out by the signal. The preferred option to convert the voltage to the state variable is to use a comparator configuration. By this method, the incoming signal from the readout circuit can be segmented into state variables according to the voltage levels. Likewise the comparator stage of the flash ADC architecture, comparators can be supplied by reference voltages determined by voltage divider configuration. Using a comparator, the voltage at the output of the readout opamp is compared with a reference voltage (V_{ref}). Simply, state variables between 0-0.25, 0.26-0.5, 0.51-0.75, and 0.76-1 are classified into logic 00, 01, 10, and 11. Three comparators are required for a 2-bit system because 0.25, 0.5 and 0.75 are supposed to determine the threshold for classification. For instance, in a 2-state readout operation, 0.2V at the output of the opamp refers to logic 00

because when it is compared with V_{ref} values of 0.25V, 0.5V and 0.75V and the output of the comparators give 0V. In case of 0.8V coming from the readout circuit, the outputs of all comparators are 1, so the logic corresponding to 0.8V is 11.

The working principle and combination of the comparators resemble the flash ADC configuration, but there is no encoder in this case. As the number of states increase, the number of comparators is supposed to be also increased. While three comparators are sufficient to conduct a 2-state operation, n-state operation requires 2^n-1 comparators.

After the logic state of the memristor is determined, the logic signal is carried to the input of the second stage. As seen in Fig. 4C, each logic state has a corresponding clock connection. In order to transfer the state of a memristor to another one, a voltage must be applied for a certain time interval at the writing circuit. For instance, in order to write logic 11 to M3, CLK_11 is used and the naming of clock inputs is done according to the logic state they should write. As mentioned earlier in the text, altered voltage values can be used instead of varying clocking. Fig. 5 shows the random input ($V(in)$) and its corresponding outputs of a 5-stage two-state shift register. As seen in the $V(in)$ graph, the voltage value varies while the duty cycle is kept constant. It is important to note that the first output voltage is the signal directly written by the voltage coming from the input. So $V(out1)$ is recorded before it's classified into logic states. For example, the voltage value between $400 \mu s$ and $800 \mu s$ is at around 200mV and since it is lower than 250mV (the boundary between 00 and 01), the corresponding input signal is classified as logic 00. When $V(out1)$ between 1.2ms and

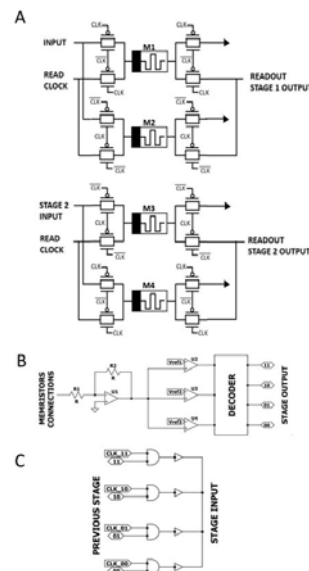


Figure 4. A) Circuit architecture of a two-stage multistate shift register. B) Readout circuitry connected to the outputs of each stage. C) Writing circuitry using voltage or time-varying pulses represented with CLK_00, CLK_01, CLK_10, and CLK_11.

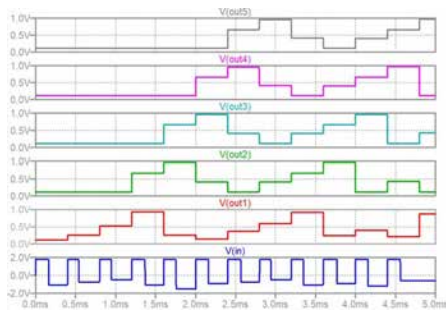


Figure 5. Simulation results demonstrating random 2-state logic shifting in a five-stage shift register. $V(in)$ graph shows the varying applied voltage in a constant clock cycle. $V(out1)$ is the signal observed before the voltage segmentation process in the comparators are completed. $V(out2)$, $V(out3)$, $V(out4)$, and $V(out5)$ are shifted outputs observed in sequential stages. The output voltages are normalized to represent the state variable values.

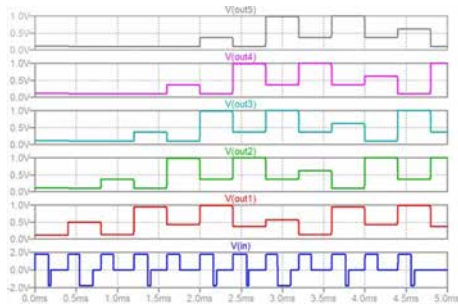


Figure 6. Simulation results demonstrating random 2-state logic shifting in a five-stage shift register. $V(in)$ graph shows the varying duty cycles for the constant applied voltage. $V(out1)$ exhibits the signal waveform observed before the voltage segmentation process in the comparators are completed. $V(out2)$, $V(out3)$, $V(out4)$, and $V(out5)$ are shifted waveforms observed in sequential stages. The output voltages are normalized to represent the state variable values.

1.6ms is checked, it can be seen that the voltage value in that time interval is 900mV and since this value is greater than 750mV (the boundary between 10 and 11), the corresponding input voltage is classified as logic 11. $V(out2)$, $V(out3)$, $V(out4)$ and $V(out5)$ represent the outputs of each state and the graphs demonstrate the shift registering of the $V(out1)$ in sequential order. All output voltage values are normalized to correlate them with the state variable (x). After the readout process at the circuit seen in Fig. 4B, output signals are classified according to the voltage levels. According to the input and the output graphs, the design works properly for the 2-state shift register. Fig. 6 is plotted to exemplify the condition at which $V(in)$ is maintained at a constant voltage and time for pulsing $-1.8V$ varies. Consequently, 2-state memristor-based shift register behavior is successfully observed for a different writing scenario. The state variables are subject to changes depending on the duration of the applied voltage. For some applications, it may be more preferred to vary the duration rather than the voltage and the proposed architecture can be utilized for both scenarios.

CONCLUSION

Memristor-based logic and data storage systems have the

potential to be implemented in advanced electronic devices not as an alternative method, but as a fundamental building block. As an architectural model for a multi-state shift register, the designed memristor-based circuit works with high accuracy. Yakopcic's memristor model is utilized in the simulations due to its accuracy and applicability. Each stage of the shift register has two memristors so that when one is being written the other one is being read. Reading and writing scenarios are designed for the flow of the data in sequential order. A pre-conditioning technique is applied during the writing process to operate the memristor accurately without knowing its initial state. Writing process using both altered clock and voltage values are achieved with the architecture given in the study. The use of memristors in shift-registers to control the clock-based flow of the data represents a crucial task in memristor-based computing and communication systems for future applications. The architecture and the circuit design covered in this study have the potential to be utilized in analog and multi-bit digital computations, as well as chaotic and neuromorphic circuits.

REFERENCES

1. Chua L. Memristor – The missing circuit element. *IEEE Transactions on Circuit Theory* 18-5 (1971) 507-519.
2. Strukov DB, Snider GS, Stewart DR, Williams RS. The missing memristor found. *Nature* 453 (2008) 80-83.
3. Gokcen D, Senturk O, Karaca E, Pekmez NO, Pekmez K. Memristive behavior of TiO_x obtained via Pb(II)-assisted anodic oxidation process. *Journal of Materials Science: Materials in Electronics* (2019) 1-11.
4. Gale E. TiO_2 -based memristors and ReRAM: Materials, Mechanisms and models (a review). *Semiconductor Science and Technology* 29-10 (2014) 104004.
5. Ielmini D. Resistive switching memories based on metal oxides: mechanisms, reliability and scaling. *Semiconductor Science and Technology* 31 (2016) 063002.
6. Muthuswamy B. Implementing memristor based chaotic circuits. *International Journal of Bifurcation and Chaos* 20-5 (2010) 1335-1350.
7. Chang T, Yang Y, Lu W. Building Neuromorphic Circuits with Memristive Devices. *IEEE Circuits and Systems Magazine*, 13-2 (2013) 56-73.
8. Patel R, Kvantinsky S, Friedman EG, Kolodny A. Multistate Register Based Resistive RAM, *IEEE Transactions on Very Large Scale Integration (VLSI) Systems*, 23-9 (2015) 1750-1759.
9. Kim W, Chattopadhyay A, Siemon A, Linn E, Waser R, Rana V. Multistate Memristive Tantalum Oxide Devices for Ternary Arithmetic, *Scientific Reports* 6- 36652 (2016) 1-9.
10. Zhang Y, Cai W, Kang W, Yang J, Deng E, Zhang Y, Zhao W, Ravelosona D. Demonstration of Multi-State Memory Device Combining Resistive and Magnetic Switching Behaviors, *IEEE Electron Device Letters* 39-5 (2018) 684-687.
11. Stathopoulos S, Khiat A, Trapatseli M, Cortese S, Serb A, Valov I, Prodromakis T. Multibit memory operation of metal-oxide bi-layer memristors. *Scientific Reports* 7-17532 (2017) 1-7.
12. Yang B. Low-power and area-efficient shift register using pulsed latches. *IEEE transactions on Circuits and Systems-I: Regular*

- Papers 62-6 (2015) 1564-1571.
13. Kvatinsky S., Satat G., Wald N., Friedman EG, Kolodny A., Weiser, U. C.. Memristor-based material implication (IMPLY) logic: Design principles and methodologies. *IEEE Transactions on Very Large Scale Integration (VLSI) Systems* 221-10 (2014) 2054-2066.
 14. Rajendran J, Manem H, Karri R, Rose GS An energy-efficient memristive threshold logic circuit. *IEEE Transactions on Computers* 61-4 (2012) 474-487.
 15. Kvatinsky S, Belousov D, Liman S, Satat G, Wald N, Friedman EG, Weiser UC. MAGIC—Memristor-aided logic. *IEEE Transactions on Circuits and Systems II: Express Briefs* 61-11 (2014) 895-899.
 16. Guckert L, Swartzlander EE. MAD gates—Memristor logic design using driver circuitry. *IEEE Transactions on Circuits and Systems II: Express Briefs* 64-2 (2017) 171-175.
 17. Guckert L, Swartzlander EE. Optimized memristor-based multipliers. *IEEE Transactions on Circuits and Systems I: Regular Papers* 64-2 (2017) 373-385.
 18. Teimoory M, Amirsoleimani A, Ahmadi A, Alirezaee S, Salimpour S, Ahmadi M. Memristor-based linear feedback shift register based on material implication logic. *European Conference on Circuit Theory and Design (ECCTD)* August, pp. 1-4, 2015.
 19. Pickett MD, Strukov DB, Borghetti JL, Yang JJ, Snider GS, Stewart DR, Williams RS. Switching dynamics in titanium dioxide memristive devices. *Journal of Applied Physics*, 106-7 (2009) 074508.
 20. Yakopcic C, Taha TM, Subramanyam G, Pino RE. Generalized memristive device SPICE model and its application in circuit design. *IEEE Transactions on Computer-Aided Design of Integrated Circuits and Systems*, 32-8 (2013) 1201-1214.
 21. Kvatinsky S, Friedman EG, Kolodny A, Weiser UC. TEAM: Threshold adaptive memristor model. *IEEE Transactions on Circuits and Systems I: Regular Papers*, 60-1 (2013) 211-221.
 22. Elshamy M, Mostafa H, Ghallab YH, Said MS. A novel nondestructive read/write circuit for memristor-based memory arrays. *IEEE Transactions on Very Large Scale Integration (VLSI) Systems*, 23-11, (2015) 2648-2656.
 23. Ho Y, Huang GM, Li P. Dynamical properties and design analysis for nonvolatile memristor memories. *IEEE Transactions on Circuits and Systems I: Regular Papers*, 58-4, (2011) 724-736.

Performance Assessment of Flat Plate Solar Collector Using Different Nanofluids

Mustafa Asker  Tukur Sani Gadanya 

Aydin Adnan Menderes University, Department of Mechanical Engineering, Aydin, Turkey

ABSTRACT

In this work, a numerical study has been performed to investigate the performance of a Flat plate solar collector (FPSC) using five different nanofluids including Al_2O_3 , CeO_2 , Cu , SiO_2 , and TiO_2 as the working fluid with a volume fraction (VF) range of 0-2% and mass flow rate of 0.02kg/s. A computer program written in MATLAB is developed and the equations are solved in an iterative approach to obtain the output temperature. The model is validated through a comparison with an experimental data that is taken from the literature and a good agreement is obtained. A parametric study is done to investigate the effects of VF's on the performance of the collector. The analyses have been conducted for the city of Aydin in Turkey. The results show that for VF of 2%, the maximum efficiency augmentation is observed in SiO_2 nanofluid by 10%.

Keywords:

Flat Plate Solar Collector; Nusselt Number; Thermal Performance; Nanofluid; Entropy

Article History:

Received: 2019/04/03

Accepted: 2019/08/23

Online: 2019/09/30

Correspondence to: Mustafa Asker
Aydin Adnan Menderes University,
Department of Mechanical Engineering
Tel: 0(256) 213 7503
Fax: 0(256) 213 6686
E-Mail: mustafa.asker@adu.edu.tr

INTRODUCTION

The need for renewable energy is gradually been recognized and accepted globally due to the threats the world is facing such as the increase in world population, climate change, fossil fuels price inflation and high cost of electricity. These threats have led to the discovery and development of new, clean and abundant alternative sources of energy called renewable energies. Among these alternative sources of energy includes solar, wind and hydropower.

Solar energy is a free, abundant and natural heat from the sun that is harnessed by solar collection method. It is the common alternative source of energy used today. It can be utilized directly in two forms: either to generate electricity by exposing a photovoltaic material to sunlight or to generate heat for heating or cooling system. For the heating system, the sun's radiation in the form of heat energy is transferred to a working fluid such as the air, water or oil. Use of solar energy for water heating is the most common and easiest application with the use of a solar collector with a flat plate been the most productive type [1]. Enhancing the heat transfer, by maximizing solar absorption and reducing the losses leads to improved efficiency and better performance. In addition, the use of nanofluids is another way for enhancing the performance of the collector. Sharafeldin et al. [2] conducted an experiment to study the effect of using CeO_2 with three different volume fractions (0.0167%,

0.0333% and 0.0666%) and a mean particle size of 30nm which was kept constant as the working fluid. They found that using CeO_2 nanofluid enhanced the efficiency compared to water. Kutlu et al. [3] investigated evacuated flat plate collector integrated with organic Rankine cycle. Their work focused on the system performance simulation for electrical production as well as water heating under different weather conditions. Verma et al. [4] conducted an experimental study using a variety of nanofluids to improve the performance of a FPSC in respect of energy and exergy efficiency by varying the mass flow rate. They found that for an optimum particle VF of 0.75% and mass flow rate of 0.025kg/s, the maximum exergetic efficiency is observed in multiwall carbon nanotubes (MWCNTs), Graphene, Cu , Al_2O_3 , TiO_2 and SiO_2 respectively. They concluded that the collector can be more frugal and efficient by reducing the collector surface area by about 19.11% as well as the use of MWCNTs nanofluid as the working fluid. In another work, Verma et al. [5] used MgO nanofluid as a working fluid. They showed that the thermal efficiency will be improved by 9.34% for 0.75% particle volume concentration. Sharafeldin [6] conducted an experiment to investigate the effect of using WO_3 on the thermal efficiency of a FPSC which operates under the weather condition of Budapest, Hungary. They found that usage of WO_3 nanofluid alleviates the thermal efficiency of the collector. Said et al. [7] used a controlled pH treated Al_2O_3

nanofluid as the working fluid to study its effects on the energetic and exeric efficiencies of a FPSC. An experiment was conducted and the results showed that for an optimum flow rate of 1.5kg/min and VF of 3%, the energetic efficiency increased by 83.5% whereas the exeric was enhanced by 20.3% for a VF of 1% and flow rate 1kg/min when compared with water. In another work, Said et al. [8] studied the thermophysical properties of Al_2O_3 nanofluid and its effect on the performance of a FPSC. They conducted an experiment to investigate the influence of density and viscosity on the pumping power using ethylene glycol/water and the Al_2O_3 . The result obtained showed that Al_2O_3 is preferred against sedimentation and agglomeration and that both their thermal conductivities increases with an increase in concentration. Yousefi et al. [9] performed an experiment to study the effect of using MWCNT and Triton X-100 as the surfactant. They found that for a VF of 2% without surfactant the efficiency decreases whereas, with a surfactant, it increases. Sabiha et al. [10] used single-walled carbon nanotube (SWCNT) to determine its effect on the thermal efficiency of an evacuated tube collector. They showed that the efficiency improved using the nanofluid in place of water as the working fluid. Hawwash et al. [11] developed a model by using ANSYS software to test the performance of FPSC using double distilled water (DDW) as well as Al_2O_3 nanofluid at different VF. They showed that the use of Al_2O_3 nanofluid enhances the efficiency compared to DDW by about 3-18% at both small and high temperature differences. Said et al. [12] used TiO_2 and Polyethylene Glycol (PEG) dispersant. Their results showed that for a constant mass flow rate of 0.5kg/min, both the energetic and exeric efficiencies increased by 76.6% and 16.9% respectively. Qinbo et al. [13] used Cu nanofluid to investigate the effects of working parameters such as temperature, heat gain, frictional resistance and thermal conductivity of the nanofluid on the efficiency of a FPSC. Their results show that for a constant flow rate of 140L/h, VF of 0.1% and particle size of 25nm, the thermal conductivity was enhanced as well as the efficiency by 23.83%. Mahian et al. [14] applied first and second law analysis to examine the efficiency of FPSC connected to minichannel using various nanofluids.

The integration of solar collection with a system is an area that recently received great attention. Bellos and Tzivanidis [15] applied multi objective optimization for FPSC integrated with an absorption chiller driven. They used Cu nanofluid as the working fluid and pure water. Their work indicated that utilizing the nanofluid improved the thermal efficiency up to 2.5%.

The use of nanofluid as the working fluid instead of water to improve the performance of the collector is gaining more attention. Different nanofluids have been studied by many researchers but few investigate which of the nanoflu-

Table 1. General collector specifications [16,17]

Collector parameters	Values
Length of collector	1.8 m
Width of the collector	1.2 m
Length of the absorber plate	1.65 m
Width absorber plate	1 m
Tilt angle θ	37°
Thickness δ	0.0005 m
Optical efficiency $\tau\alpha$	0.962
Centre distance between tubes W	0.1125 m
Number of covers	1
Diameter of riser pipes	0.0125 m
Diameter of header pipes	0.025 m
Back insulation thickness tb	0.04 m
Absorber plate emissivity of ϵ_p	0.07
Glass cover emissivity ϵ_g	0.88
Thermal conductivity of the absorber	386 W/m.K
Thermal conductivity of the insulation	0.044 W/m.K

ids would offer a better performance more than the others. This motivated the authors to investigate the performance of the collector using various nanofluids such as Aluminum oxide (Al_2O_3), Cerium oxide (CeO_2), Copper (Cu), Silicon oxide (SiO_2) and Titanium oxide (TiO_2) for various VF and mass flow rate. In addition, Entropy analysis is implemented to improve the performance of the system.

MATERIALS AND METHODS

Description Of The Problem

The FPSC system that is examined in this work is given in Fig. 1. When solar energy with intensity I incident drop on the outer layer of FPSC, part of it transmitted through the glazing and strikes the absorber plate. While the remaining part is dissipated to the surrounding as a heat loss. The tubes that are connected to the absorber, will be used to heat the working fluid as it passes inside the tubes. A pump is used to circulate the HTF inside the system. The general specifications of the collector are taken from [16, 17] and are summarized in Table 1. The analysis is done based on weather data for Aydın, Turkey.

The following assumptions are made for the analysis:

- A steady state system.
- The thermo-physical properties of the working fluids are constant.
 - The inlet temperature is constant and assumed to be $T_{amb} + 5$ K.
 - The guess temperature is assumed to be $T_{guess} = T_{in} + 10$ K.
- The Fluid flow inside the pipe is uniform.

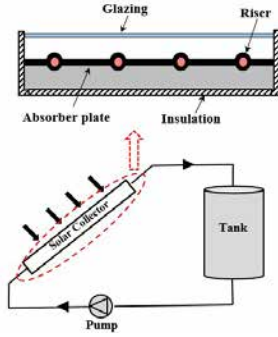


Figure 1. Schematic representation of FPSC system

The performance of a collector is expressed by applying an energy balance on FPSC. There are basically two types of losses that occur in a FPSC which are optical and thermal. The optical loss is shown as $I_T (\tau\alpha)$, where $(\tau\alpha)$ is the optical efficiency depending on the properties of the materials whereas the thermal loss is further divided into three i.e. top loss, bottom loss and edge loss [18].

The Overall heat loss U_L is the summation of the top, back and edge losses

$$U_L = U_t + U_b + U_e \quad (1)$$

Here, U_t can be evaluated as follows [18].

$$U_t = \left[\frac{N_{glass}}{C_1 \left[\frac{T_{abs} - T_{amb}}{N_{glass} + \lambda} \right]^{e_1}} + \frac{1}{h_{wind}} \right]^{-1} + \frac{\sigma(T_{abs} + T_{amb})(T_{abs}^2 + T_{amb}^2)}{(\epsilon_p + 0.0059N_{glass}h_{wind})^{-1} + \frac{2N_{glass} + \lambda - 1 + 0.133\epsilon_p - N_{glass}}{\epsilon_g}} \quad (2a)$$

Where:

$$\lambda = (1 + 0.089h_{wind} - 0.1166h_{wind}\epsilon_p)(1 + 0.07866N_{glass}) \quad (2b)$$

$$C_1 = 520(1 - \beta^2 0.000051) \quad (2c)$$

$$e_1 = 0.430 \left(1 - \frac{100}{T_{abs}} \right) \quad (2d)$$

The natural heat transfer coefficient caused by wind is given as [18]

$$h_{wind} = 5.7 + 3.8V_{wind} \quad (3)$$

The back and edge heat losses can also be determined as [18]

$$U_b = \frac{k_b}{t_b} \quad (4)$$

$$U_e = \left(\frac{k_e}{t_e} \right) \frac{A_e}{A_c} \quad (5)$$

Where k_e and k_b are thermal conductivities of the back and edge insulation respectively, A_e is the edge surface area, t_e and t_b are the thickness of edge and back insulations respectively.

The useful energy output can be written as [18]

$$Q_u = F_R A_c [I_T (\tau\alpha) - U_L (T_i - T_{amb})] \quad (6)$$

F_R denote the heat removal factor and expressed in Eq. (7) [18].

$$F_R = \frac{\dot{m}c_p}{A_c U_L} \left[1 - \exp \left(\frac{-U_L F' A_c}{\dot{m}c_p} \right) \right] \quad (7)$$

Where F' is collector efficiency factor defined as

$$F' = \frac{1/U_L}{W \left[\frac{1}{U_L (D_o + (W - D_o)F)} + \frac{1}{C_b} + \frac{1}{\pi D_i h_{fi}} \right]} \quad (8)$$

Where F is the f_{in} efficiency defined as

$$F = \frac{\tanh \left[m(W - D_o)/2 \right]}{m(W - D_o)/2} \quad (9)$$

Where

$$m = \sqrt{\frac{U_L}{k_c \delta_c}} \quad (10)$$

HEAT TRANSFER IN FPSC

For water as the working fluid, the Gnielinski Correlation [19] is used to calculate the Nusselt number.

$$Nu = \frac{\left(\frac{f}{8} \right) (Re - 1000) Pr}{1 + 12.7 \left(\frac{f}{8} \right)^{0.5} \left(Pr^{\frac{2}{3}} - 1 \right)} \quad 0.5 \leq Pr \leq 2000 \quad (11)$$

The Internal heat transfer coefficient is expressed in term of Nusselt number as

$$h_{fi} = \frac{Nu k}{D_i} \quad (12)$$

For nanofluid as the working fluid, Xuan and Li correlation [20, 21] is used to evaluate Nu for $0 \leq \phi \leq 2$

If the flow is laminar ($Re_{nf} < 2300$).

$$Nu_{nf} = 0.4328 \left(1 + 11.285 \phi^{0.754} (Re_{nf} \times Pr_{nf})^{0.218} \right) \times Re_{nf}^{0.333} Pr_{nf}^{0.4} \quad (13)$$

If turbulent flow ($Re_{nf} \geq 4000$).

$$Nu_{nf} = 0.0059 \left(1 + 7.6286 \phi^{0.6886} (\text{Re}_{nf} \times \text{Pr}_{nf})^{0.001} \right) \times \text{Re}_{nf}^{0.9238} \text{Pr}_{nf}^{0.4} \quad (14)$$

Where Re , Pr stands for Reynolds and Prandtl numbers respectively and are given below.

$$\text{Re} = \frac{4\dot{m}}{\pi D_i \mu} \quad (15)$$

$$\text{Pr} = \frac{\mu c_p}{k} \quad (16)$$

The correlation used to evaluate the k of nanofluids is adapted from [22].

$$k_{nf} = \left[\frac{k_p + 2k_w + 2(k_p - k_w)(1+b)^3 \phi}{k_p + 2k_w - (k_p - k_w)(1+b)^3 \phi} \right] k_w \quad (17)$$

Brinkman [23] suggested an equation to compute the viscosity of the nanofluid as

$$\mu_{nf} = \frac{1}{(1-\phi)^{2.5}} \mu_w \quad (18)$$

The nanofluid density and specific heat are evaluated by using Pak and Cho [24] correlation.

$$\rho_{nf} = \phi \rho_p + (1-\phi) \rho_w \quad (19)$$

$$c_{p,nf} = \frac{\rho_w c_{p,w} (1-\phi) + \rho_p c_{p,p} \phi}{\rho_{nf}} \quad (20)$$

In this study, five different nanofluids which include aluminium oxide (Al_2O_3), cerium oxide (CeO_2), copper (Cu), silicon oxide (SiO_2) and titanium oxide (TiO_2) are used. The thermo-physical properties of the working fluids are listed in Table 2.

A computer program written in MATLAB is used to get the outlet temperature. A moderate value for T_{abs} must be assumed as an initial guess through which U_L , F_R as well as Q_u are obtained. The T_{abs} is calculated by using Eq. (21) and the guessed value is corrected by an iterative approach [18].

Table 2. Thermo-physical properties of nanoparticles [2, 14]

Particle	c_p (J/kg.K)	k (W/m.K)	ρ (kg/m ³)
Al_2O_3	765	40	3970
TiO_2	686	8.9	4250
SiO_2	745	1.4	2220
CeO_2	4175	0.624	999
Cu	385	400	8933
Water	4180	0.6068	997.07

$$T_{\text{abs}} = T_m + \frac{Q_u}{A_c F_R U_L} (1 - F_R) \quad (21)$$

$$\left| \frac{(T_{\text{abs}})_{\text{guess}} - (T_{\text{abs}})_{\text{calculated}}}{(T_{\text{abs}})_{\text{calculated}}} \right| \leq 10^{-8} \quad (22)$$

The outlet temperature is obtained as follow [18]

$$T_{\text{out}} = T_{\text{in}} + \frac{Q_u}{\dot{m} c_p} \quad (23)$$

The thermal efficiency can be expressed as [25].

$$\eta_{\text{en}} = \frac{Q_u}{A_c I_T + \text{Pumping Power}} \quad (24)$$

The total entropy generation [26].

$$\dot{S}_{\text{gen}} = \dot{m} c_p \ln \frac{T_{\text{out}}}{T_{\text{in}}} - \frac{\dot{Q}_s}{T_s} + \frac{\dot{Q}_o}{T_{\text{amb}}} \quad (25)$$

Where, \dot{Q}_s and \dot{Q}_o are the heat absorbed (W) by the collector surface and heat lost to the surrounding (W) respectively.

$$\dot{Q}_s = I_T \eta_o A_c \quad (26)$$

$$\dot{Q}_o = \dot{Q}_s - \dot{m} c_p (T_{\text{out}} - T_{\text{in}}) \quad (27)$$

Pressure Drops

The pressure drop for the FPSC is calculated as follow [27].

$$\Delta P = \left[f \frac{L}{D_i} \left(\rho \frac{V^2}{2} \right) \right]_{\text{in/out header}} + \left[\rho g (L \sin(\beta) + h_L) \right]_{\text{riser+ fittings}} \quad (28)$$

where, h_L represents the total head loss which consist of two parts major and minor losses, is given as follow [28].

$$h_L = \frac{8 \dot{m}^2}{\rho^2 g \pi^2 D_i^4} \left(f \frac{L}{D_i} + \sum K \right) \quad (29)$$

The term f given in Eq. (29) represent the frictional factor which can be evaluated by using Goudar-Sonnad correlation [29]. The reason behind using this correlation is that, it is non-iterative and more accurate [30].

RESULTS AND DISCUSSION

A numerical model has been conducted to investigate the impact of various type nanofluids on the performance of FPSC. In addition, energy analysis is done and the pressure drop is evaluated for different values of mass flow rate and solar radiation. In order to validate the numerical model of this work, the result are compared with experimental data obtained by [15]. The numerical model is observed to be in good agreement with the published work from [15] which make the works reliable as shown in Fig. 2.

Throughout the solution, the solar load is selected as 562 W/m² [31]. Also, wind velocity is taken as 2 m/s [32], $T_{\text{amb}}=308$ K [32] and kg/s with the use of the collector spe-

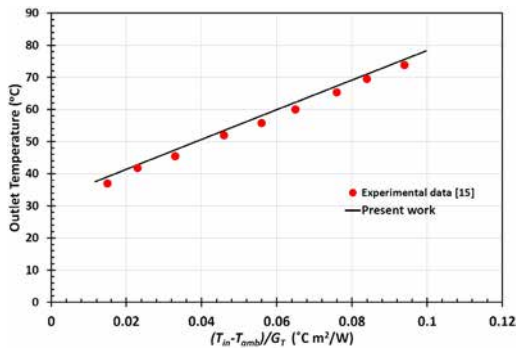


Figure 2. Comparison of outlet temperature with Ref. [15].

cification that is mentioned in Table 1.

Fig. 3 shows the impact of particle VF increase and its influence on the heat transfer performance. In this figure, for Cu nanofluids with 0% VF, the value of $Nu=11.7605$ and $h_{fi}=570.9$ $W/m^2 \cdot K$ based on Eq. (13) and Eq. (14). While for water the value of $Nu=14.0159$ and $h_{fi}=680.3897$ $W/m^2 \cdot K$. by using Eq. (11) and Eq. (12) respectively. Since the convective heat transfer coefficient is proportional to both Nu and thermal conductivity, the it is improved as the VF increases. A maximum increase is observed at VF of 2% in Al_2O_3 . This is obvious, because during particle loading, both the k and μ of the base fluid are augmented. However, the rise in thermal conductivity results to better heat transfer performance whilst increase in viscosity results to development in boundary layer thickness. For the VFs used, the effect of thermal enhancement is higher than that of viscosity. Therefore, the heat transfer increases.

The variation of outlet temperature with VF is shown in Fig. 4. In this figure, at a given value of volume fraction Cu nanofluid provides the maximum outlet temperature whereas SiO_2 nanofluid shows the smallest value. Based on Eq. (23), the outlet temperature is inversely proportional to the heat capacity. By definition, specific heat is the heat required to raise the temperature of a unit mass of a substance by one unit of temperature i.e. the smaller the heat capacity the higher the outlet temperature. Other factors such as density and thermal conductivity also determines higher

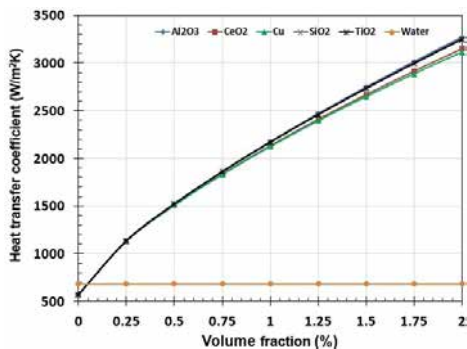


Figure 3. Heat transfer coefficients with respect to VF for different nanofluids.

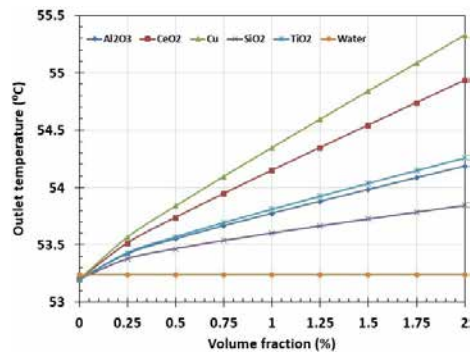


Figure 4. Outlet temperatures against VF for different nanofluids.

outlet temperature. Al_2O_3 shows higher outlet temperature than SiO_2 despite having less heat capacity. The reason is, for a constant mass flow rate, a nanofluid with higher density results to lower velocity which makes it easier to absorb higher thermal energy. Moreover, Al_2O_3 having higher thermal conductivity. The maximum outlet temperature is observed on Cu, CeO_2 , TiO_2 , Al_2O_3 and SiO_2 respectively for VF of 2%. However, the maximum outlet temperature is 55.32 $^{\circ}C$ at 2% VF of Cu.

Fig. 5 depicts the change of thermal efficiency with VF. In this figure, the opposite trend to the outlet temperature with SiO_2 nanofluid providing the highest efficiency whereas Cu nanofluid the smallest. This happened because among all the nanofluids, Cu provides the highest absorber plate temperature and the absorbed energy will be minimized. Therefore, the efficiency reduced. Moreover, the thermal efficiency is a function of VF to a certain limit. The maximum efficiency improvement is “between” 0.75% to 2% for all the working fluids. Besides, the maximum efficiency is observed in SiO_2 by 10%.

To develop an efficient thermal system, entropy generation analysis will play a vital role. Fig. 6 describes the influence of VF on entropy generation. At a given condition, the total entropy generation is diminished by using nanofluid with water. This is because; addition of nanoparticles increases the transfer of heat efficiently due to the augmentation in the value of k for nanofluids. Thus, the irreversibility generated in the system is depressed. The maximum drop

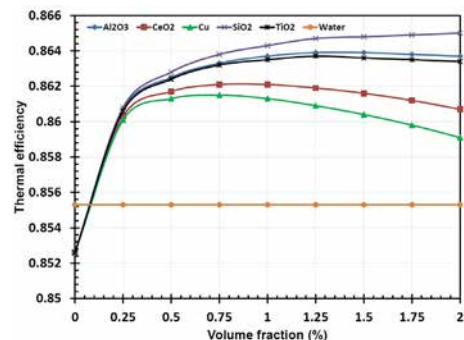


Figure 5. Thermal efficiency against VF for different nanofluids.

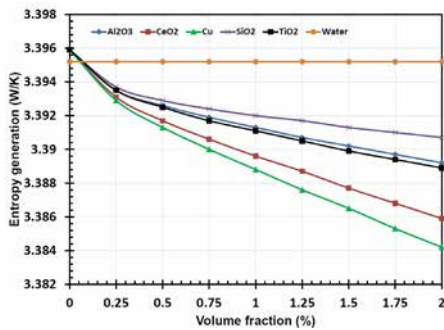


Figure 6. Entropy generation against VF.

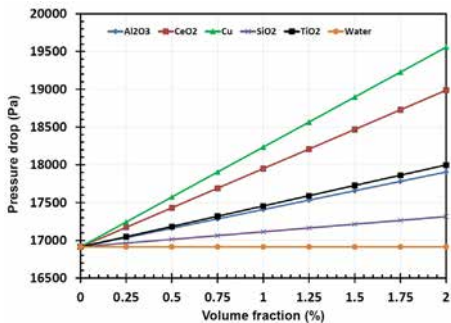


Figure 7. Pressure drop variation with respect to VF.

in entropy generation is observed in Cu, followed by CeO_2 , then TiO_2 , Al_2O_3 and lastly SiO_2 .

Fig. 7 illustrates the variation of pressure drop against the VF for different nanofluids. In this figure, the supplementation of nanoparticles into the water improves its viscosity which results to increase in the frictional factor. It can be seen that at VF=2 for Cu nanofluid the pressure drop is 19559 Pa while for SiO_2 nanofluid is 17315 Pa. As a result, the pressure drop rises with the increasing concentration.

In Figs. 8-10 different values of mass flow rate such as 0.01, 0.02 and 0.03 kg/s are selected to examine its effect on outlet temperature, thermal efficiency and pressure drop correspondingly. the solar radiation and the volume fraction for nanofluids are taken as $562 W/m^2$ and 1.25 respectively.

Fig. 8 exhibits the distributions of outlet temperature for various mass flow rates for different nanofluids. The highest outlet temperature occurs in lowest mass flow rate.

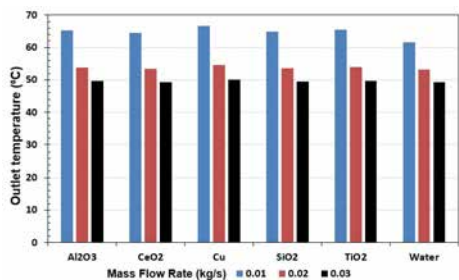


Figure 8. Variation of outlet temperature for different mass flow rate.

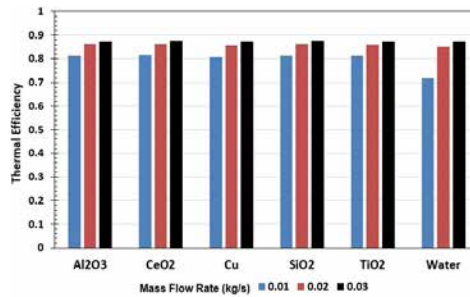


Figure 9. Variation of thermal efficiency for different mass flow rate.

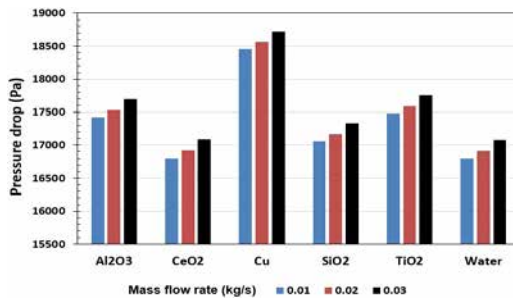


Figure 10. Variation of pressure drop for different mass flow rate.

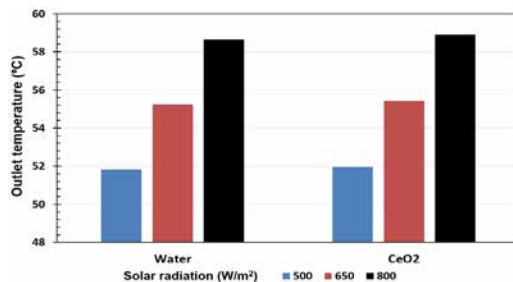


Figure 11. Variation of outlet temperature for different solar radiation.

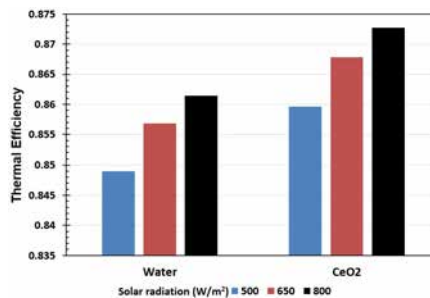


Figure 12. Variation of thermal efficiency for different solar radiation.

In Fig. 9, on the other hand the variation of thermal efficiency is given for different mass flow rate. At maximum value of mass flow rate leads to higher thermal efficiency rates. This because, as the mass flow rate increase the useful energy output will be increased based on equation (6). Therefore, higher thermal efficiency will be obtained according to Eq. (24).

Fig. 10 illustrates the pressure drop for the various nanofluid for different mass flow rate. Increasing the mass flow rate leads to an increase in pressure drop due to direct

proportion of pressure drop with fluid velocity (Equation 28). In addition, the nanofluid exhibiting the highest-pressure drop is copper (Cu).

The effect of solar radiation on the performance of solar collector and pressure drop is analysed. To perform these analyses, cerium oxide (CeO_2) is selected. The mass flow rate for the HTF and the VF for nanofluids are taken as 0.02 kg/s and 1.25 respectively. In addition, three different solar loads (500 W/m^2 , 650 W/m^2 , 800 W/m^2) are selected. Fig. 11 illustrates the variation of outlet temperature for different solar radiation for different nanofluid. As can be seen in Fig. 11, the highest solar radiation results in higher outlet temperature.

Fig. 12 shows the distribution of thermal efficiency for various solar radiation for different nanofluid. As can be seen in Fig. 12, the highest solar radiation lead to an increase in thermal efficiency because of the increase in useful energy output according to Equation (6). Increasing the solar radiation from 500 W/m^2 to 800 W/m^2 with the same flat plate collector area causes the thermal efficiency rate for CeO_2 to increase from 86% to 87.3%.

CONCLUSION

In this study, a computational analysis of FPSC is implemented to investigate the influence of using five different nanofluids which includes Al_2O_3 , CeO_2 , Cu, SiO_2 and TiO_2 for different VF's. Moreover, the influence of mass flow rate for heat transfer fluid (HTF) and solar radiation are also investigated.

We believe that this study is useful for the various thermal design applications.

The following are the results of the study summarized below:

- 1- Al_2O_3 nanofluid shows the highest heat transfer coefficient whereas Cu the smallest.
2. Cu nanofluid provides the highest outlet temperature followed by CeO_2 , TiO_2 , Al_2O_3 and SiO_2 .
3. SiO_2 provides higher thermal efficiency enhancement by up to 10% compared to water at 0.02 kg/s and VF of 2%.
4. Increasing the VF diminishes entropy generation value with maximum drop observed in Cu, CeO_2 , TiO_2 , Al_2O_3 and SiO_2 nanofluids respectively.
5. FPSC with VF of 2% has higher pressure drop which seen in Cu, CeO_2 , TiO_2 , Al_2O_3 and SiO_2 respectively.

Nomenclature

A_c	Collector surface area (m^2)
A_e	Edge surface area (m^2)
c_p	Specific heat (J/kg.K)

D_o	Outer diameter of the collector tube (m)
D_i	Inner diameter of the collector tube (m)
F	Fin efficiency
F'	Collector efficiency factor
f	Frictional factor
g	Gravitational acceleration (m/s^2)
G_T	Incident solar radiation (W/m^2)
I	Heat flux of solar radiation (W/m^2)
k	Thermal conductivity (W/m.K)
L	length (m)
\dot{m}	Mass flow rate (kg/s)
N_{glass}	Number of the glass cover
Nu	Nusselt number
P	Pressure (Pa)
Pr	Prandtl number
Qu	Absorbed energy by plate (W)
Re	Reynolds number
\dot{S}_{gen}	Entropy generation (W/K)
T	Temperature (K)
T_{abs}	Absorber temperature (K)
T_{amb}	Ambient temperature (K)
T_p	Plate temperature of (K)
t_b	Back thickness (m)
te	Edge thickness (m)
V_{wind}	Wind velocity (m/s)
W	Tube spacing (m)

Greek symbols

α	Absorption coefficient
β	Collector inclination angle (degree)
μ	Viscosity of fluid (kg/m.s)
δ_c	Thickness of absorber plate (m)
ϵ	Emissivity
ρ	Density (Kg/m^3)
σ	Stefan-Boltzmann constant ($\text{W}/(\text{m}^2.\text{K}^4)$)
$\tau\alpha$	Optical efficiency
ϕ	Volume fraction of nanofluids

Subscripts

p	Particles
w	Water
nf	Nanofluid
in	Inlet
out	Outlet

Abbreviations

FPSC	Flat plate solar collector
HTF	Heat transfer fluid
VF	Volume fraction

REFERENCES

1. Alima MA, Abdin Z, Saidur R, Hepbasli A, Khairul MA, Rahim NA. Analyses of entropy generation and pressure drop for a conventional flat plate solar collector using different types of metal

- oxide nanofluids. *Energy and Buildings* 66 (2013) 289-296.
2. Sharafeldin MA, Grof G. Experimental investigation of flat plate solar collector using CeO₂ nanofluid. *Energy Conversion and Management*, 155 (2018) 32-41.
 3. Kutlu C, Li J, Su Y, Wang Y, Pei G, Riffat S. Annual Performance Simulation of a Solar Cogeneration Plant with Sensible Heat Storage to Provide Electricity Demand for a Small Community: A Transient Model. *Hittite Journal of Science and Engineering*, 6 (2019) 75-81.
 4. Verma S K, Tiwari AK, Chauhan DS. Experimental evaluation of flat plate solar collector using nanofluid. *Energy Conversion and Management* 134 (2017) 103-115.
 5. Verma, SK, Tiwari AK, Chauhan DS. Performance agumentation in flat plate solar collector using MgO/water nanofluid. *Energy Conversion and Management* 124 (2016) 607-617.
 6. Sharafeldin MA, Grof G, Mahian O. Experimental study on the performance of a flat plate collector using WO₃/Water nano fluids. *Energy* 141 (2017) 2436-2444.
 7. Said Z, Saidur R, Sabiha MA, Hepbasli A, Rahim NA. Energy and exergy efficiency of a flat plate solar collector using pH treated Al₂O₃ nanofluid. *Journal of Cleaner Production*, 112 (2016) 3915-3926.
 8. Said Z, Sajid MH, Alim MA, Saidur R, Rahim NA. Experimental investigation of the thermophysical properties of AL₂O₃-nanofluid and its effect on a flat plate solar collector. *International Communications in Heat and Mass Transfer* 48 (2013) 99-107.
 9. Yousefi T, Farzad V, Ehsan S, Sirus Z. An experimental investigation on the effect of MWCNT-H₂O nanofluid on the efficiency of flat-plate solar collectors. *Experimental Thermal and Fluid Science* 39 (2012) 207-212.
 10. Sabiha MA, Saidur R, Hassani S, Said Z, Mekhilef S. Energy performance of an evacuated tube solar collector using single walled carbon nanotubes nanofluids. *Energy Conversion and Management* 105 (2015) 1377-1388.
 11. Hawwash AA, Abdel Rahman AK, Nada SA, Ookawara S. Numerical Investigation and Experimental Verification of Performance Enhancement of Flat Plate Solar Collector Using Nanofluids. *Applied Thermal Engineering* 130 (2018) 363-374.
 12. Said Z, Sabiha MA, Saidur R, Hepbasli A, Rahim NA, Mekhilef S, Ward TA. Performance enhancement of a Flat Plate Solar collector using Titanium dioxide nanofluid and Polyethylene Glycol dispersant. *Journal of Cleaner Production* 92 (2015) 343-353.
 13. He Q, Zeng S, Wang S. Experimental investigation on the efficiency of flat-plate solar collectors with nanofluids. *Applied Thermal Engineering* 88 (2015) 165-171.
 14. Mahian O, Kianifar A, Sahin AZ, Wongwises S. Performance analysis of a minichannel-based solar collector using different nanofluids. *Energy Conversion and Management* 88 (2014) 129-138.
 15. Bellos E, Tzivanidis C. Performance analysis and optimization of an absorption chiller driven by nano fluid based solar flat plate collector. *Journal of Cleaner Production* 174 (2018) 256-272.
 16. Gunjo GD, Manhanta P, Robi PS. CFD and experimental investigation of flat plate solar water heating system under steady state condition. *Renewable Energy* 106 (2017) 24-36.
 17. Shojaeizadeh E, Veysi F, Kamandi A. Exergy efficiency investigation and optimization of an Al₂O₃/water nanofluid based Flat-plate solar collector. *Energy and Buildings* 101 (2015) 12-23.
 18. Duffie JA, Beckman WA. *Solar Engineering of Thermal Processes*, fourth ed. Wiley, New Jersey, 2013.
 19. Gnielinski V. New equations for heat and mass transfer in turbulent pipe and channel flow. *International Chemical Engineering* 16 (1979) 359-368.
 20. Xuan Y, Li Q. Investigation on convective heat transfer and flow features of nanofluids. *Journal of Heat Transfer* 125 (2003) 151.
 21. Sint N KC, Choudhury IA, Masjuki HH, Aoyama H. Theoretical analysis to determine the efficiency of a CuO-water nanofluid based-flat plate solar collector for domestic solar water heating system in Myanmar. *Solar Energy* 155 (2017) 608-619.
 22. Yu W, Choi SUS. The role of interfacial layers in the enhanced thermal conductivity of nanofluids: a renovated Maxwell model. *Journal of Nanoparticle Research* 5 (2003) 167-171.
 23. Brinkman HC. The viscosity of concentrated suspensions and solution. *The Journal of Chemical Physics* 20 (1952) 571.
 24. Pak BC, Cho YI. Hydrodynamic and heat transfer study of dispersed fluids with submicron metallic oxide particles. *Experimental Heat Transfer* 11 (1998) 151-170.
 25. Genc MA, Ezan MA, Turgut A. Thermal performance of a nanofluid-based flat plate solar collector: A transient numerical study. *Applied Thermal Engineering*, 130 (2018) 395-407.
 26. Bejan A. *Entropy Generation Minimization: the Method of Thermodynamic Optimization of Finite-size Systems and Finite-time Processes*, first ed. CRC Press, Florida, 1996.
 27. White FM. *Fluid Mechanics*. 7th ed. McGraw-Hill, Boston, 2009.
 28. Shamsirgaran S, Assadi KM, Al-Kayiem H, Sharma KV. Energetic and Exergetic Performance of a Solar Flat-Plate Collector Working with Cu Nanofluid. *Journal of Solar Energy Engineering*, 140 (2018) 031002.
 29. Goudar CT, Sonnad JR. Comparison of the iterative approximations of the Colebrook-White equation, *Hydrocarbon Processing*, 87 (2008) 79-83.
 30. Asker M, Turgut O E, Coban MT. A review of non-iterative friction factor correlations for the calculation of pressure drop in pipe. *Bitlis Eren University Journal of Science and Technology*, 4 (2014) 1-8.
 31. Photovoltaic Geographical Information System. <http://re.jrc.ec.europa.eu/pvgis/apps4/pvest.php> (08.07.2018)
 32. Turkish State Meteorological Service. <https://www.mgm.gov.tr/> (08.07.2018)

Effective Processing of Specularite Ore by Wet Magnetic Separation and Reverse Flotation Techniques

Ammar Mahdi Al-Dhubaibi¹, Huseyin Vapur¹ , Soner Top² 

¹Cukurova University, Department of Mining Engineering, Adana, Turkey

²Abdullah Gul University, Department of Materials Science and Nanotechnology Engineering, Kayseri, Turkey

ABSTRACT

The aim of this study was to obtain a high grade and yield percentage of iron concentrate from a specularite ore by using wet magnetic separation and reverse flotation techniques. The processing a specularite sample using wet magnetic separation and reverse flotation method was studied. During the magnetic separation process, particle size was -2000 μm and magnetic field applied at 0.25 T and 0.85 T which were performed at a solid-liquid ratio of 10% and 20% by weight, respectively. In the reverse flotation tests, experimental design (DOE) was applied, statistically. Depressant dosage, collector dosage and flotation time were selected as main parameters. PH value, frother dosage (MIBC) and particle size were constant parameters. The results showed that particle size and magnetic field intensity had a significant effect on the iron concentrate grade and yield for wet magnetic separation. The optimum value of iron concentrate grade was 98.75% at 0.25 T and particle size of -150 μm while the highest value of iron concentrate yield was 67% at 0.75 T and particle size of -74 μm . In the flotation tests, depressant dosage had the greatest influence on the iron concentrate grade while the effect of the collector dosage and froth collection time were less. Froth collection time had the greatest effect on iron concentrate yield. The maximum iron concentrate grade was 90.13% for the following conditions: 5250 g/ton depressant, 1000 g/ton collector and 2-minute froth collection time. The maximum iron concentrate yield was 98.96% for the following conditions: 5250 g/ton depressant, 1500 g/ton collector and 1 min froth collection time under fixed conditions.

Keywords:

Magnetic separation, Reverse flotation, Particle size, Upgrading, Specularite, Experimental design.

INTRODUCTION

In recent years, the world steelmaking industry has been significantly developed. This led to a rapid increase in iron ore production and demand [1]. Iron, which is one of the most useful elements in the world, has plentiful mineral forms. The primary industrial types of iron minerals include oxides and hydroxides and carbonates. Magnetite [Fe_3O_4], hematite [Fe_2O_3], goethite [$\text{FeO}(\text{OH})$], limonite [$\text{FeOOH}\times n\text{H}_2\text{O}$] and siderite [FeCO_3] are the most common iron minerals [2]. Most of the iron ores in the world are in the form either hematite (Fe_2O_3) or magnetite (Fe_3O_4) [3]. Gravity and magnetic separation methods are basic ore processing techniques for obtaining the iron concentrates [4]. Wet low and high intensity magnetic separation methods are appropriate methods to process these ores with high iron content and a high degree

of liberation of iron oxides from gangue [2]. The magnetic separation method is a dominant technique in beneficiation of low-grade iron ores since magnetic separator process has benefits of low operating cost, large capacity and being environmentally friendly [1]. Magnetic separation method depends on magnetic susceptibility of the materials. The magnetic fraction with higher magnetic susceptibility may be valuable or gangue depending upon its end use in a particular process and also the non-magnetic fraction, e.g., separation of magnetite (magnetic) from quartz (non-magnetic), etc. [5].

Also, flotation can also be used for the beneficiation of iron oxides minerals (hematite and magnetite) if the major impurity is quartz [6]. Flotation is a physicoche-

Article History:

Received: 2019/05/10

Accepted: 2019/09/09

Online: 2019/09/30

Correspondence to: Huseyin Vapur

Department of Mining Engineering, Faculty of Engineering, Cukurova University, Turkey
E-Mail: hvapur@gmail.com

mical separation method based on chemical differences in the surface characteristics of the mineral species present in pulp [6] and the efficiency of the process directly proportional to the characteristics of the bubbles produced [7]. This separation procedure has been applied to iron ores since 1931[8-10]. There are 2 types of flotation have been carried out from that period to upgrade the iron ores by froth flotation process including both direct and reverse flotation. The formation processes and the mineralogical composition of iron ores have a significant influence on these separation processes [11]. The market necessities for the higher-grade iron concentrate to improve the productivity of the steel-making industry have increased the significance of the flotation process concerning the classic pre-concentration of iron ores by gravity or magnetic separation [9]. Today, the cationic reverse flotation of quartz is the most commonly used route, which depends on floatability of the quartz with amines partially neutralized with acetic acid, whilst iron ore is depressed by starches [12]. Besides, reverse flotation of quartz has been successfully used for particle size below 150 μm for iron ore separation [13].

The objective of this study is to separate iron concentrate from gangues by using wet magnetic separation and reverse flotation techniques and to investigate the effect of the effective separation parameters (particle size and magnetic field intensity in magnetic separation, corn starch depressant, Aero 343 collector additions and froth collection time in reverse flotation) on the grades and recovery yields of specularite ore.

EXPERIMENTAL

Materials

Specularite sample was obtained from Feke district of Adana in Turkey. The sample contents have been determined by XRF (X-ray fluorescence) analysis using Mini-pal-4 Panalytical device. As shown in Table 1, the sample contains a high ratio of Fe_2O_3 . In addition, the results of the analysis showed high content of both silica and calcium oxide. The mineral phases of the sample have been revealed by XRD (X-ray diffraction) analysis. Rigaku Minflex XRD device has been used for this purpose. XRD patterns have been interpreted with the PDXL software with current database (Fig. 1).

The Fig. 2 was showed the microscope images of specularite ore sample under reflected light microscope (Nikon-YS100). The microscope images were taken by particle size and they were classified (a: $<38 \mu\text{m}$, b: $74+38 \mu\text{m}$, c: $150+74 \mu\text{m}$, d: $500+150 \mu\text{m}$, e: $1000+500 \mu\text{m}$ and f: $2000+1000 \mu\text{m}$

μm). In the microscopic images, white colored particles are quartz minerals while red, black and dark gray colored particles are iron minerals such as goethite, hematite and specularite. The sample, which had the maximum particle size of 90 mm, was crushed by a laboratory-type jaw crusher ($<10 \text{ mm}$) and ground for 12 minutes using a ball mill (the charge volume was 45-50 % of the internal volume of the mill) at 60 rpm drum speed as the critical value in dry conditions. Then samples were sieved into different degrees of fineness: $-2000+1000 \mu\text{m}$, $-1000+500 \mu\text{m}$, $-500+150 \mu\text{m}$, $-150+74 \mu\text{m}$, $-150 \mu\text{m}$, $-74 \mu\text{m}$ and $-106 + 38 \mu\text{m}$. In flotation tests, $-38+0 \mu\text{m}$ sized materials were discharged by desliming. The particle size distribution is shown in Fig. 3.

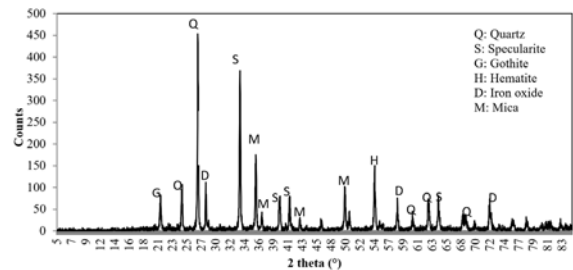


Figure 1. XRD analysis of the sample

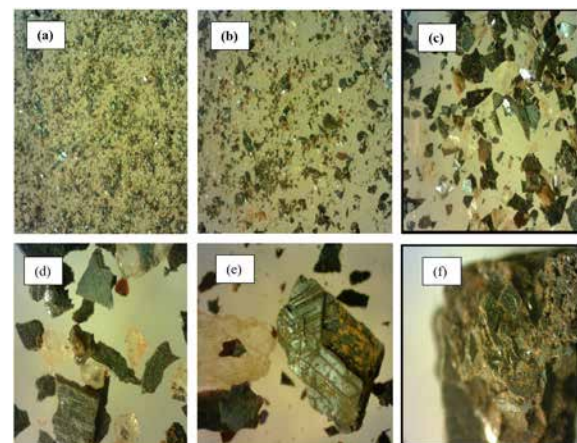


Figure 2. Microscope images of the different sized samples

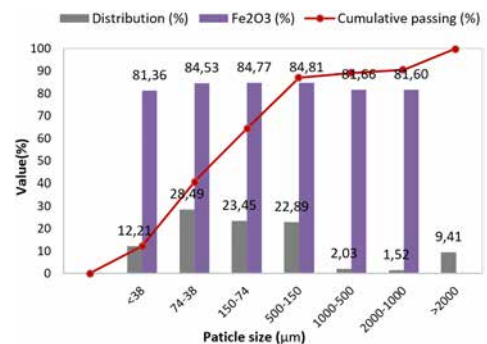


Figure 3. The particle size distribution of the sample

Table 1. XRF analysis of the specularite sample.

Content	Fe_2O_3	SiO_2	CaO	SO_3	La_2O_3	MnO	HgO	Cr_2O_3	CuO	Rb_2O	MoO_3	Y_2O_3	Eu_2O_3	V_2O_5
%	82,78	8,11	8,46	0,3	0,11	0,02	0,025	0,02	0,04	0,03	0,01	0,003	0,07	0,02

Methods

Wet Magnetic Separation Tests

Magnetic separation experiments were carried out using laboratory type high intensity wet magnetic separator (Eriez L4-20). Beneficiation of specularite sample using this separation method divided into two stages. The first stage, samples were prepared according to particle size at five different sizes: -2000+1000 μm , -1000+500 μm , -500+150 μm , -150+74 μm , -74 μm and separation tests carried out at a fixed magnetic field intensity of 0.75 T. All the tests performed at 10% solid ratio by weight (25 g solid/225 ml water). The second stage was performed at 7 different magnetic field intensity; 0.25 T, 0.35 T, 0.45 T, 0.55 T, 0.65 T, 0.75 T and 0.85 T using optimum particle sized sample (-150 μm). This size was selected based on the results of the experiments of the first stage and the experiments in 2nd stage were performed at 20% solid ratio by weight (40 g solid/160 ml water).

Reverse Flotation Tests

The reverse flotation tests were carried out in a batch Denver type flotation machine equipped with a volume of 1 L cell and operating at a fixed impeller speed of 1200 rpm using tap water. The solid/liquid ratio was 10% by weight at the constant value of pH 12.5 in all experiments using sodium hydroxide granulated NaOH (grade >99.0%). Comparing to acidic medium, the flotation of iron oxides and silica was stronger in alkaline medium. As pH increases, the surface charge of oxides increases. The surface charges aim to become more negative, according to previous studies [14-18]. Methyl isobutyl carbinol (MIBC) was used in the experiments as frother and added to the flotation cell at a fixed dosage of 600 g/ton for all experiments. MIBC was added to the cell one minute before froth collection. The froth product was collected at certain time intervals. The particle size was -106+38 μm . MIBC dosage and the particle size were selected based on the preliminary tests. Corn starch is widely preferred in flotation of metallic ores due to its good depressant properties and their low cost [3, 19, 20]. The dosages of corn starch were between 500 – 10000 g/ton. The collector in these experiments was Aero 343. Collector dosages ranged from 500-1500 g/ton. Conditioning time for the depressant was 2 min and was 4 min for collector reagent. Then, it was mixed in 1200 rpm with adjusted pH.

Box Behnken test design, one of the DOE method for response surface, was used to evaluate flotation results. It was preferred due to the presence of more variables in reverse flotation experiments compared to magnetic separation. It is also possible to determine the active parameters more quickly with fewer experiments in this design. The models were created by using Design Expert 11 software shown in Table 2.

Table 2. Box Behnken test design parameters.

Run	A: Collector g/ton (x_1)	B: Depressant g/ton (x_2)	C: Time min. (x_3)
1	1500	10000	2
2	1000	5250	2
3	1500	5250	1
4	1000	500	1
5	1000	10000	3
6	1500	500	2
7	1000	10000	1
8	1500	5250	3
9	1000	500	3
10	1000	5250	2
11	1000	5250	2
12	500	5250	1
13	500	500	2
14	500	10000	2
15	500	5250	3

After each experiment, both concentrate and tailings were dried over 105 °C and then weighed to calculate the recovery of the Fe_2O_3 by using the following equation: Where R is the recovery rate of iron concentrate, F is the weight of the feed solids (%), C is the weight of the concentrate (%), f is metal grade in the feed (%), c is the metal grade in the concentrate (%) [21, 22].

$$\% \text{Recovery} = R = \frac{C_c}{F_f} \times 100 \quad (1)$$

RESULTS AND DISCUSSION

In general, there is an inverse relationship between upgrading and recovery yield, so that when one of them increases, the other decreases. In this study, we tried as much as possible compatibility between them so that the results of the grade and recovery yield are high for both.

Wet Magnetic Separation

Parameters affecting the performance of the wet intensity magnetic separator are particle size and magnetic field intensity, mostly. The effect of each operating parameters on grade and recovery yield of iron concentrate was discussed in the following subtitles.

Effect of Feed Particle Size on Grade and Yield of Iron Concentrate

Wet magnetic separation experiments were carried out to investigate the effect of particle size on the specularite upgrading in the wet magnetic separation as shown in Fig. 4. The results showed that, at a fixed magnetic field intensity of 0.75 T and solid/liquid rate of 10% by weight, the particle size had a significant effect on both grade and yield of iron concentrate. Generally, when the

particle size of the specularite sample was reduced, iron concentrate grade gradually increased and reached to highest value (97,01%) at the particle size of 150 μm . Then, iron concentrate began decreasing lightly when the particle size was decreased. The particle size of the samples also had a particular effect on the iron concentrate yield as illustrated in Fig. 3. At particle size of 2000 μm , iron concentrate yield was at its lowest value as 36.26%. When particle size reduced from 2000 μm , iron concentrate yield significantly increased. A maximum recovery yield (67%) achieved at the particle size of -74 μm . In these experiments, the efficiency of the wet magnetic separator to attract concentrations of iron in large quantities and selectivity was increased by decreasing the particle size at magnetic field strength 0.75 Tesla. Therefore, both the grade and yield of the iron concentrate were increased by decreasing the particle size of the sample.

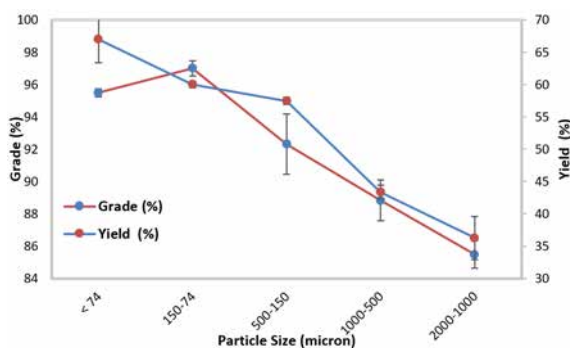


Figure 4. Concentrate grades and yields at different particle sizes in the magnetic separation

Effect of Magnetic Field Intensity on Grade and Yield of Iron Concentrate

Results of wet magnetic separation experiments were seen in Fig. 5. After the optimum particle size range was determined as $-150+0 \mu\text{m}$, the low intensity wet magnetic separation tests were performed at 0.25 T, 0.35 T, 0.45 T, 0.55 T, 0.65 T, 0.75 T, and 0.85 T magnetic field strengths.

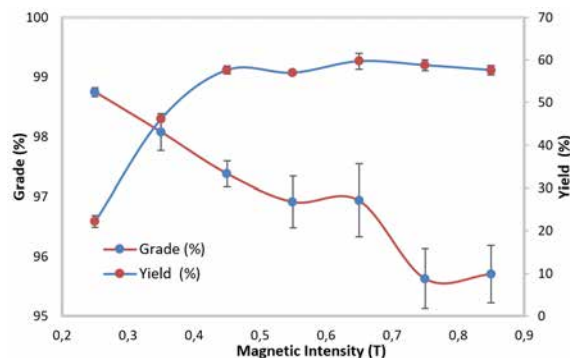


Figure 5. Concentrate grades and yields at different magnetic field intensities.

In Fig. 4, it was concluded that there was a significant effect of the magnetic field intensity on both iron concentrate grade and recovery yield by using wet magnetic separation. In general, iron concentrate grades decreased as the magnetic field intensities increased. When magnetic field intensity was low, the ability of the separator to attract concentrations containing iron-quartz reduced. Only liberated iron particles were attracted at low magnetic fields and this caused increasing ability of the separator to upgrading the sample but in return, yield decreased. At a magnetic field intensity of 0.25 T, iron concentrate grade was at its maximum value of 98.75%. After this point, iron concentrate grade began to decrease slightly with increasing magnetic field intensity due to the attraction of more quartz-iron bearing (non-liberated particles) particulates. At a magnetic field intensity of 0.55 T, iron concentrate grade was increased so slightly by increasing the magnetic field intensity from 96.91% to 96.94% at magnetic field intensity of 0.65 T. Iron concentrate grade began to decrease slightly to 95.63% at magnetic field intensity of 0.75 T which are considered at the lowest value of iron concentrate grade. Iron concentrate yield was directly proportional to the magnetic field intensity except in the intensities of the magnetic fields between 0.45 and 0.85 T, there was a slight variation of iron concentrate yield increases and decreases. The highest value of iron concentrate yield was 59.62% at a magnetic field intensity of 0.65 T.

Reverse Flotation

Reverse flotation experiments were carried out to reveal the role of depressant dosage, collector dosage and froth collection time in the flotation separation of quartz from specularite. Table 3 shows the parameters (collector, depressant and froth collection time) as factors while both grade and yield of the iron concentrate as the response in reverse flotation test for all experiments, which were analyzed in Box-Behnken test design.

Effect of Depressant Dosage on Grade and Yield of the Iron Concentrate

The dosage of the corn starch had a significant and positive effect on iron concentrate grade. Generally, the grade of the iron concentrate was slightly increased with increasing depressant dosages. Fig. 6 shows the effect of the depressant on iron concentrate grade at 500 g/ton, 5250 g/ton and 10000 g/ton conditions, respectively. Using 500 g/ton depressant, iron concentrate grade was decreased at increasing collector and froth collection times. At a depressant dosages of 5250 g/ton, iron concentrate grade was slightly increased by increasing collector and froth collection times. The highest grade of iron concentrate (90.13%) was obtained the medium values of collector and froth collection time. At depressant dosage of 10000

Table 3. The factors and responses which were analyzed in Box Behnken test design in reverse flotation tests.

Run	Collector g/ton (x ₁)	Depressant g/ton (x ₂)	Time min. (x ₃)	Iron Concentrate Grade (%)	Iron Concentrate Yield (%)	SiO ₂ (%)	CaO (%)
1	1500	10000	2	89.78	95.74	6.01	3.91
2	1000	5250	2	90.13	96.85	6.00	4.05
3	1500	5250	1	89.02	98.96	7.03	4.18
4	1000	500	1	88.67	98.65	7.00	4.06
5	1000	10000	3	89.98	93.80	6.01	3.75
6	1500	500	2	87.21	96.24	7.80	4.50
7	1000	10000	1	87.27	96.57	8.20	4.11
8	1500	5250	3	90.05	92.93	6.00	3.65
9	1000	500	3	88.03	93.15	7.50	4.24
10	1000	5250	2	89.09	95.05	7.01	3.98
11	1000	5250	2	89.06	95.04	7.03	4.14
12	500	5250	1	89.43	94.76	6.03	4.16
13	500	500	2	88.06	91.09	7.01	4.38
14	500	10000	2	88.54	93.23	7.10	4.08
15	500	5250	3	89.23	92.40	6.02	4.05

g/ton, iron concentrate grade was continue to increase with increasing both collector and froth collection time and the general effect of the depressant dosage on the iron concentrate grade at this dosage was more positively comparing at lower dosages of depressant. High pH values have the effect of increasing the effect of corn starch [3]. Experiments in this study conducted at pH 12.5 also resulted in >90% iron concentration grades (Fig. 6). Effect of the depressant dosages on specularite at 500 g/ton, 5250 g/ton and 10000 g/ton were shown in Fig. 7.

As shown, the effect of the depressant on the iron concentrate yield was negative and the effect was almost the same for all experiments. At different dosages of depressant, the iron concentrate yield was increased with increasing collector dosage and decreasing froth collection time. The

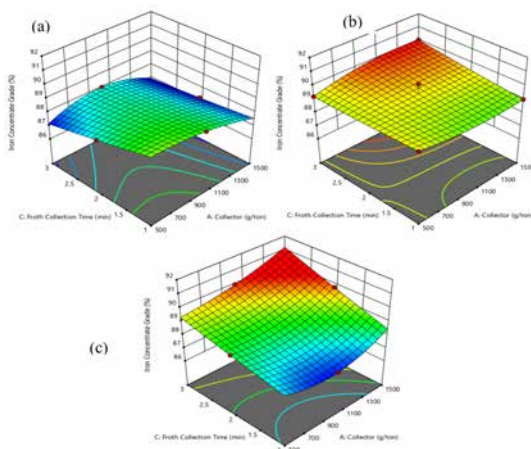


Figure 6. Effect of depressant dosage: 500 g/ton (a), 5250 g/ton (b), and 10000 g/ton (c) on iron grade (%)

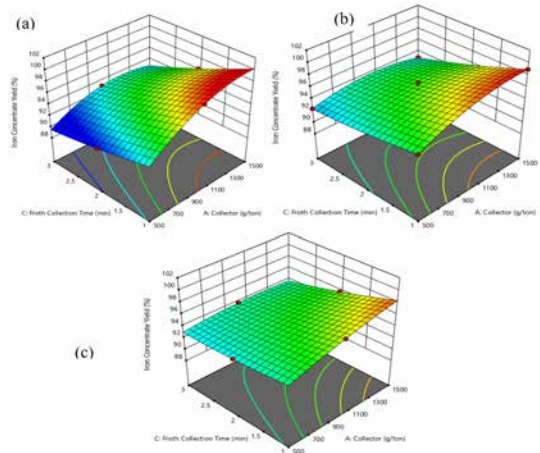


Figure 7. Effect of depressant dosage: 500 g/ton (a), 5250 g/ton (b) and 10000 g/ton (c) on iron yield (%)

highest value of iron concentrate recovery (98.96%) was achieved by 5252 g/ton of depressant usage at 1500 g/ton collector and 1 min froth collection time.

Effect of Collector Dosage on Grade and Yield of the Iron Concentrate

As seen in Fig. 8, under the highest depressant and froth collection time conditions, Fe₂O₃ grade increased according to the increase in the Aero 343 collector dosage. When 500 g/ton collector was used, iron concentrate grade was slightly increased with the increase of the depressant. Then, iron concentrate grade was slightly decreased with increased depressant values but iron concentrate grade continued to increase by increasing the depressant at froth collection time of 3 minutes. When collector was used more than 1000 g/ton and both of the depressant and froth collection time were at the highest values, the effect of Aero 343 on iron concentrate grade was positive. While the collector dosage was the lowest, more flotation time and highest values of depressant were needed to obtain high-grade concentrate. No significant increase was observed in the iron grades after 5000 g/ton of depressant and 2 min of froth collection time. At collector dosage of 1500 g/ton, the effect of the froth collection time on iron concentrate grade remained the same at the lower froth collection times (1-2 min). The maximum iron content was obtained with the depressant dosage (5252 g/ton) for 2 min (Fig. 8).

The effect of the 500 g/ton, 1000g/ton and 1500 g/ton collector dosages on iron concentrate yield were shown in Fig. 9. The collector dosage had a positive effect on iron concentrate yield. However, the iron concentrate yield increased according to the increase in the collector dosage and the decrease in both depressant dosage and froth collection time. iron concentrate yield reached its highest value at 1500 g/ton collector dosage. At this test, depressant and froth collection time were 500 g/ton and 1 min, respectively.

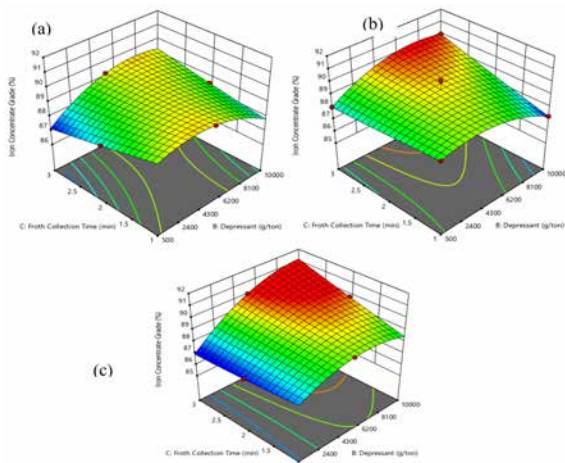


Figure 8. Effect of collector dosage: 500 g/ton (a), 1000 g/ton (b) and 1500 g/ton (c) on iron grade (%)

Effect of Froth Collection Time on Grade and Yield of the Iron Concentrate

The effect of froth collection time on iron concentrate grade was observed and the results obtained as shown in Fig. 10 at froth collection times of 1, 2 and 3 min, respectively. Generally, the effect of froth collection time on the iron concentrate grade was not stable. However, the effect was positive at 3 min and the highest values of depressant and collector. For 1 min collection time, iron concentrate grade was slightly increased with the increase in the depressant adding and then iron concentrate grade began to decrease slightly with the increase in the depressant dosage.

When 3350 g/ton depressant and 500 g/ton collector were used, the iron concentrate grade began to decrease slightly. Under the 1500 g/ton collector usage condition, a significant increase in Fe₂O₃ grade seems to be obtained according to the increase in depressant dosage. While the other variables were at the highest value, the iron grade was obtained at the highest value for 3 min froth collection time.

Froth collection time had the greatest effect on the iron concentrate yield as shown in Fig. 11. When froth collection time was 1 min, where 5250 g/ton depressant and 1500 g/ton collector were used, iron concentrate yield reached 98.96%. In standard flotation tests, recovery yields increase with increasing froth collection times. Nevertheless, this phenomenon is vice versa in reverse flotation method which floats the gangue minerals. When the froth collection times were increased, the iron concentrate yields were decreasing, gradually. The yield reached its lowest value at the froth collection time of 3 min. iron concentrate yield was in its lowest value when the values of depressant and collector were at their lowest points. The grade values in Fig. 11 confirm the recovery yield values in figure.

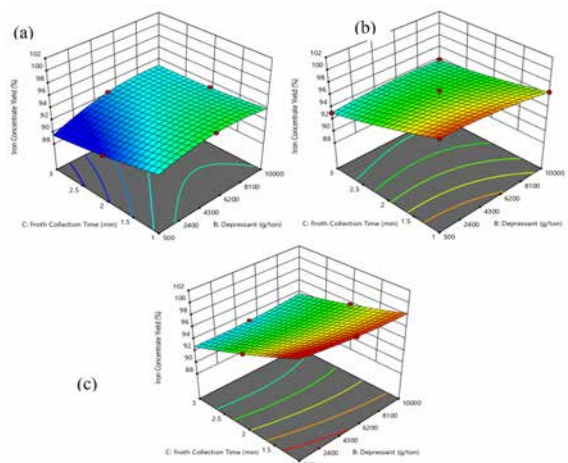


Figure 9. Effect of collector dosage: 500 g/ton (a), 1000 g/ton (b) and 1500 g/ton (c) on iron recovery yield (%)

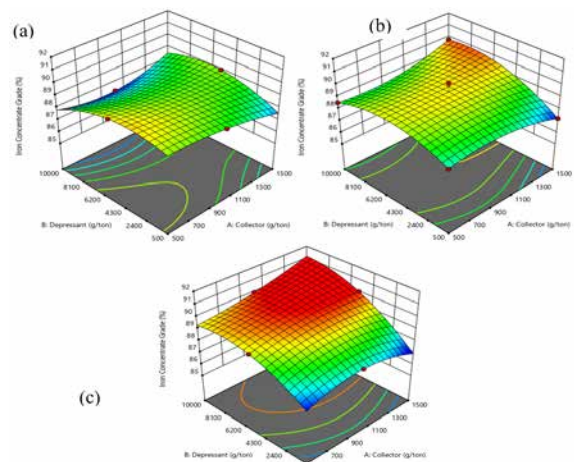


Figure 10. Effect of froth collection time (minute) on iron grade(%): 1 (a), 2 (b) and 3 (c)

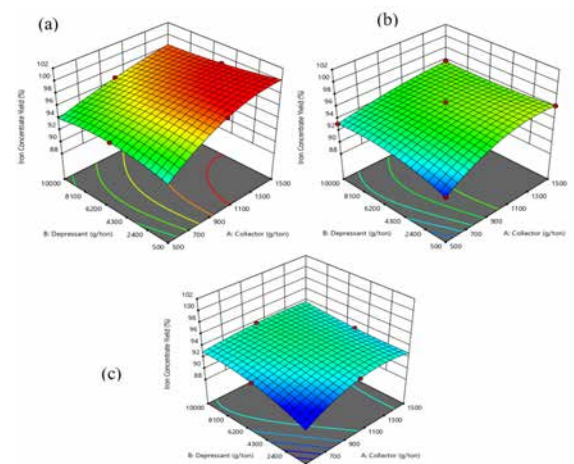


Figure 11. Effect of froth collection time (minute) on iron yield(%): 1 (a), 2 (b) and 3 (c)

ANOVA tests revealed that iron concentrate grade and recovery yields could be explained by cubic models using DOE. The correlation coefficients (R²) for iron concentrate

grade and yield were calculated as 0.94 and 0.97, respectively. It was shown a good correlation for parameters. The equations 2 and 3 show the obtained models:

$$\begin{aligned} \text{Fe}_2\text{O}_3\text{grade} (\%) &= 89.43 + 0.103 X_1 \\ &+ 0.138 X_2 + 0.518 X_3 + 0.523 X_1 X_2 \\ &+ 0.30 X_1 X_3 + 0.838 X_2 X_3 - 0.042 X_1^2 \\ &- 0.9887 X_2^2 + 0.048 X_3^2 + 0.625 X_1^2 X_2 \\ &- 0.31 X_1^2 X_3 - 0.005 X_1 X_2^2 \end{aligned} \quad (2)$$

$$\begin{aligned} \text{Fe}_2\text{O}_3\text{yield} (\%) &= 95.65 + 1.18 X_1 \\ &- 0.358 X_2 - 20.7 X_3 - 0.66 X_1 X_2 \\ &- 0.918 X_1 X_3 + 0.683 X_2 X_3 - 1.18 X_1^2 \\ &- 0.396 X_2^2 + 0.292 X_3^2 + 0.768 X_1^2 X_2 \\ &- 0.03 X_1^2 X_3 - 0.733 X_1 X_2^2 \end{aligned} \quad (3)$$

Where; X_1 : collector dosage (g/ton), X_2 : depressant dosage (g/ton) and X_3 : froth collection time (min).

CONCLUSION

Upgraded iron ores are indispensable raw materials that can be used in iron-steel and paint industries. As a result, it was possible to obtain Fe_2O_3 concentrates in the grades that can be used by the industry (>85% Fe_2O_3) by separating the specularite mineral from the gangues using physical (magnetic) and physicochemical (flotation) separation techniques. The wet magnetic separation method was selected to beneficiate specularite ore in terms of iron concentrate grade. The optimum conditions of tests were determined as follows: 0.75 T magnetic field intensity, -74+0 μm particle size and 20% solid/liquid ratio. In the wet magnetic separation process, both particle size and magnetic field intensity had a significant effect on grade and recovery yield of iron concentrate. At constant magnetic field intensity of 0.75 T and solid/liquid ratio of 20% by weight, when the particle size of the specularite sample was reduced, iron concentrate grade gradually increased. At fixed particle size of -150+0 μm and solid/liquid ratio of 20%, iron concentrate grade was increased with decreasing magnetic field intensities. At 0.25 T magnetic field intensity, iron concentrate grade was at the highest value. In low intensity wet magnetic separation tests, when the magnetic field intensity was increased, the grade and yield were inversely proportional to each other. The maximum value of iron concentrate grade was 98.75% (with 22.23% yield) at 0.25 T, -150+0 μm particle size and 20% solid/liquid ratio while the highest value of iron concentrate recovery yield was 67% (with 95.49% iron concentrate grade) at 0.75 T and particle size of -74+0 μm and 20% solid/liquid ratio.

Flotation method in a magnetic field were used recently in numerous studies [23, 24]. In the next stage of the study,

it is planned to investigate the effect of the combination of these two methods by applying flotation in the magnetic field. In the reverse flotation method the optimum conditions were as follows: 5250 g/ton corn starch, 1000 g/ton Aero 343 collector, 600 g/ton MIBC, 2 min froth collection time at pH 12.5 and -106+38 micron particle size. The tests indicated that iron concentrate grade especially increased with the increase in corn starch dosages. Because the iron depression ability of the corn starch was positively related to the depressing of specularite ore and to its optimum solubility at high PH condition. Froth collection time also had a crucial effect on the iron concentrate grades. While the froth collection time was 1 min, the iron yield was the highest. When the froth collection time was 3 min, the iron content was the highest but the yield was low. The reverse flotation of quartz caused this result. As noted, collector dosage and froth collection time had almost the same effect on iron concentrate grade. Optimum flotation test conditions for the best iron concentrate grade (90.13% with 96.85% recovery yield) were as follows: 5250 g/ton corn starch, 1000 g/ton Aero 343 collector, 600 g/ton MIBC, 2 min froth collection time at pH 12.5 and -106+38 particle size. In terms of iron concentrate yield, the depressant had a negative effect, whereas the effect of the collector dosage was significant. Also, iron concentrate yields were increased by Aero 343 collector additions. The froth collection time had the greatest effect on the iron concentrate yield. The highest iron concentrate yield (98.96% with 89.02% iron concentrate grade) was obtained at optimum conditions: 5250 g/ton corn starch, 1500 g/ton Aero 343, 600 g/ton MIBC, 1 min froth collection time and -106+38 micron particle size.

ACKNOWLEDGEMENTS

This study was supported by Department of Scientific Research Projects, Cukurova University, (Project No: FLY-2019-11823).

References

- Xiong, D., L. Lu, and R. J. Holmes. "Developments in the physical separation of iron ore: magnetic separation." *Iron Ore*. Woodhead Publishing, pp. 283–307, 2015.
- Filippov, L. O., V. V. Severov, and I. V. Filippova. "An overview of the beneficiation of iron ores via reverse cationic flotation." *International journal of mineral processing* 127 (2014): 62–69.
- Yang, Siyuan, Chao Li, and Liguang Wang. "Dissolution of starch and its role in the flotation separation of quartz from hematite." *Powder technology* 320 (2017): 346–357.
- Seifelnassr, Ahmed AS, Eltahir M. Moslim, and Abdel-Zaher M. Abouzeid. "Concentration of a Sudanese low-grade iron ore." *International Journal of Mineral Processing* 122 (2013): 59–62.
- Das, Avimanyu, and Subrata Roy. "Magnetic Separation-

- Principles and Application in Beneficiation of Iron Ores." pp. 89-102, 2007.
6. Laitinen, Ossi, et al. "Use of chemically modified nanocelluloses in flotation of hematite and quartz." *Industrial & Engineering Chemistry Research* 53.52 (2014): 20092-20098.
 7. Haryono, Didied, et al. "The Effect of Flotation Reagents Addition (MIBC and PAX) on the Relative Permittivity Value Using 2-Electrode Capacitance Sensor." *Procedia engineering* 170 (2017): 369-372.
 8. Crabtree, E. H., and J. D. Vincent. "Historical outline of major flotation developments." *Froth Flotation-50th Anniversary Volume*. AIME New York, NY, (1962): 39-41.
 9. Houot, R. "Beneficiation of iron ore by flotation-review of industrial and potential applications." *International Journal of Mineral Processing* 10.3 (1983): 183-204.
 10. Ma, Mark. "Froth flotation of iron ores." *Int. J. Min. Eng. Miner. Process* 1.2 (2012): 56-61.
 11. De Melo, C. V., de Araujo, A. C., & Filippov, L. "Reverse cationic flotation of iron ores with complex silicate gangue minerals." *Conf. Proc. Iron Ore*, pp. 241-244, 2017.
 12. Yang, David C. "Reagents in iron ore processing." Marcel Dekker, Inc., *Reagents in Mineral Technology*, (1988): 579-644.
 13. Lima, Neymayer P., George ES Valadão, and Antonio EC Peres. "Effect of amine and starch dosages on the reverse cationic flotation of an iron ore." *Minerals Engineering* 45 (2013): 180-184.
 14. Fuerstenau, D. W. "Streaming potential studies on quartz in solutions of aminium acetates in relation to the formation of hemi-micelles at the quartz-solution interface." *The Journal of Physical Chemistry* 60.7 (1956): 981-985.
 15. Fuerstenau, D. W. "Correlation of contact angles, adsorption density, zeta potentials, and flotation rate." *Trans. AIME* 208 (1957): 1365-1367.
 16. Iwasaki, Iwao, S. R. B. Cooke, and Arthur F. Colombo. "Flotation characteristics of goethite." (1960).
 17. Somasundaran, P., Thomas W. Healy, and D. W. Fuerstenau. "Surfactant adsorption at the solid-liquid interface-dependence of mechanism on chain length." *The Journal of Physical Chemistry* 68.12 (1964): 3562-3566.
 18. Smith, R.W., Haddenham, R., Schroeder, C. "Amphoteric surfactants as flotation collectors." *Trans. AIME* 254 (1973): 231-235.
 19. Araujo, A. C., P. R. M. Viana, and A. E. C. Peres. "Reagents in iron ores flotation." *Minerals Engineering* 18.2 (2005): 219-224.
 20. Kar, Bhagyaxmi, et al. "Investigations on different starches as depressants for iron ore flotation." *Minerals Engineering* 49 (2013): 1-6.
 21. Wills, Barry A., and James Finch. *Wills' mineral processing technology: an introduction to the practical aspects of ore treatment and mineral recovery*. Butterworth-Heinemann, pp. 258-342, 2005.
 22. Rao, DV Subba. *Minerals and coal process calculations*. CRC Press, 2016.
 23. Birinci, M., Miller, J. D., Sarıkaya, M., Wang, X. "The effect of an external magnetic field on cationic flotation of quartz from magnetite." *Minerals Engineering* 23.10 (2010): 813-88.
 24. Manouchehri, H-R. "Magnetic conditioning of sulfide minerals to improve recovery of fines in flotation - a plant practice." *Minerals & Metallurgical Processing*; Littleton 35.1 (2018): 46-54

Characterization of Iron Nanowires Fabricated by Electrodeposition into Polycarbonate Template

Halil Yılmaz¹  Mustafa Kocabas² 

¹Mus Alparslan University, Department of Mechanical and Metal Technologies, Mus, Turkey

²Konya Technical University, Department of Metallurgy and Materials Engineering, Konya, Turkey

ABSTRACT

In the present study, commercially available polycarbonate (PC) membranes with different pore diameters were used as a template for electrodeposition of iron nanowires. The iron nanowire forests with average diameters ranging from 125 to 800 nm and several microns in length have been fabricated by reduction of metal ions into the nano-channels of PC templates. The morphology and microstructure of the iron nanowire forests have been characterized by a scanning electron microscope (SEM) and transmission electron microscope (TEM). The SEM results revealed that iron nanowires have a straight and cylindrical shape. TEM studies revealed a polycrystalline nature for the nanowires. These results showed that the iron nanowires prepared by PC templates are long-term promising candidates for the investigation of the size effect dependence of their properties.

Keywords:

Iron nanowires; Polycarbonate template; Electrodeposition; Body-centered cubic; Characterization

Article History:

Received: 2019/05/22

Accepted: 2019/07/16

Online: 2019/09/30

Correspondence to: Halil Yılmaz,
Department of Mechanical and Metal
Technologies, Mus Alparslan University,
49250, Mus, Turkey
E-mail: halil.yilmaz@alparslan.edu.tr;
Telephone: +90(436) 249 49 49 (2532)

INTRODUCTION

The properties of metallic materials with small dimension have gained increasing attention and have been extensively investigated because of their distinct properties in comparison to bulk counterparts [1]. A number of reports have been published on the compression and tension strength of metallic nanowires/pillars of diameters $< 5 \mu\text{m}$. In all cases the strength of the wires/pillars increases with decreasing specimen diameter. This is called a size effect or “smaller is stronger” phenomenon. This size effect observation was first introduced by Uchic et al. with experimental studies on Ni nanopillars [2, 3] and followed by researches on a number of face-centred cubic (fcc) and body-centred cubic (bcc) metals. [4-6] Similar size effect behavior is observed for the mechanical behaviors of other specimens with small volumes, e.g. in thin films. The small sample dimension eliminates many of the features that control the strength in bulk metals. Dislocation interactions with free surface or confinement of dislocation strongly affect the mechanical properties. [7]

Metallic nanowires are used in several applications such as optical devices, batteries, semiconductors, or micro-electromechanical systems (MEMS). The me-

tallic nanowires have also been proposed as essential components of flexible, electrically-conductive systems. Therefore, nanostructured materials have been investigated owing to their excellent properties, having usually superior mechanical behavior compared to their bulk counterparts [8, 9]. Understanding of the deformation mechanisms and mechanical properties of miniaturized materials is essential in order to design micro/nanodevices with high reliability. Iron nanostructured materials are relatively inexpensive, they have low toxicity, and most of them are biocompatible. Therefore, they have been used in biomedical applications such as magnetic resonance imaging and in direct drug delivery systems [10]. In addition to biomedical applications, iron-based nanostructures can also be used in the fields of catalysis, energy and data storage. [11-13]

In the fabrication of nanostructured materials, several manufacturing techniques have been widely used including a template-assisted approach, nanoimprint lithography, and electron and beam processing [14-16]. These techniques enable to achieve and control the final shape of products with high accuracy. However, they are laborious, ineffective and expensive techniques on large-scale fabrication processes. Among these tech-

niques, the most effective method to fabricate nanostructured materials with tailorable dimensions is the template-assisted approach. The anodic aluminum oxide (AAO) and polymer membranes are widely used as commercially available templates [17]. Pore diameters of the AAO templates can be tailored within the range of 10-200 nm, and the thickness of the templates can be controlled from several nanometers to several hundreds of micrometers by changing the anodization conditions such as applied potential, preferred electrolyte, and time [18-20]. The polymer templates are produced by irradiation of heavy ions followed by chemical etching. Although the pores on the membrane are usually non-homogeneously distributed across the surface, the polymer templates are chemically more stable such as strong acidic and alkaline solutions as compared to AAO templates [21]. Moreover, they can be readily dissolved in dichloromethane or chloroform.

Kawai et al. examined the magnetic behavior of nanowires of Co and Co-Ni alloys [22] as well as pure Fe [23] electrodeposited using AAO templates. Martin et al. [24] synthesized polymeric and metallic nanotubes into polymer templates with a great number of randomly distributed pores. Whitney et al. [25] studied the fabrication of Ni and Co nanowire arrays into the polymer templates with nanopores. Reports regarding the fabrication of metallic nanowires showed that many metallic nanostructures like Fe, [17, 26-29] Au, [30-32] Co, [27, 33, 34] Ni, [33, 35, 36] Ag [37] and Cu [38] have been successfully prepared using electrochemical deposition method with the help of the template-assisted approach.

The aim of the work reported in this study was to fabricate and characterize iron nanowires with different diameters into randomly distributed porous PC membranes by electrochemical deposition. Here, PC membranes with four different pore diameters, ranging from 125 to 800 nm, were used. Having a different diameter metallic nanowires will enable the study of the size effect dependence of electrical and mechanical properties and allow a better understanding of the microstructure of metallic nanowires important for deformation mechanisms and mechanical properties.

MATERIALS AND EXPERIMENTAL PROCEDURES

Materials Used

PC templates with randomly distributed nanopores were procured from Millipore UK. The specifications of the PC templates are listed in Table 1. One side of the template was sputter-coated with gold-palladium (Au-Pd) using a Gatan 682 Precision Sputter Coating System for 1 minute to make them electrically conductive for a subsequent electrodeposition process (a few nanometers thick).

This coating layer also provided a stable substrate for the growth of the wires. Pieces in sizes of 0.5 cm square were cut from the template sheets and the coated side was placed on a copper metal sheet (3 cm × 5 cm). The area of the PC-templates was measured with a caliper to determine the size of the exposure area. Special care was taken to paint with lacquer around the template to hold it in place and avoid metal deposition onto the copper sheet.

Table 2. Box Behnken test design parameters.

Samples	Pore Diameter (nm)*	Porosity (%)*	Thickness (μm)*	Average Pore Diameter (nm)**	Porosity (%)**
Membrane 1	100	4-18	25	125 ± 12	~ 8
Membrane 2	220	5-20	25	250 ± 19	~ 23
Membrane 3	400	10-20	10	430 ± 41	~ 14
Membrane 4	800	5-20	25	800 ± 48	~ 18

* Information from the manufacturer

** Pore diameters measured via ImageJ software

Electrodeposition of Iron

Electrodeposition of iron was carried out by a conventional electrochemical three-electrode setup, with a platinum counter electrode, a saturated calomel electrode (SCE) as the reference electrode, and the working electrode which was the PC template placed onto a copper sheet. The electrodeposition of iron was performed at a constant voltage of -900 mV and ambient temperature in 1 M iron (II) sulfate heptahydrate (FeSO₄·7H₂O, Fisher Scientific, UK) solution with a pH value of 2.4 ± 0.2. A potentiostat method was utilized using the Gill AC instrument (ACM instruments). The electrodeposition time was altered between 30 to 90 minutes depending on the area of the PC template placed on the copper sheet, porosity percentage of the templates and template thickness. After electrodeposition, all specimens were rinsed with distilled water and ethanol and then dried using hot air. Then, the PC template was removed from the copper substrate and placed into a small tubular container (2 ml) to liberate the wires from the template. The PC template was dissolved in dichloromethane (CH₂Cl₂, Merck) with repeated changes of fresh solvent to separate the wires completely from the polymer. Then the small container filled with dichloromethane was sonicated in an ultrasonic bath for approximately half an hour to obtain individual nanowires for subsequent TEM characterizations.

Characterization Studies

The microstructure of the iron nanowires and surface of the templates were characterized via high-resolution SEM and TEM. A PHILIPS XL30 SEM (FEI, Eindhoven, The Netherlands) was used for the analysis of the surface morphology and geometry of the templates and the wires.

ImageJ software was used to measure the average pore diameter and dimensions of the nanowires from 25 SEM images with different magnifications. TEM was employed to obtain crystallographic information of the fabricated wires using the 200 kV PHILIPS CM20 analytical TEM (FEL, Eindhoven, Netherlands). For this, individual iron nanowires were prepared by dispersing the suspension containing the wires on a carbon mesh TEM grid using an airbrush. Diffraction data were acquired to identify the crystal structure of the iron nanowires, and bright field (BF) images were collected for obtaining structural information. Only nanowires with a maximum thickness of 115 nm were examined due to the limitation of electron transparency. Post-processing of diffraction pattern data was performed in Gatan microscopy software. The distance between the rings in the diffraction pattern was measured using the line profile method by adjusting the endpoints of a line. While indexing the diffraction pattern, the ratios of the diameters of the first five rings were measured. The ratios of the diameters of the rings enable to identify the crystal structure of the nanowire.

RESULTS AND DISCUSSION

The SEM images in Fig. 1 show the surface of the PC templates. The PC templates had a porosity of less than 25% and the nanopores were randomly distributed in the templates. Apart from the suppliers' data, the average pore diameters of the membranes were calculated as 125 ± 12 nm, 250 ± 19 nm, 430 ± 41 nm, and 800 ± 48 nm for membrane 1, 2, 3 and 4, respectively (shown in Table 1). These pore diameters represent the diameter of the final product. The porosity percentages for the membranes were ranging from 8 to 24%.

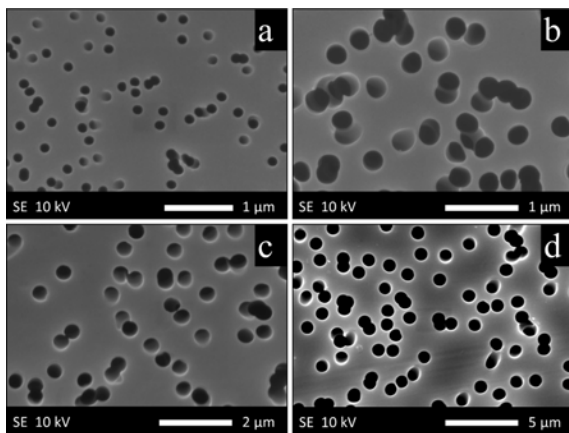


Figure 1. Top-view SEM images of the PC templates with average diameters of: (a) 125 ± 12 nm (b) 250 ± 19 nm (c) 430 ± 41 nm (d) 800 ± 48 nm

Fig. 2 (a-d) shows the SEM images of liberated iron nanowire forests with average diameters ranging between 125 and 800 nm. The SEM images of free-standing nanowire

forests indicate that the electrodeposition of iron in the pores was homogeneous. The final shape and morphology of the nanowires usually depend on electrodeposition conditions [39, 40]. While the length of the nanowire forest can be controlled by the deposition time, the diameters of the wires cannot be changed because of the inherent nature of the PC template [21, 39-41]. The forest, with a nanowire lengths up to 25 μ m, was prepared. The average lengths of the fabricated iron nanowire forests were approximately 25, 8, 5 and 10 μ m for the membranes 1, 2, 3 and 4, respectively. The SEM images in Fig. 2 (a-d) show that the nano-channels are not in parallel alignment indicating some variations of the final length of the wires. The PC membranes, as presented in this work, provide suitable templates for basic research and applications where a high degree of parallelism is not of importance, as well as for the size effect studies on magnetic, electrical and mechanical properties.

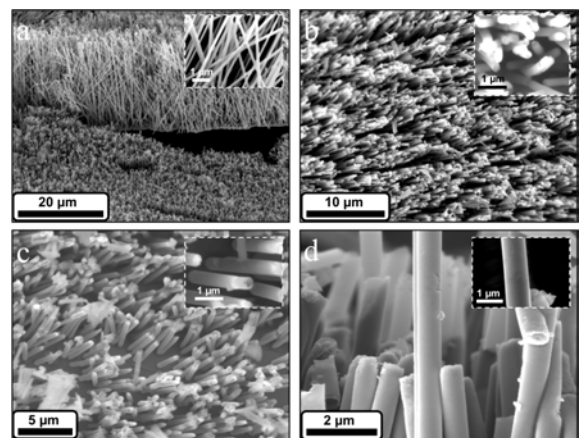


Figure 2. Representative SEM images of liberated iron nanowires with average diameters: (a) 125 ± 12 nm (b) 250 ± 19 nm (c) 430 ± 41 nm (d) 800 ± 48 nm. Insets show the higher magnification of the nanowires.

TEM investigations of an individual iron nanowire with a diameter of approximately 115 nm is summarised in Fig 3 (a). The diffraction pattern in Fig. 3 (b) confirmed the crystal structure as body-centered cubic (bcc) and the wires to be polycrystalline. Single-crystal nanowires are achieved at higher temperatures and lower voltages, which possess homogeneous and smooth surfaces. The voltages used in the experiments are quite high and temperatures low (room temperature) compared to a previously reported study in the literature [38]. Altering the electrodeposition conditions such as temperature and voltage might produce single crystal iron nanowires with smooth surfaces. The diameter of the nanowires could be decreased under 80 nm to obtain a single crystal nanowire by electrodeposition [30]. The results indicated that polycrystalline iron nanowires with four different diameters are promising candidates for the investigation of size effects of their optical, electrical, magnetic and mechanical behaviors and evaluating their potential applications.

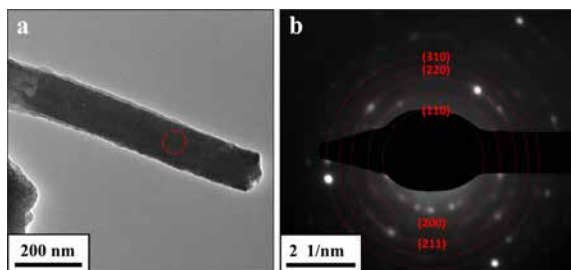


Figure 3. (a) Bright-field TEM image showing an iron nanowire (115 nm in diameter) used for diffraction pattern studies with the area marked with a dashed circle indicating where the diffraction pattern was taken. (b) A typical diffraction pattern of one iron nanowire; the rings are indexed.

CONCLUSION


An effective template-assisted approach has been presented to fabricate polycrystalline iron nanowires with diameters of 125 to 800 nm and length of 25 μm in an iron sulfate ($\text{FeSO}_4 \cdot 7\text{H}_2\text{O}$, at room temperature) solution by electrodeposition into PC templates with randomly distributed pores. The SEM results showed that the forests of iron nanowires ranging from approximately 125 to 800 nm in diameter can be successfully manufactured. The diameters of the fabricated iron nanowires are similar to the nominal diameter of the pores. The nanowires with a length of up to 25 μm could be fabricated by controlling the deposition time. Furthermore, the final shape of the metallic wires directly reflects the shape of the pores in the PC template. Finally, the TEM studies revealed that iron nanowire with a diameter of 115 nm was found to be polycrystalline and the reflection of the diffraction pattern matches with bcc structure type.

References

1. Stelmashenko N, Walls M, Brown L, and Milman YV. Microindentations on W and Mo oriented single crystals: an STM study. *Acta Metallurgica et Materialia*. 41 (1993) 2855–2865.
2. Uchic MD, Dimiduk DM, Florando JN, and Nix WD. Sample dimensions influence strength and crystal plasticity. *Science*. 305 (2004) 986–989.
3. Dimiduk D, Uchic M, and Parthasarathy T. Size-affected single-slip behavior of pure nickel microcrystals. *Acta Materialia*. 53 (2005) 4065–4077.
4. Greer JR, Oliver WC, and Nix WD. Size dependence of mechanical properties of gold at the micron scale in the absence of strain gradients. *Acta Materialia*. 53 (2005) 1821–1830.
5. Kiener D, Motz C, Schöberl T, Jenko M, and Dehm G. Determination of mechanical properties of copper at the micron scale. *Advanced Engineering Materials*. 8 (2006) 1119–1125.
6. Ng K and Ngan A. Stochastic nature of plasticity of aluminum micro-pillars. *Acta Materialia*. 56 (2008) 1712–1720.
7. Greer JR and De Hosson JTM. Plasticity in small-sized metallic systems: Intrinsic versus extrinsic size effect. *Progress in Materials Science*. 56 (2011) 654–724.
8. Zhu T, Bushby A, and Dunstan D. Materials mechanical size effects: a review. *Materials Science and Technology*. 23 (2008) 193–209.
9. Duan X, Huang Y, Cui Y, Wang J, and Lieber CM. Indium phosphide nanowires as building blocks for nanoscale electronic and optoelectronic devices. *Nature*. 409 (2001) 66.
10. Krajewski M, Lin WS, Lin HM, Brzozka K, Lewinska S, Nedelko N, Slawska-Waniewska A, Borysiuk J, and Wasik D. Structural and magnetic properties of iron nanowires and iron nanoparticles fabricated through a reduction reaction. *Beilstein journal of nanotechnology*. 6 (2015) 1652–1660.
11. Bahome MC, Jewell LL, Hildebrandt D, Glasser D, and Coville NJ. Fischer-Tropsch synthesis over iron catalysts supported on carbon nanotubes. *Applied Catalysis A: General*. 287 (2005) 60–67.
12. Zhang X, Wen G, Huang S, Dai L, Gao R, and Wang ZL. Magnetic properties of Fe nanoparticles trapped at the tips of the aligned carbon nanotubes. *Journal of Magnetism and Magnetic Materials*. 231 (2001) 9–12.
13. Reddy M, Yu T, Sow C-H, Shen ZX, Lim CT, Subba Rao G, and Chowdari B. Fe_2O_3 nanoflakes as an anode material for Li ion batteries. *Advanced Functional Materials*. 17 (2007) 2792–2799.
14. Jung G-Y, Johnston-Halperin E, Wu W, Yu Z, Wang S-Y, Tong WM, Li Z, Green JE, Sheriff BA, and Boukai A. Circuit fabrication at 17 nm half-pitch by nanoimprint lithography. *Nano Letters*. 6 (2006) 351–354.
15. Solak HH, Ekinci Y, Käser P, and Park S. Photon-beam lithography reaches 12.5 nm half-pitch resolution. *Journal of Vacuum Science & Technology B: Microelectronics and Nanometer Structures Processing, Measurement, and Phenomena*. 25 (2007) 91–95.
16. Martin CR. Nanomaterials: a membrane-based synthetic approach. *Science*. 266 (1994) 1961–1966.
17. Borissov D, Isik-Uppenkamp S, and Rohwerder M. Fabrication of iron nanowire arrays by electrodeposition into porous alumina. *The Journal of Physical Chemistry C*. 113 (2009) 3133–3138.
18. Masuda H and Fukuda K. Ordered metal nanohole arrays made by a two-step replication of honeycomb structures of anodic alumina. *Science*. 268 (1995) 1466–1468.
19. Li A, Müller F, Birner A, Nielsch K, and Gösele U. Hexagonal pore arrays with a 50–420 nm interpore distance formed by self-organization in anodic alumina. *Journal of Applied Physics*. 84 (1998) 6023–6026.
20. Nielsch K, Choi J, Schwirn K, Wehrspohn RB, and Gösele U. Self-ordering regimes of porous alumina: the 10 porosity rule. *Nano letters*. 2 (2002) 677–680.
21. Ulbricht M. Advanced functional polymer membranes. *Polymer*. 47 (2006) 2217–2262.
22. Kawai S and Ueda R. Magnetic properties of anodic oxide coatings on aluminum containing electrodeposited Co and Co Ni. *Journal of the Electrochemical Society*. 122 (1975) 32–36.
23. Tsuya N, Tokushima T, Shiraki M, Wakui Y, Saito Y, Nakamura H, Hayano S, Furugori A, and Tanaka M. Alumite disc using anodic oxidation. *IEEE Transactions on Magnetics*. 22 (1986) 1140–1145.
24. Martin CR, Parthasarathy R, and Menon V. Template

- synthesis of electronically conductive polymers—A new route for achieving higher electronic conductivities. *Synthetic Metals*. 55 (1993) 1165–1170.
25. Whitney T, Searson P, Jiang J, and Chien C. Fabrication and magnetic properties of arrays of metallic nanowires. *Science*. 261 (1993) 1316–1319.
 26. AlMawlawi D, Coombs N, and Moskovits M. Magnetic properties of Fe deposited into anodic aluminum oxide pores as a function of particle size. *Journal of applied physics*. 70 (1991) 4421–4425.
 27. Tourillon G, Pontonnier L, Levy J, and Langlais V. Electrochemically synthesized Co and Fe nanowires and nanotubes. *Electrochemical and Solid-State Letters*. 3 (2000) 20–23.
 28. Baik JM, Schierhorn M, and Moskovits M. Fe nanowires in nanoporous alumina: Geometric effect versus influence of pore walls. *The Journal of Physical Chemistry C*. 112 (2008) 2252–2255.
 29. Friedman AL and Menon L. Optimal Parameters for Synthesis of Magnetic Nanowires in Porous Alumina Templates Electrodeposition Study. *Journal of the Electrochemical Society*. 154 (2007) E68–E70.
 30. Dou R and Derby B. The strength of gold nanowire forests. *Scripta materialia*. 59 (2008) 151–154.
 31. Benfield RE, Grandjean D, Kröll M, Pugin R, Sawitowski T, and Schmid G. Structure and bonding of gold metal clusters, colloids, and nanowires studied by EXAFS, XANES, and WAXS. *The Journal of Physical Chemistry B*. 105 (2001) 1961–1970.
 32. Forrer P, Schlottig F, Siegenthaler H, and Textor M. Electrochemical preparation and surface properties of gold nanowire arrays formed by the template technique. *Journal of Applied Electrochemistry*. 30 (2000) 533–541.
 33. Daub M, Knez M, Goesele U, and Nielsch K. Ferromagnetic nanotubes by atomic layer deposition in anodic alumina membranes. *Journal of applied physics*. 101 (2007) 09J111.
 34. Metzger RM, Konovalov VV, Sun M, Xu T, Zangari G, Xu B, Benakli M, and Doyle W. Magnetic nanowires in hexagonally ordered pores of alumina. *IEEE Transactions on Magnetics*. 36 (2000) 30–35.
 35. Nielsch K, Müller F, Li AP, and Gösele U. Uniform nickel deposition into ordered alumina pores by pulsed electrodeposition. *Advanced Materials*. 12 (2000) 582–586.
 36. Zeng H, Skomski R, Menon L, Liu Y, Bandyopadhyay S, and Sellmyer DJ. Structure and magnetic properties of ferromagnetic nanowires in self-assembled arrays. *Physical Review B*. 65 (2002) 134426.
 37. Sauer G, Brehm G, Schneider S, Nielsch K, Wehrspohn R, Choi J, Hofmeister H, and Gösele U. Highly ordered monocrystalline silver nanowire arrays. *Journal of Applied Physics*. 91 (2002) 3243–3247.
 38. Molares MT, Brötz J, Buschmann V, Dobrev D, Neumann R, Scholz R, Schuchert I, Trautmann C, and Vetter J. Etched heavy ion tracks in polycarbonate as template for copper nanowires. *Nuclear Instruments and Methods in Physics Research Section B: Beam Interactions with Materials and Atoms*. 185 (2001) 192–197.
 39. Schönenberger C, van der Zande BMI, Fokkink LGJ, Henny M, Schmid C, Krüger M, Bachtold A, Huber R, Birk H, and Staufer U. Template Synthesis of Nanowires in Porous Polycarbonate Membranes: Electrochemistry and Morphology. *The Journal of Physical Chemistry B*. 101 (1997) 5497–5505.
 40. Liu Z, Abedin SZE, Ghazvini MS, and Endres F. Electrochemical synthesis of vertically aligned zinc nanowires using track-etched polycarbonate membranes as templates. *Physical Chemistry Chemical Physics*. 15 (2013) 11362–11367.
 41. Batista EA, dos Santos DP, Andrade GF, Sant'Ana AC, Brolo AG, and Temperini ML. Using polycarbonate membranes as templates for the preparation of Au nanostructures for surface-enhanced Raman scattering. *Journal of nanoscience and nanotechnology*. 9 (2009) 3233–3238.

The Preventive Effect of Thymoquinone and Ceratonia Siliqua L. in Experimental Asthmatic Pregnant Rats: Histologically and Immunohistochemically Evaluation

Ameerah Fadhil Ahmed, Sule Coskun Cevher 
Gazi University, Department of Biology, Ankara, Turkey

ABSTRACT

There are no studies yet have been compared pregnant rat asthma models by assessing the airway both histologically and immunohistochemically under the effect of Thymoquinone (TQ) and Ceratonia siliqua (CS) (Carob). To compare asthmatic pregnant models with TQ and CS by studying changes of both the histologically and the immunohistochemically of lung tissue using light microscopy. 18 female wistar rats were randomly split to 3 groups: asthmatic pregnant group (I) sensitized by intraperitoneal ovalbumin injection (OVA) with alum on days 0 and 14 and submitted to OVA aerosolized 3 days in excess of the next 1 week then they coupled with male rats to get pregnancy; asthmatic pregnant with TQ and CS group (II) sensitized as above then they administered each of TQ and CS on the last 5 days of pregnancy; and asthmatic pregnant with dexamethasone group (III) that received dexamethasone by intraperitoneal injection on last 5 days of pregnancy. Lung tissue immunohistochemically and histologically were evaluated. Various histological changes in lung tissues of group I were revealed. However, treatment of TQ and CS was prevented these changes in group II. Immunohistochemically, vascular endothelial growth factor (VEGF) staining levels increase was observed in group I, while there was a significant decrease in group II than it is in group III. In this study, the use of TQ and CS has been shown to alleviate the histological changes and immunohistochemically caused by asthma. In conclusion, TQ and CS was thought to be a promising treatment agent for asthma in the future especially during pregnancy. The use of TQ and CS in people with normal asthma may be used as a new promising supplement to eliminate the negative effects of asthma.

Keywords:

Rats; Asthma; Remodeling; VEGF; Nebulized ovalbumin; Thymoquinone; *Ceratonia siliqua*.

INTRODUCTION

Asthma is one of the farthest extensive obstinate diseases in the world and it is approximate that out of 300 million of the world's population is suffering from asthma [1]. Asthma is a chronic inflammatory illness that define with airway hyperresponsiveness and reversible airflow restriction [2]. Sensitization to antigens is thought to be a obligatory for starting the inflammatory series in asthma attack, and constant exposure to allergen occasion inflammation of the airway mucosa and submucosa, coordinate by type 2 helper T (TH2) cells [3]. Asthma animal models have spotlight the significance of TH2-driven allergic reaction in the evolution of asthma [4]. In asthma textural changes known as airway remodeling may causing by permanent inflammation [5]. Smooth muscle hypertrophy, goblet cell

hyperplasia, subepithelial fibrosis and angiogenesis are included of respiratory remodeling [6]. At the same time, bronchial epithelium damage is observed as a result of hyperactivity of the bronchi. Epithelial damage is caused by eosinophil infiltration followed by degradation of eosinophils and release of toxic granular proteins [7, 8]. As a result of the development of edema simultaneously with the cellular and molecular changes observed in the respiratory tract, episodic dyspnoea (shortness of breath) occurs as a result of narrowing of the bronchi with mucosal edema typical of asthma. Strong anti-inflammatory drugs, such as inhaled corticosteroids and anti-leukotrienes, are the basis for the treatment of asthma symptoms in the long term [9]. In spite of these drugs are efficient, also they have side effects. Thus in collateral with

Article History:

Received: 2019/06/16

Accepted: 2019/07/30

Online: 2019/09/30

Correspondence to: Ameerah Fadhil

Ahmed Ahmed,

Gazi University, Biology, 06500, Ankara,

TURKEY

E-Mail: emire.ahmed80@gmail.com

current medicines, scientists are in work with classic or popular medicines. *Nigella sativa* L. is one of these medicines, has become apply as classic therapy of asthma and other inflammatory diseases. Both in vitro and in vivo models, Thymoquinone (TQ) active component of *N. sativa* has been searched for its anti-oxidant, anti-inflammatory and anticancer properties [10]. An inflammatory change combined with asthma is preventing by the strong inhibitor TQ [11]. It is forbids T helper 2 (Th2) cytokines, eosinophil infiltration and reduces allergic airway inflammation; this proof indicates its prospective anti-inflammatory role along the allergic reaction in the lung. In spite of these, few are known about the agent and mechanisms principal underlying these all effects [12]. The formation of 5-hydroxyeicosatetraenoic acid, as well as 5-lipoxygenase, inhibits by TQ [13].

Also for the time being, *Ceratonia siliqua* L. CS (carob) it have been interest and has played an important economic role for its used as food contribution as well as in the pharmaceutical and cosmetic industries [14]. Carob seeds are in particular substantial fount of compound polymers of flavonoids such as proanthocyanidin, ellagitannin and gallotannin. These phytochemicals have been used in medicine because of their pharmacological advantages over many diseases and have free radical scavenging actions [15]. It was discovered that the carob fruit contains 24 different phenolic compounds as well as the most commonly found is gallic acid [16]. Carob powder is a precious reference of vitamins E, D, C, Niacin, B6, and folic acid; vitamins A, B2, and B12 are provided in fewer levels. And it is oil constitute of 17 fatty acids, mainly oleic, linoleic, palmitic, and stearic acid respectively at 40.45%, 23.19%, 11.01%, and 3.08% [17]. A source of bioactive ingredient found in carob fruit is called D-Pinitol, that it can be carry out by a few methods like supercritical fluids and using ion exchange resins [18, 19]. The relationship between d-pinitol and diabetes is an important subject for worldwide and there are different investigations about this subject [20, 21].

Oxidative stress OS and nitrosative stress NS are the injurious efficacy of free radicals causing possible biological harms [22, 23, 24]. To forbidding damaging effects against OS, cells have many preventive mechanisms called antioxidant defense system [25]. A large number of medicinal and racy plants, as well as fruits and leaves of some berry herbs, biosynthesis phytochemicals have antioxidant effects and may be used as a native origin of free radical scavenging compounds was show off by a lot of studies [26].

Natural products have an increasing interest in foodstuffs because of the potential negatory efficacy of artificial nutrition additions on human healthiness as well as in last years the increase of customer sensation. As far as it can be

determined by our literature research until now no studies have been declared on the antioxidant capacity and antiasthmatic role of the CS combined with TQ supplement used in this study especially its effect on asthmatic pregnant.

The objective of this research was to identify the effectiveness of TQ and CS co-administration on lung tissue in the pregnant rats with asthma as histologically and immunohistochemically.

MATERIALS AND METHODS

Experimental Animals and Ethical Approval

Wistar albino 18 female rats with range of weight 200–250 g were provided from the GU Laboratory Animal Breeding and Experimental Research Center (GUDAM, Ankara, Turkey), and were hold in three groups, every group having six rats. The animals were hold at $20 \pm 2^\circ\text{C}$ with 12:12 h adverse, light/dark period and dedicated free entrance to usual laboratory food for rodent with water in stainless birdcages, and be given humane maintenance accordingly to the scale outlined in the Guide for the Care and Use of Laboratory Animals. This study was certified by Ethics Committee of the Science Faculty of Gazi University (Code No: G. U. ET-16. 035).

Experimental Design

The rats were at random disunited into three groups every having six rats. Group I (asthmatic pregnant): they were induced to asthma by OVA. Group II (asthmatic pregnant with TQ and CS treated): the asthmatic rats received 10mg/kg/day each of TQ and CS once a day during last 5 days of pregnancy. Group III (Asthmatic pregnant with Dexamethasone treated): the rats received 1mg/kg/day Dexamethasone [27] once a day during last 5 days of pregnancy.

TQ was dissolved in normal saline (PF %0, 9 isotonic) 10mg/kg [28] using water bath kept at 60°C and the solution was prepared fresh just before gavage administration. CS was dissolved in normal saline (PF %0, 9 isotonic) at room temperature.

Sensitization and Inhalational Exposure

Groups of OVA were sensitized to ovalbumin (grade V, ref. A5503-1G, Sigma Aldrich), in accordance with the procedures of Moura et al. [29] and Yang et al. [30]. They were effective sensitized by intraperitoneally injections (i.p.) of OVA (1mg/mL saline) with alum (1mg/mL normal saline) (Reagent grade, 239186-25G, Sigma Aldrich) that an adjuvant on days 0 and 14. Rats were challenged

for 30 min with inhalation of OVA by a nebulizer (Handyneb, SN. NGM 769576) coupled to a plastic box on the days 21, 22 and 23. After the last inhalation of OVA rats were coupled with male rats (1 male each of 3 females). After proving rat's pregnancy by the veterinarian (between 11-13 pregnant days), they were attacked of asthma by a second doses of OVA (5mg/mL) inhalation for 3 days. Then in last 5 days of pregnancy rats in group II were received mix of TQ (274666-5G, Sigma Aldrich) and SC (Carob powder from herbalist) solutions by intragastric gavage and rats in group III were received dexamethasone doses by i.p injection.

Histological Study

All rats were anaesthetized by an injection of ketamine (40 mg/kg) and xylazine (2 mg/kg) intramuscularly. After death of all animals lung samples were dissected immediately, well washed with saline and in 10% neutral-buffered formalin were fixed for 72 h at least. For half an hour all the samples were washed in tap water, in ascending grades of alcohol (absolute 70% - 90% - 95%) were dehydrated, cleared in xylene and then in paraffin wax were embedded . For light microscopic examination, serial sections of 6 µm thick were cut and stained with hematoxylin and eosin (H&E). In many days later the sections were viewed and photographed by Olympus BX51 microscope (Olympus Optical Co. Ltd, Tokyo, Japan) [31].

Immunohistochemically Method

An avidin-biotin-complex (ABC) for formalin-fixed paraffin-embedded tissues immunohistochemical staining method was used [32]. From each paraffin block, successive sections of 5 µm of tissue were cut, then on glass slides prepared and desiccated. In xylene, tissues were deparaffinized then in graded alcohol solutions rehydrated. For blocking the action of endogenous peroxidase, 3% hydrogen peroxide in pure methanol was used for 20 min at room temperature. In a microwave the tissues were vaporized for 10 min using 0.01 M sodium citrate solution at pH 6.8 for retrieve the antigen. For 10 min at room temperature, Non-specific protein linking was saturated

using 4% horse serum (Invitrogen, Burlington, Ontario) in phosphate buffered saline (PBS). By application the diluted primer VEGF to tissue segments, the slides incubated 1 hour in room temperature. In accordance with the manufacturer's directions (Vector Laboratories; Vecastain Elite ABC kit) reagent (ABC) was made and applied for 30 min in room temperature. Coloration improved by applying diaminobenzinetetrahydrochloride (DAB) reagent (Sigma Aldrich) for 10 min. For counterstained the tissues, hematoxylin were applied, then in graded alcohol dehydrated and affixed with cover glass. Semi quantitative method was used. 0: no staining, 1: low staining, 2: moderate staining, 3: severe staining.

Statistical Analysis

Submits of data was performed by means (SD) and ranges (minimum-maximum) between-group comparisons were made using Tukey. A statistically significant was counted by value of P <0.05 and these statistical analysis was made by using version 11 of the SPSS software package (SPSS Inc, USA).

RESULT AND DISCUSSION

Histological Results of Lung Tissues

When the general histological structure of the groups was evaluated, group I increased inflammatory cell and eosinophils infiltration around the bronchi and bronchiole walls, increased subepithelial smooth muscle thickness and epithelial cell lengths was noticed. In group II decreased inflammatory cell infiltration, subepithelial smooth muscle and epithelial cell lengths were normal. The administration of dexamethasone revealed a very mild regulation in all of the histological finding associated with asthma (Fig. 1: A, B and C) (Table1).

Di Cosmo et al [33] showed that OVA treatment of animals significantly participated in the bronchial constriction and damage of lung tissue. Wills-Karp et al [34] were noticed that OVA sensitization of animals led to significant in-

Table 1. H & E histological semiquantitative evaluation in lung tissue.

Groups	Inflammatory cell and eosinophils infiltration around the bronchi and bronchiole walls	Subepithelial smooth muscle thickness	Epithelial cell lengths
Asthmatic Pregnant (I)	+++*	+++*	+++*
Asthmatic Pregnant with TQ & CS(II)	+++	+++	+++
Asthmatic Pregnant with Dexamethasone(III)	++**	++**	++**

*: Significant increase, **: Significant decrease.
P < 0.05

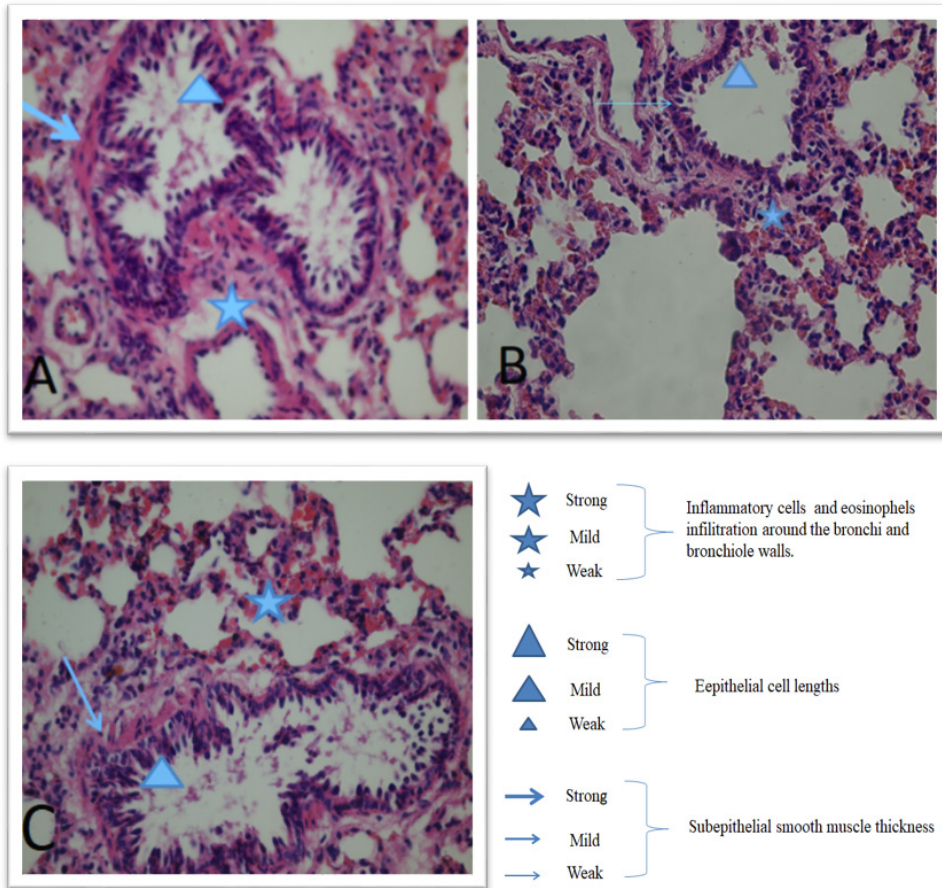


Figure 1. (A) Lung sections of asthmatic pregnant rat. Increased inflammatory cell and eosinophils infiltration around the bronchi and bronchiole walls (★), subepithelial smooth muscle thickness (→) and epithelial cell lengths (▲) X40, H&E. (B) Lung sections of asthmatic pregnant rat with TQ and CS. Inflammatory cell infiltration (★), subepithelial smooth muscle thickness (→) and epithelial cell lengths (▲) were normal. X40, H&E. (C) Lung sections of asthmatic pregnant rat with Dexamethasone. Very mild regulation in all of the histological finding associated with asthma (★, →, ▲) X40, H&E.

filtration of inflammatory cells into the lung as observed by bronchoalveolar lavage and histological examination. In the study of Serap CM et al [35] inflammatory cell infiltration and epithelial damage were observed in the lung tissues of asthmatic mice.

Similar findings were found in our study in accordance with the above studies. The above mentioned studies support our work. In present study OVA – induced asthma in group I was significantly increased the inflammatory cell and eosinophils infiltration around the bronchi and bronchiole walls, increased subepithelial smooth muscle thickness and epithelial cell lengths ($p < 0.05$). In group II the histological changes in group I were significantly decreased ($p < 0.05$). This study is quite remarkable in that it is the first study showing the effects of the combined use of TQ and CS on pregnant rats. However, only use of TQ has been shown similar results in the lungs of asthmatic mice [35, 36]; to date, there is no study showed the effective role of carob in the alleviation or treatment of asthma.

In III group the use of dexamethasone as a treatment of asthma was significant decreased the inflammatory cell and eosinophils infiltration around the bronchi and bronchiole walls, subepithelial smooth muscle thickness and epithelial cell lengths in the lung tissues of rats ($p < 0.05$) however, dexamethasone's effect was less than it is in group II. Dex from glucocorticoids is frequently used in models of allergic asthma as standard reference [37]. Glucocorticoids extremely block T cell pro-inflammatory cytokine manufacture and that's why decrease infiltration of inflammatory granulocytes as eosinophils [38, 39].

Our results show similar findings with the results of the above-mentioned investigators, and the co-administration of TQ and CS contributed to healing by reducing the signs of inflammation associated with asthma.

VEGF Immunohistochemistry

The immunohistochemically finding was significantly increased in subendothelial VEGF in group I when com-

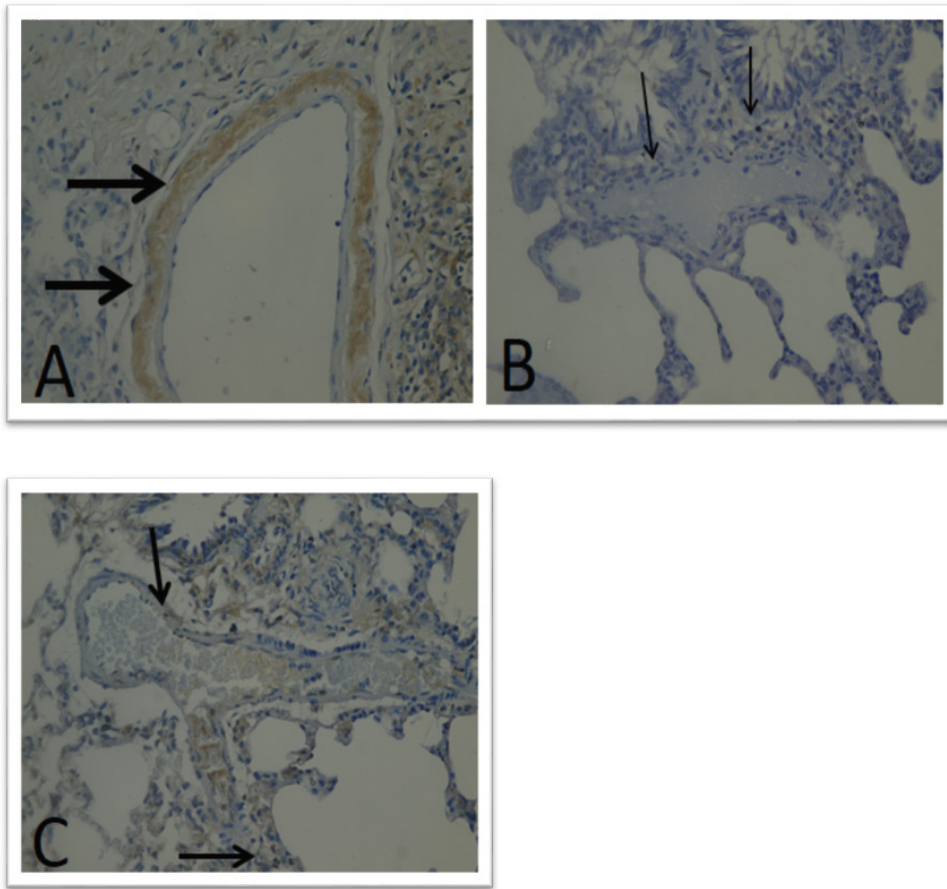


Figure 2. (A) Lung sections of asthmatic pregnant rat. VEGF positive stained, showing increased. Subendothelial VEGF levels (→) X40, VEGF Immunohistochemical staining. (B) Lung sections of asthmatic pregnant rat with TQ and CS. Subendothelial VEGF levels significantly decreased (→) X40, VEGF Immunohistochemical staining. (C) Lung sections of asthmatic pregnant rat with Dexamethasone. Subendothelial VEGF levels was decreased (→) X40, VEGF Immunohistochemical staining.

pared to both of group II and group III ($p < 0.05$). In group II subendothelial VEGF was significantly decreased when compared to I and dexamethasone group ($p < 0.05$). When compared to group II and Group III, decreased subendothelial VEGF level found in the co-administration of TQ and CS group (Fig. 2) (Table 2). This finding indicated that co-administration of TQ and CS decreased subendothelial VEGF level that plays a key role in angiogenesis.

Asthma develops as a result of chronic inflammation and remodeling in the respiratory tract [40]. Findings such as increased vascularity and increased number of blood vessels in submucosal patients have raised this question. The increase in the number of vessels is mainly due to factors

related to endothelial cell proliferation [41]. Angiogenesis occurs due to the differentiation and proliferation of endothelial cells and vascular permeability and VEGF plays a key role in the process of asthma [42].

Serap CM et al observed that submucosal immunopositive vessels in chronic asthma group increased significantly [35]. Enhancement in vascular format, number and exterior space and ultra-structure of VEGF and VEGF receptors is great certified in asthma airway [41, 43, 44, 45, 46]. In our study, the subendothelial VEGF level was significantly increased in asthma group ($p < 0.05$). The result of Serap CM et al [35] confirms our result of asthma group increasing angiogenesis.

Table 2. Immunohistochemistry of subendothelial VEGF in lung tissue.

Groups	Asthmatic pregnant (I)	Asthmatic pregnant with TQ&CS (II)	Asthmatic pregnant with Dexamethasone (III)
Subendothelial VEGF	+++*	+++	+++*

+: Significant increase, **: Significant decrease.
 $P < 0.05$

Serap CM et al demonstrated that the application of TQ alone in asthmatic mice decreased submucosal VEGF and epithelial VEGF [35]. This finding was similar to our result. Subendothelial VEGF was significantly decreased ($p < 0.05$) in group II. In our study, the co-administration of TQ and CS together in the lungs of asthmatic pregnant rats was alleviated or treated the damages caused by OVA.

Although TQ has been reported to reduced asthma symptoms and inflammatory markers, there is no literature on the effect of TQ and CS on concomitant use of asthma. Respiratory response in asthma is in the form of Ig E-mediated, mast cell degranulation and histamine and leukotriene mediators. These effects in TQ show anti-inflammatory effects by inhibiting the production of leukotriene B₄, thromboxane B₂ and by inhibiting 5-lipoxygenase and cyclooxygenase pathways in arachidonic acid metabolism[47]. It has also been shown to have inhibitory effects on histamine receptors[48]. The effect of carob alone in asthmatic lung tissues of animals or patients was not described yet. This is the first report evidence the positive effect of carob and TQ in lung tissues of asthmatic pregnant rats. Preceding works have represented that locust bean juice is opulent in potassium, sodium, calcium, magnesium, iron, copper and manganese, in addition to zinc. In addition, a strong antioxidant element such as gallic acid is the very rich phenolic complex found in carob fruit (3.27 mg /g) and also high tannic acid (10.2 mg/dl) was found [49]. Phenolic compounds and zinc's antioxidant and free radical scavenging activity have previously been informed [50, 51]. In our study it can be said that the decreased in VEGF levels in lung tissue is probably the cumulative effect of antioxidant and free radical scavenger effect of carob and the decreasing angiogenesis effect of TQ.

In III group subendothelial VEGF was significantly decreased ($p < 0.05$) however the effect of dexamethasone was less than it is in co-administration of TQ and CS group. Serap CM et al [35] indicated the use of dexamethasone significantly decreased VEGF immunohistochemically changes but there is no significant between TQ and dexamethasone treated groups when it was investigated in lung tissues of asthmatic mice

Currently, drugs used in the treatment of asthma have limited effects on structural changes. Anti-leukotrienes, theophylline and inhaled corticosteroids used in asthma may be effective in reducing the structural changes in the respiratory system when used for a long time [52]. Thus a new or alternative treatment are needed especially this new treatment has little or no side effect when it will use for long time.

CONCLUSION

In the current study, co-administration of TQ and CS decreased the inflammatory cell and eosinophils infiltration, around the bronchi and bronchiole walls, of lung tissues in asthmatic treated groups compared to dexamethasone group. The results of this study demonstrate that the combined use of TQ and CS may be an total/cumulative effect of TQ's reducing the angiogenesis and the antioxidant effect of carob together. This type of application will contribute to the treatment of asthma and the prevention of attacks especially during pregnancy. At the same time, the use of TQ and CS in people with normal asthma may be used as a new promising supplement to eliminate the negative effects of asthma. Current studies will open wide prospects for the positive role of TQ and CS in alleviating and treating the symptoms of asthma.

ACKNOWLEDGEMENT

We wish to thank projects of scientific investigation (BAP) of Gazi University for their permanent concern and precious counseling in this project. Through a research Grant No. 05/2016-22 from the BAP, this work was partially supported.

References

1. Hansel TT, Barnes PJ. Novel drugs for treating asthma. *Curr Allergy Asthma Rep* 2001;1:164-73.
2. Tagaya E, Tamaoki J. Mechanisms of airway remodeling in asthma. *Allergol Int.* 2007;56:331-40.
3. Herz U, Renz H, Wiedermann U. Animal models of type I allergy using recombinant allergens. *Methods.* 2004 ;32:271-80.
4. Zosky GR, Sly PD. Animal models of asthma. *Clin Exp Allergy.* 2007;37:973-88.
5. Ramos-Barbón D, Ludwig MS, Martin JG. Airway remodeling: lessons from animal models. *Clin Rev Allergy Immunol.* 2004;27:3-21.
6. Arm JP, Lee TH. The pathobiology of bronchial asthma. *Adv Immunol* 1992; 51:323-82.
7. Gleich GJ, Adolphson CR. The eosinophilic leukocyte: structure and function. *Adv Immunol* 1986; 39:177-253.
8. Sumi Y, Hamid Q. Airway remodeling in asthma. *Allergol Int* 2007;56:341-8.
9. Atta-ur-Rahman, Malik S, Ahmed S, Choudhary MI, Habib-ur-Rehman. Nigellimine-N-oxide A new isoquinoline alkaloid from the seeds of *Nigella sativa*. *Heterocycles* 1985; 23:953-5.
10. Woo CC, Kumar AP, Sethi G, Tan KH. Thymoquinone: Potential Cure for Inflammatory Disorders and Cancer. *Biochem Pharmacol* 2012; 83: 443-51.
11. Ammar el SM, Gameil NM, Shawky NM, Nader MA. Comparative evaluation of anti-inflammatory properties of thymoquinone and curcumin using an asthmatic murine model. *Int Immunopharmacol*

- 2011; 11: 2232-6.
12. El Gazzar M, El Mezayen R, Marecki JC, Nicolls MR, Canastar A, Dreskin SC. Anti-inflammatory effect of thymoquinone in a mouse model of allergic lung inflammation. *Int Immunopharmacol* 2006; 6: 1135-42.
 13. Al-Gahmadi MS. The anti-inflammatory, analgesic and antipyretic activity of *Nigella sativa*. *J Ethnopharmacol* 2001;76:45-8.
 14. Sidina MM., El Hansali M, Wahid N, Ouattmane A, Boulli A, Haddioui A. Fruit and seed diversity of domesticated carob (*Ceratonia siliqua* L.) in Morocco. *Scientia Horticulturae*. 2009; 123: 110-116.
 15. Luthria D. Significance of sample preparation in developing analytical methodologies for accurate estimation of bioactive compounds in functional foods. *Journal of the Science of Food and Agriculture* 2006; 86: 2266-2272.
 16. Anonim. Ulusal Gıda Kompozisyon Veri Tabanı. 2017; www.turkomp.gov.tr/food/376 (Access Date: 11.07. 2017).
 17. Youssef, M. K. E., El-Manfaloty, M. M., & Ali, H. M. Assessment of proximate chemical composition, nutritional status, fatty acid composition and phenolic compounds of carob (*Ceratonia siliqua* L.). *Healthcare Foodservice Magazine*. 2013; 3, 304-308.
 18. Karhan, M., H. Gubbuk, İ. Turhan, H. R. Öziyici, H. Akgül, K. Uçgun. Türkiye’de yetişen keçiyoynuzu (*Ceratonia siliqua* L.) tiplerinin biyoaktif birmoleküllü D-pinitol içeriği üzerine çevre koşulları ve bileşim unsurlarının etkisi. 2010. TÜBİTAK Projesi Proje No: 107O650.
 19. Alper, Y. Keçiyoynuzu (*Ceratonia siliqua* L.) meyvesinden süperkritik karbondioksit (CO₂) ekstraksiyonu ile d-pinitol eldesi. Yüksek lisans tezi. E. Ü. Fen Bilimleri Enstitüsü Gıda Mühendisliği Anabilim Dalı Bornova- İzmir. 2016.
 20. Davis, A., M. Christiansen, J. F. Horowitz, K. M. Hellerstein, and E. R. Ostlund. Effect of pinitol treatment on insulin action in subjects with insulin resistance. *Diabetes Care*. 2000; 23: 1000-1005.
 21. Kim, J.I., Kim, J.C., Kang, M.J., Lee, M.S., Kim, J.J., Cha, I.J. Effects of Pinitol isolated from soybeans on glycemic control and cardiovascular risk factors in Korean patients with type 2 diabetes mellitus: a randomized controlled study. *European Journal of Clinical Nutri*. 2005; 59: 456-458.
 22. Kovacic P, Jacintho JD. Mechanisms of carcinogenesis: Focus on oxidative stress and electron transfer. *Current Medicinal Chemistry* 2001; 8: 773-796.
 23. Valko M, Leibfritz D, Moncol J, Cronin MTD, Mazur M, Telser J. Free Radicals and Antioxidants in Normal Physiological Functions and Human Disease. *The International Journal of Biochemistry & Cell Biology*. 2007; 39: 44-84.
 24. Gulcin I, Beydemir S. Phenolic compounds as antioxidants: carbonic anhydrase isoenzymes inhibitors. *Mini Rev Med Chem* 2013; 13 (3): 408-430.
 25. De Zwart LL, Meerman JHN, Commandeur JNM, Vermeulen NPE. Biomarkers of free radical damage applications in experimental animals and in humans. *Free Radical Biology & Medicine*. 1999; 26: 202-226.
 26. Yu LL, Zhou KK, Parry J. Antioxidant properties of cold pressed black caraway, carrot, cranberry, and hemp seed oils. *Food Chemistry*. 2005; 91: 723-729.
 27. Xie, Q.M., X. Wu, H.M. Wu, Y.M. Deng, S.J. Zhang, J.P. Zhu, X.W. Dong. Oral administration of allergen extracts from *Dermatophagoides farinae* desensitizes specific allergen-induced inflammation and airway hyperresponsiveness in rats. *Int Immunopharmacol*. 2008; 8(12): 1639-1645.
 28. Choi, Y.H., Yan, G.H., Chai, O.H., Lim, J.M., Sung, S.Y., Zhang, X., Kim, J.H., Choi, S.H., Lee, M.S., Han, E.H., Kim, H.T., Song, C.H. Inhibition of anaphylaxis-like reaction and mast cell activation by water extract from the fruiting body of *Phellinus linteus*. *Biol Pharm Bull.*; 2006; 29 (7):1360-1365
 29. Moura CTM, Bezerra FC, Moraes IM, Magalhães PJC, Capaz FR. Increase responsiveness to 5-hydroxytryptamine after antigenic challenge is inhibited by nifedipine and niflumic acid in rat trachea in vitro. *Clin Exp Pharmacol Physiol*. 2005; 32:1119-1123.
 30. Yang EJ, Lee J-S, Song BB, Yun C-Y, Kim D-H, Kim IS. Anti-inflammatory effects of ethanolic extract from *Lagerstroemia indica* on airway inflammation in mice. *J Ethnopharmacol*. 2011; 136:422-427.
 31. Hould R. 1984. Technical on histopathology and cytopathology. Maloine. 19-21:225-227.
 32. Haines DM, Chelack BJ. Technical considerations for developing enzyme immunohistochemical staining procedures on formalin-fixed paraffin-embedded tissues for diagnostic pathology. *J Vet Diagn Invest* 1991;3:101-112.
 33. DiCosmo BF, Geba gp, Picarella D, Elias JA, Ranking JA, Stripp BR, Whetsett JA, Favell RA. Airway epithelial cell expression of interleukin-6 in transgenic mice. Uncooupling of airway inflammation and bronchial hyperreactivity. *J Clin Invest*. 1994; 94:2028-2035. [PubMed: 7962549]
 34. Wills-Karp M, Gavett SH, Schofield B, Finkelman F. Role of interleukin-4 in the development of allergic airway inflammation and airway hyperresponsiveness. *Av Exp Med Biol*. 1995; 409:343-347.
 35. Serap C.M., Serdar K., Tolgahan A., Hüsni A B., Gonca K., Gökçen Ö Ş., Tuncay Ş., Osman Y. The effectiveness of thymoquinone in experimental model of asthma and role of vascular endothelial growth factor. *Smyrna Med.J*. 2013; 3: 34- 39. [https:// ISSN: 2146-670X](https://doi.org/10.21467/ISSN:2146-670X).
 36. S. Kalemci , S. Cilaker Micili , T. Acar , T. Senol , N. Dirican, G. Omeroglu , A. Bagriyanik , G. Kamaci , O. Yilmaz. Effectiveness of thymoquinone in the treatment of experimental asthma. *Clin Ter* 2013; 164 (3):e?????. doi: 10.7417/CT.2013.1559.
 37. Das, A.M., R.J. Flower, P.G. Hellewell, M.M. Teixeira, M. Perretti, 1997. A novel murine model of allergic inflammation to study the effect of dexamethasone on eosinophil recruitment. *Br J Pharmacol.*, 121: 97-104. de Matos, O.G., S.S. Amaral, P.E. Pereira da Silva, D.A. Perez, D.M. Alvarenga, A.V. Ferreira, J.
 38. Abeer A.A. Salama., Hala F. Zaki., Siham M. El-Shenawy., EL-Denshary E.S.M., Ismaiel ElKassaby Ismaiel and Nermeen M. Shaffie. Effects of Fish oil and Dexamethasone in Experimentally-Induced Bronchial Asthma. *Australian J. of Basic and Applied Sciences*, 2012 6(13): 497-506. ISSN 1991-8178.
 39. Corrigan, C. 2012. Mechanisms of asthma. *Medicine.*, 40 (5): 223-227.
 40. Bergeron C, Boulet LP. Structural changes in airway diseases: characteristics, mechanisms, consequences, and pharmacologic modulation. *Chest* 2006;129:106887.
 41. Li X, Wilson JW. Increased vascularity of the bronchial mucosa in mild asthma. *Am J Respir Crit Care Med* 1997;156:229-33.
 42. Arm JP, Lee TH. The pathobiology of bronchial asthma. *Adv Immunol* 1992;51:323-82.
 43. Chun G L., Holger L., Peter B., Robert J H., Svetlana C., Vineet B., Min J K., Lauren C., Yoon K K., Donald M M., and Jack A E. Vascular endothelial growth factor (VEGF) induces remodeling and enhances TH2-mediated sensitization and inflammation in the lung. *Nat Med* . 2004 October ; 10(10): 1095-1103. doi:10.1038/nm1105.
 44. Vrugt B, et al. Bronchial angiogenesis in severe glucocorticoid-dependent asthma. *Eur. Respir. J*. 2000; 15:1014-1021. [PubMed:

- 10885418]
45. Salvato G. Quantitative and morphological analysis of the vascular bed in bronchial biopsy specimens from asthmatic and non-asthmatic subjects. *Thorax*. 2001; 56:902-906. [PubMed: 11713351]
 46. Lee YC, Lee HK. Vascular endothelial growth factor in patients with acute asthma. *J. Allergy Clin. Immunol.* 2001; 107:1106-1108. [PubMed: 11398093]
 47. Houghton PJ, Zerka R, DL-Heras B, Hoult JR. Fixed oil of *Nigella sativa* and derived thymoquinone inhibit eicosanoid generation in leukocytes and membrane lipid peroxidation. *Planta Medica* 1995;61:33-6.
 48. Boskabady MH, Sheiravi N. Inhibitory effect of *Nigella sativa* on histamine receptors of isolated guinea pig tracheal chains. *Pharm Biol* 2002;40:596602.
 49. Ayaz F.A., Torun H., Ayaz S., Correia P.J., Alaiz M., Sanz C., Gruz J., Strand M. Determination of chemical composition of Anatolian carob pod (*Ceratonia siliqua* L.), Sugars, amino and organic acids, minerals and phenolic compounds. *J. Food Quality*. 2007; 30: 1040-1055. <https://doi.org/10.1111/j.1745-4557.2007.00176.x>
 50. Tokeshi I., Yoshimoto T., Muto N., Nakamura S., Ashizawa K., Nakada T., Tatemoto H. Antihyaluronidase action of ellagic acid effectively prevents polyspermy as a result of suppression of the acrosome reaction induced by sperm-zona interaction during in vitro fertilization of porcine oocytes. *J. Reprod. Develop.* 2007; 53: 755-764. <https://doi.org/10.1262/jrd.18173>.
 51. Osaretin A.T., Gabriel A.A. Effect of zinc deficiency on memory, oxidative stress and blood chemistry in rats. *Adv. Med. Dent. Sci.* 2008; 2: 74-82.
 52. R.W Owen, R. Hubner, W. E Hull, G. Erben, B. Spiegelhalder, H. Bartsch, B. Haber: Isolation and structure elucidation of the major individual polyphenols in carob fiber. *Food and Chemical Toxicology* 2003.41-12:1727-1738.

Computational Insight into Conformational Rearrangement and Intramolecular-H Bond Analysis of Some Calix[4]Arenes Including Acryloyl Moiety

Arzu Karayel 

Hitit University, Department of Physics, Corum, Turkey

ABSTRACT

The conformational analyses of Calix[4]arenes reveals four different stable structures (conformations); Cone, Partial Cone, 1,2-Alternate and 1,3-Alternate after employing a density functional theory (DFT) computational analysis. Intramolecular Hydrogen Bonds (IHBs) existing Calixarene core cause Cone conformation, supporting to be the best stable state in 1, 2 and 3 compounds. In addition, one needs Natural Bond Orbital (NBO) analyses of current compounds in order to understand nature of these IHBs. Specifically, it has been shown using NBO that the LP $\rightarrow \sigma$ interactions for O \cdots O \cdots H IHBs and the delocalization LP $\rightarrow \pi^*$ for O=C=O are the major contributions to energy stabilization. Of all conformers of compound 4, Partial Cone has the lowest energy, which can be attributed to devoid of intramolecular hydrogen bond due to the absence of free phenolic groups.

Keywords:

Calix[4]arene; Acryloyl moiety; Conformational equilibrium; DFT; NBO.

INTRODUCTION

Calixarenes are macrocyclic compounds, which are utilized in important fields like pharmacy, engineering and medicine. They are applied as sensors in various areas of human activities, in medical applications and environmental protection (1, 2). Moreover, they are used in catalysis as well as in molecular recognition. Their cage-like structures play important role in host-guest mechanism in supramolecular chemistry (1, 2). In addition, the functionalization of Calixarenes by means of substituting methylene bridges with heteroatoms is quite important in order to discover new compounds (1, 2). Calixarenes attract much attention due to the rich conformational possibilities which come in four varieties: Cone, Partial Cone, 1,2-Alternate and 1,3-Alternate (3-6).

The four forms of Calixarenes are mainly due to the free rotation of methylene groups. The determination of stable conformations could not always be achieved correctly by spectroscopic techniques such as IR and NMR. On the other hand, the current state of theory on predicting Calixarene derivatives remains inconclusive or insufficient (7) hence there is still need for extensive theoretical work. Moreover, in literature, it has been highlighted that the determination of the conformational stability from experimental results of Calixarenes

derivatives could be complicated (8), thus, justifies the importance of more theoretical studies.

The main goal in this study is to scrutinize the conformational stability and the effect of intramolecular hydrogen bonds on this equilibrium of some Calix[4]arene derivatives including acryloyl moiety using first principles calculations based on Density Functional Theory (DFT). For this purpose, the most stable states of the compounds were investigated in detail by taking into account all cases including Cone (C), Partial Cone (PC), 1,2-Alternate (1,2-A) and 1,3-Alternate (1,3-A). In the next section, we will explain material and methods and computational method used in geometry optimizations of the current molecules. Later, we will discuss our results and summarize our study in conclusion part.

MATERIAL AND METHODS

In Fig. 1, the structures that are previously reported experimental synthesis and spectral characterization are depicted. These reported experimental results have been used as the starting point for the following computational study (9, 10). An X-Ray crystallography of the compound 2 is also available (10) and is used as initial configuration in following DFT calcu-

Article History:

Received: 2019/07/17

Accepted: 2019/08/29

Online: 2019/09/30

Correspondence to: Arzu Karayel,

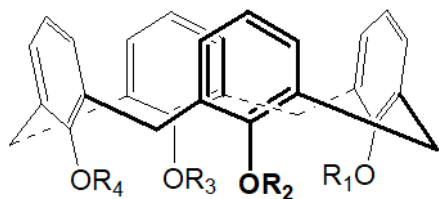
Hitit University, Department of

Physics, 19030, Corum, TURKEY

E-Mail: arzukarayel@hitit.edu.tr

Phone: +90 364 227 70 00-1676

Fax: +90 364 227 70 05



- 1 $R_1 = \text{COCH}=\text{CH}_2$, $R_2, R_3, R_4 = \text{H}$
- 2 $R_1, R_4 = \text{COCH}=\text{CH}_2$, $R_2, R_3 = \text{H}$
- 3 $R_1, R_2, R_3 = \text{COCH}=\text{CH}_2$, $R_4 = \text{H}$
- 4 $R_1, R_2, R_3, R_4 = \text{COCH}=\text{CH}_2$

Figure 1. The structures of Calix[4]arene derivatives including acryloyl moiety.

lations. These molecules are some Calix[4]arenes derivatives containing acryloyl moiety, in which they consist of p-substituted phenolic units linked by methylene bridges in the ortho position relative to the OH groups (1, 9). These relevant compounds have two usual positions, lower rim (hydroxyl groups) and upper rim (para position as to the hydroxyl groups), as shown in Fig 1.

Computational Method

The conformational equilibrium of Calix[4]arenes derivatives containing acryloyl moiety was examined by using DFT method with B3LYP functional at 6-31G(d,p) level. All possible conformers, i.e. C, PC, 1,2-A and 1,3-A

were relaxed at optimization stage. While all geometries were drawn using Gauss View 5.0 program (11), X-Ray starting geometry of compound 2 was created by taking crystal information file (cif) containing X-Ray coordinates from literature (10). Babel program (12) was used in order to transfer these coordinates into the Z-matrix format. Gaussian 09 program (13) was used in order to relax of all molecules. The intramolecular hydrogen bonding energies were calculated using NBO 3.1 program (14) as implemented in Gaussian 09 program. The molecular electrostatic potentials (MEPs) were drawn in order to see intramolecular H-bond sites. The HOMOs and the LUMOs were illustrated and the global reactivity parameters were computed.

RESULT AND DISCUSSION

Conformational Analysis of the Compounds

In molecules having hydroxyl group, Cone conformation was found to be the most stable state (molecule 1, 2 and 3 contain three, two and one hydroxyl group, respectively, as shown Fig. 2.) Hydroxyl groups led to conformational rigid structures, i.e. fixed conformations such as Cone, by means of strong O-H...O IHBs in the molecules. DFT analysis indicated the molecule 3 exists in Cone. However, Cone has only 0.11 kcal/mol lower energy than Partial Cone as shown in Table 1. As a result, it is apparent that this molecule adopts a Cone conformation since it contains at least one free phenolic group. A study on Calix[4]arene molecule which has one free hydroxyl group revealed that this molecule could exist in both confor-

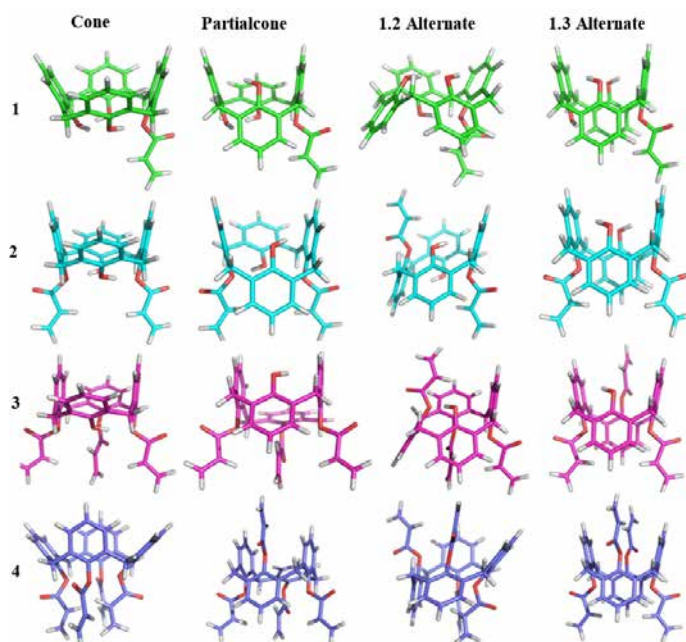


Figure 2. All possible conformers of Calix[4]arene derivatives including acryloyl moiety.

Table 1. Optimization energies of conformers of compounds **1**, **2**, **3** and **4**.

Comp.	Conformer	<i>E</i> (hartree)	ΔE kcal/mol
1	Cone	-1573.1375732	0.0
	Partial cone	-1573.1275896	6.26
	1,2-Alternate	-1573.1216164	10.01
	1,3-Alternate	-1573.1214976	10.09
2	Cone	-1763.8625073	0.0
	Experimental ^a	-1763.8613754	0.71
	Partial cone	-1763.8601678	1.47
	1,3-Alternate	-1763.8572642	3.29
	1,2-Alternate	-1763.8536385	5.57
3	Cone	-1954.5940627	0.0
	Partial cone	-1954.593894	0.11
	1,3-Alternate	-1954.592281	1.15
	1,2-Alternate	-1954.5911824	1.81
4	Partial cone	-2145.3287422	0.0
	1,3-Alternate	-2145.3283142	0.27
	1,2-Alternate	-2145.3263679	1.49
	Cone	-2145.3154581	8.34

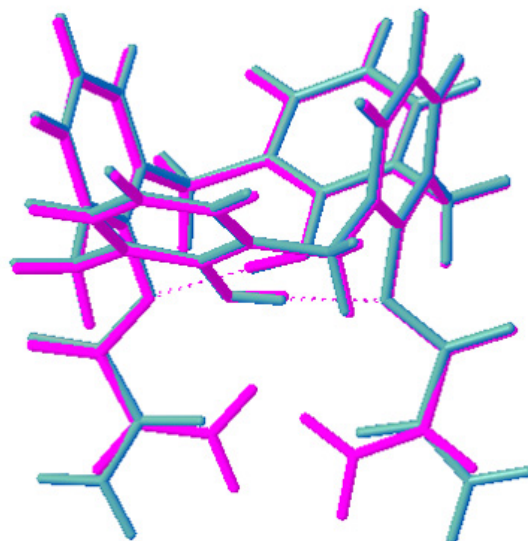
^a Experimental starting geometry was taken from X-ray coordinates (10).

mations, where one of these conformations is Partial Cone in according to NMR and second one is Cone in according to both IR and DFT. It is also reported that there is a swift exchange between Cone and Partial Cone conformations (15). Moreover, our conformational analysis of compound **4** revealed that the Partial Cone is the most stable state. In the literature, it is emphasized that Calix[4]arenes prefer the Partial Cone or 1,3-Alternate

Table 2. Hydrogen-bond geometries (Å, °) of compound **1**, **2** and **3**.

Molecule		<i>D</i> — <i>H</i> ··· <i>A</i>	<i>D</i> — <i>H</i>	<i>H</i> ··· <i>A</i>	<i>D</i> ··· <i>A</i>	<i>D</i> — <i>H</i> ··· <i>A</i>
1	Model optimization	<i>O</i> ₁ — <i>H</i> ₁ ··· <i>O</i> ₂	0.980	1.741	2.687	161.2
		<i>O</i> ₂ — <i>H</i> ₂ ··· <i>O</i> ₃	0.984	1.729	2.686	163.2
		<i>O</i> ₃ — <i>H</i> ₃ ··· <i>O</i> ₄	0.977	1.800	2.773	173.3
	Experimental ^a	<i>O</i> ₁ — <i>H</i> ₁ ··· <i>O</i> ₂	0.91 (11)	2.00 (11)	2.897 (3)	170 (9)
		<i>O</i> ₃ — <i>H</i> ₃ ··· <i>O</i> ₄	0.79 (8)	2.11 (8)	2.855 (4)	157 (8)
2	Exp_optimization	<i>O</i> ₁ — <i>H</i> ₁ ··· <i>O</i> ₂	0.970	1.878	2.843	173.5
		<i>O</i> ₃ — <i>H</i> ₃ ··· <i>O</i> ₄	0.970	1.877	2.843	173.5
	Model_optimization	<i>O</i> ₁ — <i>H</i> ₁ ··· <i>O</i> ₂	0.970	1.893	2.852	169.4
		<i>O</i> ₃ — <i>H</i> ₃ ··· <i>O</i> ₄	0.970	1.893	2.852	169.4
3	Model_optimization	<i>O</i> ₁ — <i>H</i> ₁ ··· <i>O</i> ₂	0.968	2.024	2.975	166.6
4	There is no intramolecular hydrogen bonding					

^a These results were taken from literature (10).

**Figure 3.** The comparison of optimized model geometry (blue) with optimized experimental geometry (pink) of compound **2**, where O···O distances are 1.893 Å and 1.878 Å, respectively.

conformers since they are lacking of free phenolic groups (16). In order to find exact conformation of compound **4**, we employed a DFT method which predicts the exact conformation as Partial Cone.

When the energy of the model geometry of compound **2** is compared with that of experimental geometry, it is seen a difference of 0.71 kcal/mol, as shown in Table 1. The reason of this difference can be attributed to hook-shaped direction of carbonyl groups of the acryloyl moiety in X-ray geometry (Fig. 3). This is due to steric effect of solvent toluene, as understood from experimental study (10). The experimental realization also confirms that compound **2** prefers Cone conformation due to the intramolecular

Table 3. Stabilization energies (kcal/mol) of selected NBO donor-acceptor pairs in NBO basis at B3LYP/6-31g(d,p)//B3LYP/6-31g(d,p) level for **1**, **2** and **3** compounds.

Comp.	Φ_i	Φ_j	$E_{ij}^{(2)}$ (kcal/mol)	$\epsilon_i - \epsilon_j^b$ (a.u.)	F_{ij}^c (a.u.)
1	LP_1O_9	$\sigma^*O_{55}^-H_{58}$	9.25	1.05	0.088
	LP_2O_9	$\sigma^*O_{55}^-H_{58}$	12.92	0.79	0.092
	LP_1O_{34}	$\sigma^*O_9^-H_{59}$	16.90	1.02	0.118
	LP_2O_{34}	$\sigma^*O_9^-H_{59}$	7.38	0.78	0.069
	LP_1O_{47}	$\sigma^*O_{34}^-H_{57}$	14.46	1.03	0.110
	LP_2O_{47}	$\sigma^*O_{34}^-H_{57}$	1.26	0.80	0.029
	LP_2O_{47}	$\pi^*C_{48}^-O_{49}$	39.01	0.34	0.105
2	LP_1O_9	$\sigma^*O_{62}^-H_{66}$	9.47	1.05	0.090
	LP_2O_9	$\sigma^*O_{62}^-H_{66}$	0.73	0.82	0.023
	LP_1O_{54}	$\sigma^*O_{41}^-H_{64}$	9.48	1.05	0.090
	LP_2O_{54}	$\sigma^*O_{41}^-H_{64}$	0.73	0.82	0.023
	LP_2O_9	$\pi^*C_{30}^-O_{11}$	40.44	0.34	0.106
	LP_2O_{54}	$\pi^*C_{55}^-O_{56}$	40.44	0.34	0.106
3	LP_1O_{54}	$\sigma^*O_{41}^-H_{71}$	4.51	1.05	0.062
	LP_2O_{54}	$\sigma^*O_{41}^-H_{71}$	1.90	0.81	0.037
	LP_2O_9	$\pi^*C_{30}^-O_{11}$	42.65	0.34	0.108
	LP_2O_{54}	$\pi^*C_{55}^-O_{56}$	38.58	0.34	0.104
	LP_2O_{62}	$\pi^*C_{63}^-O_{64}$	43.07	0.33	0.109

^a $E^{(2)}$: stabilization energy, ^b Energy difference of i (donor) and j (acceptor) NBO orbitals, ^c F_{ij} : the Fock matrix element.

hydrogen bond between hydroxyl and acryloyl groups (9). This result is in accordance with our theoretical results in terms of both conformational research and intramolecular hydrogen bond analysis. The optimization results regarding to intramolecular hydrogen bonding of X-Ray geometry of compound **2** were listed in Table 2 as Exp optimization line.

The intramolecular hydrogen bond of **1** is stronger than that of both **2** and **3** (Table 2). These results are in line with NBO analysis results, as shown in Table 3. The short O...O distance means the presence of robust intramolecular H-bonds. Also, the molecular electrostatic potential graphs represent the intramolecular H-bond sites as the electron-rich region in acceptor oxygens of both acryloyl moiety and the hydroxyl groups, while presenting the phenyl rings as the neutral region.

As shown in Fig. 4, HOMOs are partially distributed on Calix[4]arene core with a hydroxyl group, while LUMOs are located partially on acryloyl groups of all molecules. According to Column ΔE from top to bottom in Table 4, HOMO-LUMO energy gaps are gradually increasing, which indicate the molecules become more rigid as it can also be understood from η value.

CONCLUSION

An exhausting search of conformal configurations of Calix[4]arene derivatives including acryloyl moiety is the main promise of this work. Exclusively, compound **4** aside from others, the exact conformation could not be determined exactly by experimental methods (NMR or IR) since there is no -OH group being capable of intra-

Table 4. HOMO-LUMO energies and calculated global reactivity parameters of Calix[4]arenes.

Comp.	E_{homo} (eV)	E_{lumo} (eV)	ΔE (eV)	χ (eV)	μ (eV)	η (eV)	σ (eV) ⁻¹	ω (eV)
1(Cone)	-5.49969	-1.66969	3.8300	3.5847	-3.5847	1.9150	0.2611	3.3551
2(Cone)	-5.60010	-1.62071	3.9794	3.6104	-3.6104	1.9897	0.2513	3.2756
3(Cone)	-5.74541	-1.68711	4.0583	3.7163	-3.7163	2.0291	0.2464	3.4032
4(Partial Cone)	-6.33944	-1.48057	4.8589	3.9100	-3.9100	2.4294	0.2058	3.1465

ΔE : $E_{\text{LUMO}} - E_{\text{HOMO}}$; χ : Electronegativity, μ : Chemical potential, η : Chemical hardness, σ : Global softness, ω : Electrophilicity index

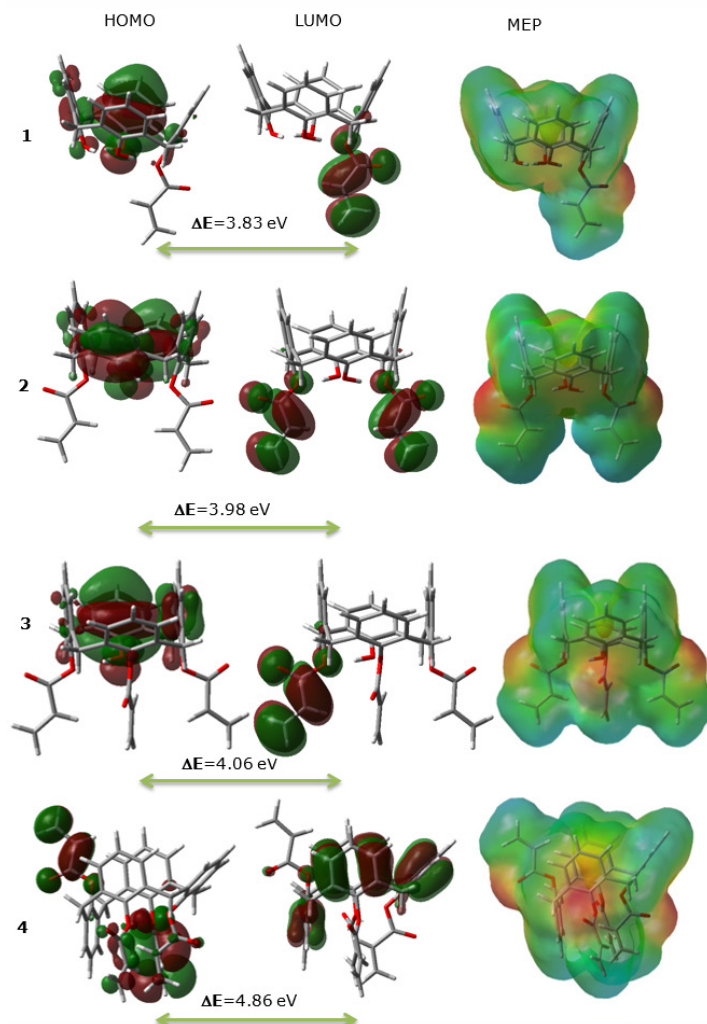


Figure 4. HOMO-LUMO and MEP drawing of the compounds.

molecular hydrogen bonding. In addition, it is only estimated that the conformational structure can be a Partial Cone or 1,3-Alternate due to the steric effect. However, the exact conformation was determined as Partial Cone by DFT method. It has been shown that molecules (1, 2 and 3) having hydroxyl group adopt Cone conformation, being most stable state, while Partial Cone is the lowest energy state for compound 4 without free phenolic groups. The robust O-H...O type bonds of 1, 2 and 3 compounds have given rise to be planarity of the molecules. In NBO analyses, it is understood that the LP \rightarrow σ^* interactions for O...O-H IHBs and the delocalization LP \rightarrow π^* for O-C=O are the major contributions to energy stabilization. The determination of accurate structures as a result of laborious conformational search will shed light on understanding of host-guest mechanisms of Calix[4]arene molecules.

ACKNOWLEDGEMENT

We thank to Associate Prof. Dr. Sevil Özkınalı for giving permission to use the structures synthesized previously to be used in theoretical calculations. The numerical calculations reported in this paper were fully performed at TUBITAK ULAKBİM, High Performance and Grid Computing Center (TRUBA resources).

References

1. Gutsche CD. Calixarenes Revisited, The Royal Society of Chemistry, Cambridge, UK, 1998.
2. Furer VL, Potapova LI, Vatsouro IM, Kovalev VV, Shokova EA, Kovalenko VI. Investigation of the conformation and hydrogen bonds in adamantylthiacalix[4]arene by IR spectroscopy and DFT. Journal of Molecular Structure 1171 (2018) 207-213.
3. Şener İ, Şener N, Erişkin S. Synthesis and absorption spectra of

- some novel hetaryl-tetrakisazocalix[4]arene derivatives. *Dyes and Pigments* 96(1) (2013) 256-263
- Galindo-Murillo R, Olmedo-Romero A, Cruz-Flores E, Petrar PM, Kunsagi-Mate S, Barroso-Flores J. Calix[n]arene-based drug carriers: A DFT study of their electronic interactions with a chemotherapeutic agent used against leukemia. *Computational and Theoretical Chemistry* 1035 (2014) 84-91.
 - Shamova LI, Shamov GA, Antipin IS, Konovalov AI. Modeling K⁺ and Ag⁺ Complexation by Thiacalix[4]arene Amides Using DFT: The Role of Intramolecular Hydrogen Bonding. *The Journal of Physical Chemistry A* 113 (19) (2009) 5691-5699.
 - Bifulco G, Gomez-Paloma L, Riccio R, Gaeta C, Troisi F, Neri P. Quantum Mechanical Calculations of Conformationally Relevant ¹H and ¹³C NMR Chemical Shifts of Calixarene Systems. *Organic Letters* 7(26) (2005) 5757-5760.
 - Guzzo RN, Rezende MJC, Kartnaller V, Carneiro JW de M, Stoyanov SR, Costa da LM. Experimental and DFT evaluation of the ¹H and ¹³C NMR chemical shifts for calix[4]arenes. *Journal of Molecular Structure* 1157 (2018) 97-105.
 - Kostyukevych KV, Khristosenko RV, Pavluchenko AS, Vakhula AA, Kazantseva ZI, Koshets IA, Shirshov YM. A nanostructural model of ethanol adsorption in thin calixarene films. *Sensors and Actuators B: Chemical* 223 (2016) 470-480.
 - Özkınalı S, Kocaokutgen H. Synthesis, spectral characterisation and thermal behaviours of some new p-tert-butylcalix[4]arene and calix[4]arene-esters containing acryloyl groups. *Journal of Molecular Structure* 1031 (2013)70-78.
 - Özkınalı S, Uçar I, Kocaokutgen H, Bulut A. 25,27-Bis(acryloyloxy)-26,28-dihydroxycalix[4]arene toluene hemisolvate. *Acta Crystallographica Section E Structure Reports Online* 63(8) (2007) o3378-o3378.
 - Roy D, Todd K, John M. GaussView, Version 5, Semichem Inc., Shawnee Mission, KS, 2009.
 - Walters P, Stahl M. Babel, Version 1.1, Department of Chemistry, University of Arizona, Tucson, AZ 85721.
 - Frisch MJ, Trucks WG, Schlegel HB, Scuseria GE, Robb MA, Cheeseman JR, Scalmani G, Barone V, Mennucci B, Petersson GA, Nakatsuji H, Caricato M, Li X, Hratchian HP, Izmaylov AF, Bloino J, Zheng G, Sonnenberg JL, Hada M, Ehara M, Toyota K, Fukuda R, Hasegawa J, Ishida M, Nakajima T, Honda Y, Kitao O, Nakai H, Vreven T, Montgomery JA, Jr., Peralta JE, Ogliaro F, Bearpark M, Heyd JJ, Brothers E, Kudin KN, Staroverov VN, Keith T, Kobayashi R, Normand J, Raghavachari K, Rendell A, Burant JC, Iyengar SS, Tomasi J, Cossi M, Rega N, Millam JM, Klene M, Knox JE, Cross JB, Bakken V, Adamo C, Jaramillo J, Gomperts R, Stratmann RE, Yazyev O, Austin AJ, Cammi R, Pomelli C, Ochterski JW, Martin RL, Morokuma K, Zakrzewski VG, Voth GA, Salvador P, Dannenberg JJ, Dapprich S, Daniels AD, Farkas O, Foresman JB, Ortiz JV, Cioslowski J, and Fox DJ. Gaussian 09, Revision C.01, Gaussian, Inc., Wallingford CT, 2010.
 - Glendening ED, Reed AE, Carpenter JE, Weinhold F. NBO Version 3.1, TCI, University of Wisconsin, Madison, 1998.
 - Özkınalı S, Karayel A. Synthesis, characterization, conformational equilibrium and intramolecular hydrogen bond analysis of Novel Azocalix[4]arenes including acryloyl moiety using DFT studies. *Journal of Molecular Structure* 1176 (2019) 303-313.
 - Chawla HM, Singh SP, Sahu SN, Upreti S. Shaping the cavity of calixarene architecture for molecular recognition: synthesis and conformational properties of new azocalix[4]arenes. *Tetrahedron* 62(33) (2006) 7854-7865.

The Performance of Gas Turbine Power Plant Using 5% Biodiesel & 95% High Speed Diesel

Mujammil Asdhiyoga Rahmanta, Tiva Winahayu Dwi Hapsari, Bernaded Oka Anggraini
PLN Research Institute, PT. PLN (Persero), 12780, Jakarta, Indonesia

ABSTRACT

Indonesia is the largest producer of crude palm oil (CPO) in the world. Biodiesel containing fatty methyl ethyl ester (FAME) is oil produced as a derivative process from CPO. Biodiesel has properties similar to high speed diesel (HSD). The Minister of Energy and Mineral Resources (MEMR) made a policy of using biodiesel as a mixture of HSD to be used as fuel in the electricity and transportation sector. There are many problems in the implementation of these fuels, especially in gas turbine power plants such as the impact on performance and reliability. In this study, the effects of biodiesel mixed with HSD were studied using a gas turbine power plant with a capacity of 18 MW. The mixture of 5% biodiesel and 95% HSD (called B5) is used as fuel for testing for 1 month operation. Performance indicators such as load, fuel consumption, specific fuel consumption, exhaust gas temperature, and nozzle pressure are monitored during the testing. Performance data and results of inspection of hot gas lines from gas turbines operated for a month are then analyzed. As the results, B5 has reduced power production, increased fuel consumption, and the potential for heat corrosion in hot gas lines. After carrying out visual and deposit sampling inspections, found many deposits containing Carbon, Sodium and Sulphur. Sediment samples were tested in the laboratory to find out metal contaminants in deposits in the transition pieces, nozzle stages one, and nozzle stages two. The metal contaminants allegedly came from HSD and Biodiesel fuel.

Keywords:

Biodiesel; High speed diesel; Performance; Reliability; Corrosion; Hot gas path; Gas turbine

Article History:

Received: 201 / 0 / 0

Accepted: 201 / / /

Online: 2019 / / 3

Correspondence to: Mujammil Asdhiyoga
Rahmanta

PLN Research Institute, PT. PLN (Persero),

12780, Jakarta, Indonesia

Tel: +62 21 797 3774

Fax: +62 21 799 1762

E-Mail: mujammil1@pln.co.id

INTRODUCTION

The Republic of Indonesia is one of the largest producers of crude palm oil (CPO) in the world along with Malaysia [1]. In addition, Indonesia is an oil importing country. To reduce oil imports, the Minister of Energy and Mineral Resources (MEMR) issued a decree No. 25 of 2013 concerning changes to Ministerial Regulation No. 32 of 2008 concerning Provision, Use and Trading of Biofuel as Alternative Energy. According to the Ministerial Decree, the use of biodiesel in the electricity sector is targeted at 7.5% in 2013, 20% in 2014, 25% in 2015, and 30% in 2016 from total oil consumption.

PLN is an Indonesian state-owned electricity company that has many diesel engines and gas turbines for its generation. In diesel engine power plants, biodiesel and high speed diesel (HSD) mixed fuels can be implemented properly. Apart from not requiring engine modifications, this is because there are no major problems in terms of performance and reliability. However, in gas turbine power plants, there are many implementation

problems in gas turbine power plants such as performance and reliability issues.

Biodiesel contains fatty ethyl methyl ester (FAME) which has similar properties as HSD oil especially with low viscosity characteristics [2, 3, 4, 5]. The most common method used in producing biodiesel is the CPO transesterification process. In this process, the raw material for lipids is converted into biodiesel. One mole of triglycerides reacts with three moles of alcohol to produce three moles of mono alkyl ester and one mole of glycerol. To increase the reaction rate and yield of biodiesel, the catalyst is usually added to excess alcohol, which shifts the equilibrium to the product side because of its reversible reaction [6, 7, 8]. Traditionally, the transesterification process uses solvents including ethanol or methanol and homogeneous catalysts such as KOH, NaOH, and H₂SO₄ [5, 9]. However, this method has several disadvantages such as extensive separation processes, generation of wastewater, and corrosion of equipment [9, 10, 11].

Biodiesel has similar properties as HSD as indicated in Indonesian National Standard (SNI) No. 7182: 2015 quality requirements for biodiesel. For physical and chemical properties, biodiesel has a number that is relatively the same as HSD as stated in the decision of the Director General of Oil and Gas MEMR No. 14499K/14/DJM/2008 concerning Standards and Quality of Types of Diesel Fuel Marketed Domestically. But, naturally biodiesel has specific properties such as coagulants or clumps (at relatively low temperatures) and depressoants (cleaning deposits in pipelines).

The 18 MW gas turbine power plant used in this trial is an industrial gas turbine produced by General Electric. Gas turbines have been designed to use gas and oil as fuel. This study is intended to determine the effect of performance and reliability of the use of 5% biodiesel and 95% HSD mixtures or B5.

MATERIALS AND METHODS

Shown in Figure 1 that B5 is used as fuel during testing. Biodiesel is mixed with HSD in tanks for 1 month operational consumption. Before being mixed, biodiesel and HSD were sampled and analyzed. Biodiesel and HSD fuels are supplied from two different companies. After being mixed in tanks with a fuel ratio of 5% biodiesel and 95% HSD, mixed fuels are sampled according to the ASTM D 4057 Standard Practice for Manual Sampling of Petroleum and Petroleum Products. Fuel samples were tested and analyzed in the laboratory before being verified and confirmed for use in experiments. Then the gas turbine is operated for a month with continuous base load conditions.

During the 1 month trial, performance parameters were monitored in the control room and locally. After 1 month of operation, visual inspection and deposit sampling is done to get the data to be analyzed.

Gas Turbine Specification

The specifications of the gas turbine power plant for testing are shown in Table 1. This power plant has been operating since 1993 for peak load conditions. The plant is installed with a capacity of 20 MW. Because it has experienced long operating hours for years, now it is only

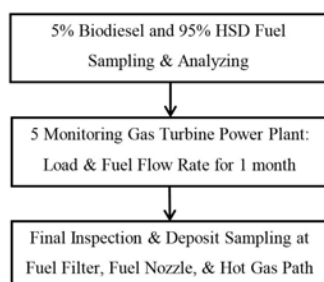


Figure 1. Flowchart of the experiment

Table 1. Specification of gas turbine

Specification	Value
Manufacturer	GEC Alstom
Installed capacity	20 MW
Compressor & Turbine speed	5,100 rpm
Compressor stage	17
Pressure ratio	10
Turbine impulse stage	2
Combustor (Nozzle)	10 multiple combustor reverse flow
Chamber arrangement	Concentrically located around compressor
Generator Speed	3,000 rpm

able to operate with a maximum load of 18 MW due to a decrease in the life of the material.

Gas Turbine Monitoring

During 1 month of testing, gas turbine power plants continued to be monitored as usual performance parameters as shown in Table 2. In this test, B5 fuel was sampled and analyzed four times during the 1 month test. This is done to find out and maintain the quality of the mixed fuel during testing as next as shown in Table 4.

Table 2. Operating performance parameters

No.	Monitoring Item	Data Resource
1	Fuel properties	Sample analyzing
2	Fuel flow	Flow meter counter
3	Load	Data logger export meter
4	Nozzle pressure	Monitor control room
5	Deposit	Visual and sampling observation
6	Flue gas temperature	Monitor in the control room
7	Flue gas	Flue gas duct

The schematic diagram [12] of the gas turbine operation performance test is shown in Fig. 2. The dashed line shows the measurement instrument of the operating process, such as fuel sample, fuel flow rate, pressure nozzle, load, exhaust gas, & gas temperature throw away. Turbine inspection and deposit sampling is carried out after 1 month of the gas turbine being operated. The deposit sample is tested in the laboratory to find out the metal material or composition. The results of the composition of the metal are used to determine whether it comes from fuel or gas turbine material.

Fuel Characteristics

Fuel is tested before testing as shown in Table 3. HSD & biodiesel are tested by CV. Petrolab before mixing in the tank. As shown in Table 3, the properties of biodiesel are similar to HSD such as kinematic viscosity which is very important in the atomization process in a fuel nozzle. The gross calorific value of biodiesel is lower than HSD

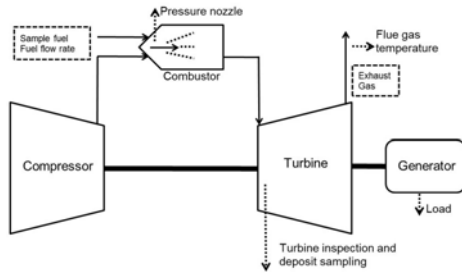


Figure 2. Simple cycle of gas turbine in the experiment

around 10%. But, the biodiesel flash point is higher than HSD around 20%. While impurity metals such as Sodium or Na and Lead or Pb have the same relative value. B5 mixture is tested as shown in Table 4 where the result of the mixed B5 parameter is between the results of HSD & biodiesel.

Table 3. HSD, Biodiesel, & B5 properties before performance test*

Parameter	Unit	Result			Method
		HSD	FAME	B5	
Specific gravity at 60/60 °F	-	0,842	0,866	0,843	ASTM D1298
Kinematic viscosity at 40 °C	cSt	3,454	4,084	3,647	ASTM D445
Sulphur content	%	0,165	0,03	0,182	ASTM D4294
Water content	%	<0,05	0,08	<0,05	ASTM D95
Ash content	%	0,01	0,01	0,01	ASTM D482
Flash point PMCC	oC	82	108	80	ASTM D93
Gross calorific value	KCal/kg	10.516	9.175	10.120	ASTM D240
Carbon residue	ppm	0,01	0,05	0,02	ASTM 189
Vanadium, V	ppm	<0,1	<0,1	<0,01	ASTM D5708
Natrium, Na	ppm	1,52	1,76	1,84	ASTM D5709
Kalium, K	ppm	Nil	Nil	<0,01	ASTM D5710
Calcium, Ca	ppm	2,3	4,62	2,9	ASTM D5711
Timbal, Pb	ppm	2,66	1,93	<0,01	ASTM D5712
Besi, Fe	ppm	Nil	0,08	0,21	ASTM D5713

*Tested by CV. Petrolab Service

During 1 month operation, B5 is tested to determine the stability of its parameters. B5 fuel sampling is carried out on days 1, 11, 20, & 29. Shown in Table 4, the results of parameters such as viscosity, flash point, density, and heating value are relatively stable. But, the water content is not stable.

Table 4. B5's properties during the 1 month test

No.	Parameter	Unit	B5 Result** (day to)				Method
			1	11	20	29	
1	Viscosity 40 °C	cSt	3,21	3,12	3,15	3,17	ASTM D445
2	Flash point	°C	76	76	75	75	ASTM D 93
3	Water content	Ppm	113	523	380	133	ASTM D 95
4	Density 15 °C	g/ml	0,8415	0,8405	0,8395	0,8405	ASTM 1298
5	Heating Value	MJ/kg	46.567	46.245	46.036	45.903	ASTM 240

Table 5. The result of emission test during 1 month operating test

No.	Parameter	Unit	Result** (day to)				Restriction
			1	11	20	29	
1	NO _x	mg/m ³	149	135	139	145	< 800
2	SO _x	mg/m ³	296	-	12	23	< 1000
3	Opacity	%	5	5	5	5	< 20

***Measured by PLN Research Institute during the performance tests which held four times a month

RESULTS AND DISCUSSION

Emission Test

Compared with the limit value of the regulation of the Minister of Environment No. 21 of 2008 [13], the results of parameters such as NO_x, SO_x, & Opacity are lower than the limit value. The test is carried out four times a month, and all results do not exceed the limitation value.

Performance Test Result

During the 1 month operation test, we conducted performance tests from fuel sampling to analyze performance characteristics for four times. Shown in Table 6, the turbine exhaust temperature is limited to below 500 °C. Ex-

Table 6. The result of the gas turbine performance (base load continuous) operated with B5

No.	Parameter	Unit	Result (day to)			
			1	11	20	29
1	Compressor air inlet temp	°C	32,5	28,47	29,28	32,14
2	Barometric pressure	mbar	1016	1015,44	1015,5	1015,5
3	Compressor inlet humidity	% RH	51,44	79,72	75,44	65,89
4	Fuel oil consumption	liter	15203	15320,5	14804	14579
5	Turbine Exhaust temp.	°C	495,13	494,87	494,96	495,08
6	Active Load	MW	17,83	17,5	16,74	16,38
7	Gross power output	kWh	35806,32	35285,14	33603,86	
8	Gross SFC	l/kWh	0,4246	0,4342	0,4405	0,4444
9	Gross Heat Rate	kCal/kWh	3819,415	3881,265	3949,043	3997,38

Table 7. The result of specific fuel consumption of the gas turbine after 1 month operated with B5

No.	Parameter	Before start	After shut down	Total
1	Counter kWh	308,866,900	321,227,000	12,360,100
2	Counter fuel (liter)	1,404,410	6,707,659	5,303,249
3	SFC (liter/kWh)	-	-	0.429062

penses decreased from the first day of 17.83 MW to 16.38 MW on day 29th. The cost decreased by 8.13%. Meanwhile, specific fuel consumption (SFC) increased from the first day 0.4246 to 0.4444 days on day 29th. The actual SFC for a month shown in Table 7 is 0.428 l/kWh. The increase in SFC is 4.66%.

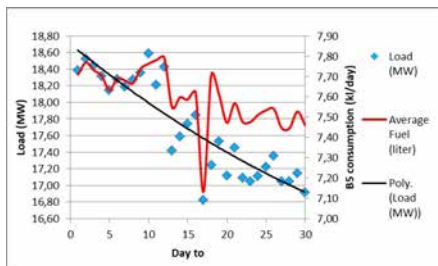


Figure 3. Graph of load and fuel (B5) consumption for a month

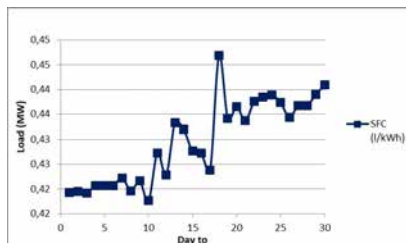


Figure 4. Graph of SFC for a month

Shown in Fig. 3, the load and fuel consumption decrease from the first day to the 30th day. The SFC value increases because the load decreases from the first day to the 30th day as shown in Fig. 4. The nozzle pressure trend lines 1 to 10 are shown in Figure 5 & 6. The gas turbine has 10 combustion chambers, so 10 nozzles are installed. The average nozzle pressure is shown in Fig. 7, it appears that the average nozzle pressure decreases because the load decreases.

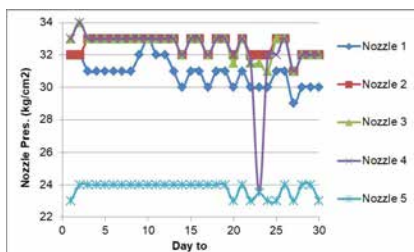


Figure 5. Graph of nozzle pressure from nozzle 1 to 5

Inspection Result

Shown in Fig. 8, the no. 2 fuel nozzle condition is divided into three different conditions. Seen from the picture,

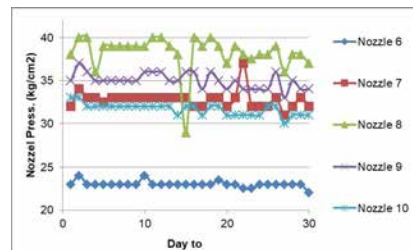


Figure 6. Graph of nozzle pressure from nozzle 6 to 10

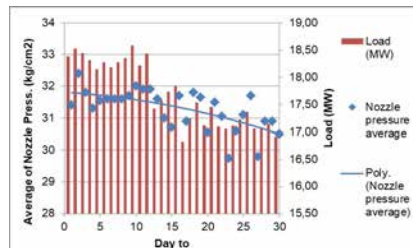


Figure 7. Graph of nozzle pressure average for a month

the deposit is formed on the nozzle after being operated by HSD and B5. A white deposit is formed in the combustion liner after being operated with B5 as shown in Fig. 9 (c).

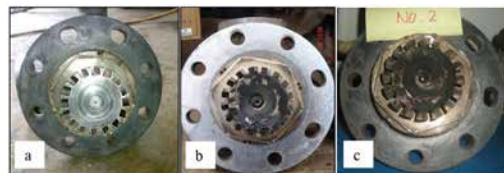


Figure 8. Visual inspection of fuel nozzle no. 2 (a) before operated (b) after operated by HSD (c) after operated with B5 for 1 month

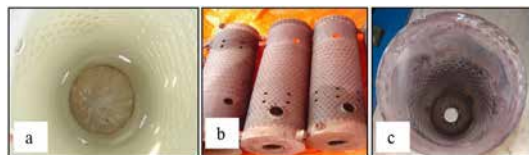


Figure 9. Visual inspection of combustion liner no. 2 (a) before operated (b) after operated by HSD taken on Major Overhaul (c) after operated with B5 for 1 month



Figure 10. Visual inspection of transition piece (a) before operated (b) after operated by HSD taken on Major Overhaul (c) after operated with B5 for 1 month



Figure 11. Visual inspection of 1st stage turbine nozzle (a) before operated (b) after operated by HSD taken on Major Overhaul (c) after operated with B5 for 1 month

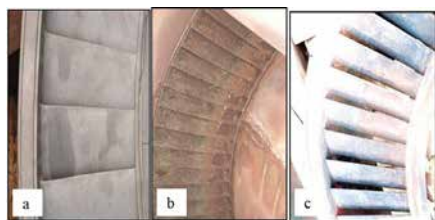


Figure 12. Visual inspection of 2nd stage turbine nozzle (a) before operated (b) after operated by HSD taken on Major Overhaul (c) after operated with B5 for 1 month

The white deposit is in the transition piece in Fig. 10 (c), the first stage nozzle in Fig. 11 (c), and the second stage nozzle in Fig. 12 (c) is taken after testing. The samples are analysed in the laboratory then the results are shown in Table 7. The deposits mostly contain Na, S, Fe, and Ni. Based on X-ray Diffraction and Dispersive Energy Spectroscopy (EDS), the compounds formed on the deposit are Sodium Sulphate (Na_2SO_4) which has the potential to make heat corrosion [14] to peel off the thermal barrier layer, and to lead corrosion in the basic ingredients contained with Fe & Ni as shown in Fig. 13. Deposits such as Na and S are likely to come from impurities in the fuel either HSD or biodiesel.

Table 8. The composition of trace metal in the deposit after 1 month operated by B5

No.	Parameter	Unit	Deposit located at****		
			Transition piece	1st stage nozzle	2nd stage nozzle
1	Natrium, Na	%	33,16	34,26	32,31
2	Magnesium, Mg	%	1,77	2,29	3,42
3	Aluminium, Al	%	-	0,97	-
4	Silika, Si	%	-	0,33	0,35
5	Sulfur, S	%	38,64	41,96	36,05
6	Kalium, K	%	0,58	0,37	0,74
7	Calcium, Ca	%	0,86	1,40	0,74
8	Chromium, Cr	%	2,91	2,90	3,21
9	Mangan, Mn	%	0,21	0,22	0,81
10	Ferrum, Fe	%	7,62	3,28	10,51
11	Cobalt	%	-	9,25	6,65
12	Nickel, Ni	%	11,46	2,43	4,02
13	Zink, Zn	%	1,10	0,37	0,52
14	Molibdenum, Mo	%	0,28	-	0,39
15	Plumbum, Pb	%	0,81	-	-

****Tested by Metallurgy Laboratory at University of Indonesia



Figure 13. Visual inspection of 1st stage turbine nozzle (erosion material) after operated with B5

CONCLUSION

The use of B5 in gas turbine power plants has decreased in output power, increased SFC fuel consumption, and led sediment materials that increase the potential for corrosion of hot gases in hot gas path material from gas turbines. Fuel that is clean of impurities and sulphur is needed to reduce this risk.

ACKNOWLEDGEMENT

This research is fully funded by PT. PLN (Persero), a state owned electricity company of Indonesia. The test was conducted and facilitated by PT. Pembangkitan Jawa Bali (PJB) as the subsidiary company of PT. PLN (Persero).

REFERENCES

1. Directorate General of Estate Crops of The Ministry of Agriculture of Republic Indonesia, 2016, Tree Crop Estate Statistics Of Indonesia 2015-2017, Jakarta: Secretariate of Directorate General of Estate Crops of The Ministry of Agriculture of Republic Indonesia.
2. Enagi I, Al-attab KA, Zainal ZA., 2018, Liquid biofuels utilization for gas turbines: a review. *Renew Sustain Energy Rev.*
3. Gupta KK, Rehman A, Sarviya RM., 2010, Bio-fuels for the gas turbine: a review. *Renew Sustain Energy Rev.*14:2946–55.
4. Sajjadi B, Raman AAA, Arandiyan H., 2016, A comprehensive review on properties of edible and non-edible vegetable oil-based biodiesel: composition, specifications and prediction models, *Renew Sustain Energy Rev.*, 63:62–92.
5. Gashaw, A.; Getachew, T.; Teshita, 2015, A review on biodiesel production as alternative fuel. *J. For. Prod. Ind.*, 4, 80–85.
6. Ma, F., Hanna, M.A. 1999, Biodiesel production: A review. *Bioresour, Technol*, 70, 1–15.
7. Duran, E.A., Tinoco, R., Perez, A., Berrones, R., Eapen, D., Sebastian, P.J., 2014, A comparative study of biodiesel purification with magnesium silicate and water. *J. New Mater. Electrochem. Syst.*, 17, 105–111.
8. Stamenkovic, O.S., Todorovic, Z.B., Lazic, M.L., Veljkovic, V.B., Skala, D.U., 2008, Kinetics of sunflower oil methanolysis at low temperatures. *Bioresour. Technol.*, 99, 1131–1140.
9. Talha, N.S., Sulaiman, S., 2016, Overview of catalysts in biodiesel production. *ARNP J. Eng. Appl. Sci.*, 11, 439–448.
10. Lotero, E., Liu, Y., Lopez, D.E., Suwannakarn, K., Bruce, D.A., Goodwin, J.G., 2005, Synthesis of biodiesel via acid catalysis. *Ind. Eng. Chem. Res.*, 44, 5353–5363
11. Saifuddin, N., Samiuddin, A., Kumaran, P., 2015, A review on processing technology for biodiesel production. *Trends Appl. Sci. Res.*, 10, 1–37..
12. Borman G.L., 1997, *Combustion Engineering*, Singapore: McGrawHill Book Co.
13. Minister of Environment Republic Indonesia, 2008, Regulation of Minister of Environment Republic Indonesia No. 21 of 2008, Quality Standards for Non-Moving Source Emissions for Businesses and / or Thermal Power Generation Activities.
14. Eliaz, N., 2000, Hot corrosion in gas turbine components, *Engineering Failure Analysis*, Pergamon 9, pp 31-43.

